UNIVERSITY OF CALIFORNIA SAN DIEGO

Defect effects on mechanical properties and deformation behavior of materials: from quantum mechanics to molecular dynamics assisted by machine learning

A dissertation submitted in partial satisfaction of the
requirements for the degree
Doctor of Philosophy

in

NanoEngineering

by

Hui Zheng

Committee in charge:

Professor Shyue Ping Ong, Chair
Professor Olivia Graeve
Professor Jian Luo
Professor Marc A. Meyers
Professor Vitali Nesterenko
Professor Kesong Yang

2021

The dissertation of Hui Zheng is approved, and it is acceptable in quality and form for publication on microfilm and electronically.

University of California San Diego

2021

DEDICATION

To my loving family.

TABLE OF CONTENTS

Dissertation Approval iii

Dedication iv

Table of Contents v

List of Figures viii

List of Tables xi

Acknowledgements xii

Vita xiv

Abstract of the Dissertation xv

Chapter 1 Introduction 1
- 1.1 Background 2
- 1.2 Defects and strengthening mechanisms 2
  - 1.2.1 Point defects 3
  - 1.2.2 Linear defects: dislocations, the leading carriers of plastic deformation 4
  - 1.2.3 Planar defects 5
- 1.3 Solid solution strengthening 6
- 1.4 Atomic-scale materials modeling 7
  - 1.4.1 Quantum-mechanical computation 7
  - 1.4.2 Classical molecular dynamics simulation 7
- 1.5 Objectives and projects summary 8

Chapter 2 Role of Zr in strengthening $MoSi_2$ from density functional theory calculations 10
- 2.1 Introduction 11
- 2.2 Methods 12
  - 2.2.1 DFT calculations 12
  - 2.2.2 Derived quantities 13
- 2.3 Results 15
  - 2.3.1 Structural model for $MoSi_2$ GB 15
  - 2.3.2 Site preference of single O and Zr dopant in bulk $MoSi_2$ . . 16
  - 2.3.3 Zr effect on O embrittlement of $MoSi_2$ GB 18
  - 2.3.4 Structural model for Zr/$MoSi_2$ interface 19
  - 2.3.5 Relative oxygen affinities of Zr and $MoSi_2$ 21
  - 2.3.6 Mechanical properties of the clean and O-contaminated α-Zr/$MoSi_2$ interface 21

2.4 Discussion . . . 22
2.4.1 Zr as a dopant . . . 22
2.4.2 Zr as a getter . . . 25
2.4.3 Screening for getter materials . . . 26
2.5 Conclusion . . . 29

Chapter 3 Grain boundary properties of elemental metals . . . 30
3.1 Introduction . . . 31
3.2 Methods . . . 33
3.2.1 Grain boundary model generation . . . 33
3.2.2 GB property computation . . . 34
3.2.3 DFT computations . . . 35
3.2.4 Scope and Availability of Data . . . 36
3.3 Results . . . 37
3.3.1 Benchmarking . . . 37
3.3.2 Grain boundary energies . . . 41
3.3.3 Work of separation . . . 44
3.3.4 Multiple linear regression model for γ_{GB} . . . 45
3.4 Conclusion . . . 49

Chapter 4 Predictive processing of NbMoTaW multi-principal element alloy to tune short-range order and mechanical properties . . . 50
4.1 Introduction . . . 51
4.2 Methods . . . 52
4.2.1 Chemical SRO parameters . . . 53
4.3 Results . . . 54
4.3.1 The effect of annealing temperature on SRO . . . 54
4.3.2 The kinetics and thermodynamics of SRO . . . 56
4.3.3 The effects of SRO on stacking fault energy and anti-phase boundary energy . . . 57
4.3.4 SRO-dependent critical resolved shear stress distribution . . . 59
4.3.5 The strength and ductility affected by SRO and temperature 63
4.3.6 The thermostability of SROs and Nb segregation in nanocrystalline MPEA . . . 66
4.4 Discussion . . . 67
4.5 Conclusion . . . 70

Chapter 5 Summary and Outlook . . . 72

Appendix A Supporting information: Role of Zr in Strengthening $MoSi_2$ Grain Boundaries from Density Functional Theory Calculations . . . 75

Appendix B Supporting information: Grain boundary properties of elemental metals . 82

Bibliography 106

LIST OF FIGURES

Figure 2.1: Models of the clean structures used in this work 17
Figure 2.2: Work of separation W_{sep} of Σ5 (001) twist GB of $MoSi_2$ with $4O_{int}$, $2Zr_{Mo}$, and ($4O_{int}$ + $2Zr_{Mo}$) with respect to coverage. 20
Figure 2.3: Relative energies (ΔE) of one O_{int} defect at different regions of α-Zr/MoSi2. The zero of the energy is set at the energy of the structure with O_{int} in bulk-like $MoSi_2$ (position 1). 22
Figure 2.4: Work of separation (W_{sep}) of clean and O_{int}-contaminated Zr/MoSi2 interfaces. The black dashed line indicates the W_{sep} of the clean Σ5 (001) twist GB of $MoSi_2$ as a reference. 23
Figure 2.5: Electron localization function (ELF) distribution of (a) clean $MoSi_2$ grain boundary (GB), (b) $4O_{int}$ doped GB, (c) $2Zr_{Mo}$ doped GB and (d) $4O_{int}$ + $2Zr_{Mo}$ doped GB. 24
Figure 2.6: Plot of silicate formation energy versus oxygen exchange reaction energy for 55 elements in the periodic table. 28

Figure 3.1: Grain boundary generation process 34
Figure 3.2: DFT calculated GB energy. For bcc and fcc, the lowest γ_{GB} types, i.e., Σ3[110](112) for bcc and Σ3[111](111) for fcc are plotted. For hcp, and double-hcp (dhcp) elements, Σ7(0001) GBs are chosen to be represented in this periodic table heatmap. 36
Figure 3.3: High-throughput computational workflow for elemental grain boundaries. . 40
Figure 3.4: GB energy γ_{GB} distribution for (a) bcc, (b) fcc, and (c) hcp/dhcp elemental metals, sorted by increasing γ_{GB}. 42
Figure 3.5: Comparison of γ_{GB} between this work and (a) previous DFT values; (b, c) EAM[1,2] and SNAP[3,4] values. (d), (e) and (f) compare our the calculated γ_{GB} of bcc Fe, fcc Al, and fcc Ni with experimentally measured MRD[5–7]. . . . 44
Figure 3.6: Comparison between surface energy (γ_{surf}), GB energy (γ_{GB}) and work of separation (W_{sep}) for (a) bcc Σ3(110), (b) fcc Σ3(111) and (c) hcp Σ7(0001) GBs, plotted in order of ascending cohesive energy E_{coh} of the element. . . 46
Figure 3.7: Relationship between calculated work of separation W_{sep} for GB with lowest γ_{GB} and experimentally measured ultimate tensile strength (UTS)[8]. 47
Figure 3.8: Multiple linear regression models for the (a) bcc $\Sigma3(110)$, (b) fcc $\Sigma7(111)$, and (c) hcp $\Sigma7(0001)$ GBs. 48

Figure 4.1: Short-range order (SRO) of bulk MPEA from different annealing temperatures T_a. (a) Pairwise SRO of bulk MPEA annealed from different temperatures from 300 K to 2400 K. (b-d) Atomic structure representatives after 2 ns MC/MD calculations at T_a= 300, 600, and 1200 K, respectively. 55
Figure 4.2: Vacancy formation energy (E_f^V), the kinetically resolved activation barriers of migration (E_{KRAB}), and the sum of E_f^V and E_{KRAB} named as activation energy of self-diffusion (E_a) for Nb, Ta, Mo and W in the alloy. 57

Figure 4.3: Calculated stacking fault energy (SFE) from structures annealed at T_a= 300, 600, 900, and 1200 K, respectively. 60
Figure 4.4: The distribution of CRSS is affected by various SROs which correspond to T_a= 300, 600, and 1200 K. 61
Figure 4.5: The spatial distributions of stacking fault energy and anti-phase boundary energy in samples annealed from T_a = 300 K, 600 K, 900 K, and 1200 K. . 62
Figure 4.6: Uniaxial tensile/compressive tests of bulk MPEA structures annealed from different temperatures. 64
Figure 4.7: Structure evolution under uniaxial tension of bulk MPEA structures with SROs and RSS configurations. 65
Figure 4.8: The SRO evolution of polycrystalline MPEAs under different temperatures of MD simulations. The top panel corresponds to the structure with Nb segregation and the large SRO. The bottom panel corresponds to a RSS. . . 67
Figure 4.9: The polycrystalline MPEA evolution under 2400 K MD simulation. 68
Figure 4.10: The polycrystalline MPEA structure evolution at 2400 K for both random solid solution structure and the structure with high SRO and Nb segregation 68

Figure A.1: Convergence of work of separation (W_{sep}) with respect to k-points grid and cutoff energy for ($4O_{int}$ +$2Zr_{Mo}$) doped $MoSi_2$ grain boundary. The W_{sep} are converged to ± 0.02 J/ m^2, as indicated by the red dashed lines. 77
Figure A.2: Schematic showing different cleavages for doped grain boundaries and interfaces. 78
Figure A.3: Relative energies (ΔE) of one O_{int} defect at different regions of β-Zr/$MoSi_2$. The zero of the energy is set at the energy of the structure with O_{int} in bulk-like $MoSi_2$ (position 1) 79
Figure A.4: Bader analysis of clean $MoSi_2$ GB as shown in Table A.2. Negative values indicate electron donors, and positive values indicate electron acceptors. . . 79
Figure A.5: Bader analysis of $4O_int$ doped $MoSi_2$ grain boundary. Negative values indicate electron donors, and positive values indicate electron acceptors. . 80
Figure A.6: Bader analysis of Zr_{Mo} doped $MoSi_2$ grain boundary. Negative values indicate electron donors, and positive values indicate electron acceptors. 80
Figure A.7: Bader analysis of $4O_{int}$+$2Zr_{Mo}$ doped $MoSi_2$ GB. Negative values indicate electron donors, and positive values indicate electron acceptors. 80

Figure B.1: Lattice translation tests (along c direction) for twist GBs. 83
Figure B.2: Lattice translation tests (along a and b directions) for twist GBs. 84
Figure B.3: GB length convergence tests of bcc Mo and fcc Cu 85
Figure B.4: GB length distribution of all 327 GBs. 86
Figure B.5: The γ_{surf} varies moderately across different surfaces while the γ_{GB} varies dramatically across different GB types. This causes the near-linear relationship between γ_{GB} and W_{sep} as shown in Figure B.6. 101

Figure B.6: The near linear trend between work of separation and GB energy. Each color represents one type of element. We observe a negative correlation between the value of W_{sep} and γ_{GB} for each element. 102
Figure B.7: The comparison between normalized GB energy and work of separation (both normalized by cohesive energy). The negative correlation between normalized γ_{GB} and W_{sep} of each element is observable. 103
Figure B.8: Linear fitting for all GB types of bcc elements with $\gamma_{GB} = \beta_1 E_{coh} a_0^{-2} + \beta_2 G \cdot a_0$. 104
Figure B.9: Linear fitting for all GB types of fcc elements with $\gamma_{GB} = \beta_1 E_{coh} a_0^{-2} + \beta_2 G \cdot a_0$. 105

LIST OF TABLES

Table 2.1: Grain boundary energies (γ_{GB}) and interface energies ($\gamma_{interface}$) with different terminations. 14
Table 2.2: Dopant formation energy (E_d) of four types of dopant in bulk $MoSi_2$ 18

Table 3.1: GB types calculated in this work. Note: The $\Sigma 7[111](111)$ twist GBs of bcc Li, Na, K, Rb, Cs and Ba have 336 atoms instead of 168. 37
Table 3.2: CPU hours for GB relaxation with and without the use of scaled prototype templates. 41

Table A.1: Work of separation (in J/m^2) for different cleavages of doped grain boundaries. 76
Table A.2: Bader analysis of clean $MoSi_2$ GB as shown in Figure A.4. Negative values indicate electron donors, and positive values indicate electron acceptors . . . 76
Table A.3: Bader analysis of $4O_iint$ doped $MoSi_2$ grain boundary as show in Figure A.5. Negative values indicate electron donors, and positive values indicate electron acceptors. 78
Table A.4: Bader analysis of Zr_{Mo} doped $MoSi_2$ grain boundary as shown in Figure A.6. Negative values indicate electron donors, and positive values indicate electron acceptors. 78
Table A.5: Bader analysis of $4O_{int}$+$2Zr_{Mo}$ doped $MoSi_2$ GB as shown in Figure A.7. Negative values indicate electron donors, and positive values indicate electron acceptors. 81
Table A.6: Work of separation W_{sep} in J/m^2 for different cleavages of doped/un-doped $\alpha - Zr/MoSi_2$ and $\beta - Zr/MoSi_2$ interface. 81
Table A.7: Strain effect on the surface energy for the cleavage (II in Figure A.2) with the lowest work of separation of α-Zr/$MoSi_2$ interface. 81

Table B.1: Force convergence test of Mo $\Sigma 3$ (112) GB 86
Table B.2: 3D shift test 87
Table B.3: Comparison between full grid search and two-step search scheme for Mo and Nb GBs. Only five lowest GB energy translations are shown at each step. It can be seen that the two schemes find essentially similar low energy translations. 88
Table B.4: Grain boundary energies (J/m^2) of cubic elements. 92
Table B.5: Grain boundary energies (J/m^2) of hcp elements 93
Table B.6: Work of separation (W_{sep} (J/m^2)) of cubic elements 94
Table B.7: Work of separation (W_{sep} (J/m^2)) of hcp elements 95
Table B.8: The comparison between the DFT calculated GB energies and the corresponding GB energies from references (in units of J/m^2). 95
Table B.9: Materials project mp-ids of all elements included in this work 99

ACKNOWLEDGEMENTS

First and foremost, I'm incredibly grateful to my advisor Prof. Shyue Ping Ong. His vision and enthusiasm in advancing the cutting-edge of research is excellent enlightenment for me. His dedication, efficiency, and the highest standard in work set a great model for me. I always appreciate his professional and constructive advice on my research projects and his great recommendations in helping us to build networks in our research community.

I want to extend my sincere thanks to all my committee members, Prof. Jian Luo, Prof. Kesong Yang, Prof. Olivia Graeve, Prof. Marc Meyers, and Prof. Vitali Nesterenko. I appreciate all your precious time and efforts in providing me insightful suggestions and encouragement over our communications.

I am very grateful to have collaborated with many outstanding researchers, including Prof. Kristin Persson, Dr. Matthew Horton, Dr. Donald Winston, Prof. Robert Richie, Prof.Mark Asta, and Dr. Sheng Yi from the University of California Berkeley. Prof. Shengfeng Yang from Indiana University–Purdue University Indianapolis, Prof. Zhenzhen Xu, Dr. Yu Hong, and Benjamin Schneiderman from Colorado school of mines. Prof. Irene Beyerlein, Prof. Anton Van der Ven, Prof. Daniel S. Gianola, Prof. Tresa Pollock, Dr. Shuozhi Xu, Dr. Yanqing Su, Dr. Fulin Wang, Dr. Jungho (Paul) Shin from University of California, Santa Barbara. I learned a lot from the insightful discussions with you.

It is my great fortune to spend five years in Materials Virtual Lab (MAVRL), where I received excellent guidance from Dr. Chi Chen and Dr. Xiang-guo Li in both career and life choices. Special thanks to Dr. Richard Tran, a great accompany during the challenging time in pursuing a Ph.D. degree. I also enjoyed working with Dr. Yunxing Zuo, Dr. Balachandran(Bala) Radhakrishnan, Weike Ye, Luke Nibbelink. Thanks also to Dr. Iek-Heng Chu, Dr.Zhenbin Wang, Dr. Zhi Deng, Dr. Zhuoying Zhu, Dr. Chen Zheng, Dr. Zihan Xu, Dr. Hanmei Tang, Dr. Mahdi Amachraa, Xinyu Guo, Yiming Chen, Ji Qi, Takumi Kitayama, you made my time in MAVRL full with support and fun.

Last but not least, I want to express my gratitude to my supportive family and friends. The patience, sweetness, and encouragement from my husband Gareth always bring me joy and ease during hard times. My parents' ongoing care and trust support me to pursue my dream. I am also grateful to have friends Chongze Hu, Bo Yan, Jiying Jiang, Sally, Crista, Paige, Amy, Patricia, Yingcong, and Linger. They support me from different perspectives and make my Ph.D. life filled with accompany and support.

Chapter 2, in full, is a reprint of the material "Role of Zr in strengthening $MoSi_2$ from density functional theory calculations" as it appears on Acta Materialia 2018, 145, 470–476. Hui Zheng Richard Tran, Xiang-Guo Li, Balachandran Radhakrishnan, Shyue Ping Ong. The dissertation author was the primary investigator and author of this paper.

Chapter 3, in full, is a reprint of the material "Grain boundary properties of elemental metals" as it appears on Acta Materialia 2020, 186, 40–49. Hui Zheng Xiang-Guo Li, Richard Tran, Chi Chen, Matthew Horton, Donald Winston, Kristin Aslaug Persson, Shyue Ping Ong. The dissertation author was the primary investigator and author of this paper.

Chapter 4, in full, is under preparation for publication of the material "Predictive processing of NbMoTaW multi-principal element alloy to tune short-range order and mechanical properties" Hui Zheng, Luke Nibbelink, Xiang-Guo Li, Yunxing Zuo, Chi Chen, Shyue Ping Ong. The dissertation author was the primary investigator and author of this paper.

VITA

2013	B. Eng. in Electronic Science and Technology , Jilin University
2016	M. S. in Microelectronics and Solid State Electronics, Jilin University
2021	Ph. D. in Nanoengineering, University of California San Diego

PUBLICATIONS

1. **Hui Zheng**, Richard Tran, Xiang-Guo Li, Balachandran Radhakrishnan, Shyue Ping Ong. "Role of Zr in strengthening $MoSi_2$ from density functional theory calculations", Acta Materialia 2018, 145, 470–476.

2. **Hui Zheng***, Xiang-Guo Li*, Richard Tran, Chi Chen, Matthew Horton, Donald Winston, Kristin Aslaug Persson, Shyue Ping Ong. "Grain boundary properties of elemental metals", Acta Materialia 2020, 186, 40–49. (*These authors contributed equally)

3. **Hui Zheng**, Luke Nibbelink, Xiang-Guo Li, Yunxing Zuo, Chi Chen, Shyue Ping Ong "Predictive processing of NbMoTaW multi-principal element alloy to tune short-range order and mechanical properties". In preparation.

ABSTRACT OF THE DISSERTATION

Defect effects on mechanical properties and deformation behavior of materials: from quantum mechanics to molecular dynamics assisted by machine learning

by

Hui Zheng

Doctor of Philosophy in NanoEngineering

University of California San Diego, 2021

Professor Shyue Ping Ong, Chair

The defects of materials have a significant impact on their mechanical properties and deformation behavior. For example, defects can sabotage desired strength or ductility, but they can also strengthen the materials if the proper element and defects combination is selected. This thesis will discuss the impacts of various defects on the mechanical properties of structural materials ranging from intermetallic to elemental metals and multi-principal element alloys (MPEAs).

First, in chapter 2, the impacts of defects on the brittleness of intermetallic were studied using density functional theory (DFT) calculations in the $MoSi_2$ model system. The application of $MoSi_2$ is limited by the oxygen embrittlement at temperatures of 400-600 °C. Our DFT

calculations verified the fact the oxygen interstitials (O_{int}) are the main detrimental defects for grain boundary intergranular fracture. We found that Zr substitution defects (Zr_{Mo}) reduce the embrittling effects of oxygen interstitials at $MoSi_2$ grain boundaries by being a charge donor to oxygen. However, a more substantial effect is observed when Zr is present as a secondary getter nanoparticle phase. Oxygen interstitials have a strong thermodynamic driving force to migrate into the Zr subsurface at the Zr/MoSi2 interface, and the energy penalty for breaking the oxygen-contaminated Zr/$MoSi_2$ interfaces are much higher than that of $MoSi_2$ grain boundaries. Thus, the introduction of Zr into $MoSi_2$ can mitigate the embrittling effect of oxygen on grain boundary fracture.

In chapter 3, we further investigated the GBs effects of a broader class of materials. We constructed the largest DFT-computed GB database using the high-throughput workflow to overview GB energies distribution of different elemental systems. The database encompasses 327 GBs of 58 elemental metals, including ten typical twist and symmetric tilt GBs for bcc and fcc metals and Σ7(0001) for hcp metals. Using this large GB dataset, we develop an improved predictive model for the GB energy of different elements based on the cohesive energy and shear modulus. The open GB database would help guide the future design of polycrystalline materials.

Nevertheless, DFT calculations are too expensive for simulating large systems or the longtime dynamic evolution of materials under certain conditions. Classical molecular dynamics (MD) simulation is a good alternative for the dynamic evolution of materials if an accurate interatomic potential (IAP) is available. The recently developed machine learning interatomic potential (ML-IAP) for bcc MoNbTaW multi-principal element alloy (MPEA) facilitates MD simulations to achieve high accuracy with low computational cost. In chapter 4, we applied the ML-IAP to explore the performance of materials under heat treatment and tensile/compressive deformation. We found that differences in annealing temperatures introduced different degrees of local chemical short-range orders (SROs) in MPEA. The presence of SROs influences the corresponding stacking fault energy, critical resolved shear stress of dislocation, and therefore the

strength and ductility of MPEA under the uniaxial tensile/compressive tests.

Chapter 1

Introduction

1.1 Background

Many materials applied in the automobile, aerospace, energy industry are not pure single crystals. Instead, most of the materials are polycrystalline and inevitably or purposely include various defects. The defects in materials are a double-edged sword; it can lead to catastrophic damage to the material and can also improve the properties of materials.

The effects of various defects on the properties of materials can be explored using quantum mechanical computational modeling based on density functional theory (DFT). The fast-growing computational power and automated workflow enable the DFT calculations to be employed in a high-throughput fashion. The systematically generated database of specific properties can be used to construct structure-property relationships in metals and potentially aid new alloy design.

Recently, the development of machine learning interatomic potentials (ML-IAPs) enables classical molecular dynamics (MD) modeling to achieve a highly accurate energy and force prediction. With the toolkit, we can explore the dynamic structure evolution using long-time (ns scale) MD for large-scale structures under various conditions.

This thesis will use first-principle calculations and classical MD modeling to explore the influences of various defects on intermetallics $MoSi_2$, elemental metals, and quaternary equimolar multi-principal element alloys (MPEAs) MoNbTaW. The remainder of this chapter introduces various defects covered in this thesis and the strengthening mechanisms related to these defects. This chapter will conclude with an overview of each project.

1.2 Defects and strengthening mechanisms

The mechanical properties of materials are greatly influenced by defects, the interactions between various defects, and the distribution of defects. This section will briefly summarize various defects explored in this thesis and their effects on materials properties.

1.2.1 Point defects

Points defects include vacancy, interstitial, and substitutional defects etc. Vacancies are the simplest point defects and are ubiquitous in crystalline solids. The energy needed to form a vacancy is often called vacancy formation energy E_v (unit eV/defect). The equilibrium number of vacancies N_v increases with temperature T [9], according to

$$N_v = N\,exp(-\frac{E_v}{kT}) \tag{1.1}$$

N is the total number of atoms, T is the absolute temperature in kelvins, and k is the Boltzmann's constant. The number of vacancies increases exponentially with increasing temperature and decreasing vacancy formation energy E_v. Therefore, we can apply heat treatment to control the number of vacancies in the material of interest.

Atoms in solid materials are in constant motion. When there is a vacancy in the adjacent site, and if the thermal vibrational energy is large enough to break the bond and cause lattice distortion, the atom can exchange positions with the neighbor vacancy, known as vacancy diffusion. The diffusion coefficient D is used to indicate the rate of atomic motion; it depends on both host and diffusing species and temperature. Temperature dependent diffusion coefficient D is:

$$D = D_0\,exp(-\frac{E_a}{kT}) \tag{1.2}$$

where D_0 is temperature-independent pre-exponential (m^2/s) and E_a is the activation energy for diffusion (eV). The activation energy E_a is the energy required to enable the diffusive motion of one atom. The larger the E_a, the smaller the diffusion coefficient D. Similarly, the higher temperature and smaller E_a contribute to larger D. Therefore, heat treatment can be used to control the vacancy density, the rate of diffusion and further control the local composition, and tune the properties of materials.

1.2.2 Linear defects: dislocations, the leading carriers of plastic deformation

A dislocation is a linear (one-dimensional) defect around which some of the atoms are misaligned[9]. There are two pure types of dislocation: edge and screw dislocation. Edge dislocation is one extra half-plane of atoms being squeezed out of the perfect crystal under shear stress. Screw dislocation is one atomic plane shifted one atomic distance relative to the initial perfect crystal around the dislocation line and forming a helical/spiral path. Most of the dislocations found in crystalline materials exhibit both screw, and edge characters, and are called mixed dislocations. Burgers vector is used to specify the direction and magnitude of lattice distortion due to the presence of dislocation. In crystalline materials, plastic deformation most often involves the motion of dislocation. It corresponds to the movement of a large number of atoms under applied stress. This process involves bond breaking and reforming. Therefore, restricting the dislocation motion leads to the increased hardness and strength. Alloying, which is a typical method to strengthen materials, could attribute solid-solution strengthening. The aforementioned point defects such as interstitial and substitutional defects disrupt the local structure of materials, create local lattice strain, which inhibits the dislocation motion.

The dislocation-dislocation interaction can strengthen the material through strain hardening. During plastic deformation, dislocation density increases, the average distance between adjacent dislocations decreases. Because the strain field from dislocation-dislocation interaction is, on average, repulsive, the dislocation mobility becomes more restricted; thus, the hardness and strength of metal increase. Next, we will introduce various planar defects, which are also the barriers to dislocation motion.

1.2.3 Planar defects

The common planar defects in polycrystalline materials include stacking fault (SF), anti-phase boundaries, grain boundaries, etc. SF comes from the disruption of the normal stacking sequence in crystalline materials. It is quantified by the stacking fault energy (SFE), which is the energy difference between the structure with SF and the initial perfect structure per unit area. SFE is the measure of the resistance of dislocation glide under plastic deformation. Typically, dislocations prefer to move on the densest plane (slip plane) and along the direction (slip direction) with the highest linear density. $\{110\} < 111 >$ represents the most favorable slip plane and direction combination (i.e., slip system) for bcc alloys. Other possible slip systems for bcc crystal also include $\{112\} < 111 >$ and $\{123\} < 111 >$.

In MPEAs, another type of planar defect called anti-phase boundary (APB) is formed by translating half of the crystal relative to the other half. APB leads to different bonding configurations compared with the initial bonding configuration. The difference between the APB and SF is that APB only causes chemical disorders without stacking disorder, while SF causes both chemical and stacking disorders. The anti-phase boundary energy (APBE) is quantified by the energy difference between the translated and initial structure per unit area. The motion of dislocation needs to overcome the energy from SF and APB in MPEAs.Therefore, increase the SFE and APBE through local composition tunning in MPEAs is one applicable method to increase the strength of MPEAs.

In polycrystalline materials, the boundary joining two adjacent grains which have different orientations are grain boundary (GB)[10]. There are various degrees of bond distortion/breaking at the GB region compared to the perfect bulk crystal. The energy penalty needed to distort/break bonds to form GB is defined as GB energy. Different GBs have different GB energies, and various GBs form a three-dimensional net spreading through the material. Therefore, GBs have a substantial influence on polycrystalline materials. For example, the GB regions have excess volume than the bulk region. Thus, GB tends to interact with other defects such as impurity atoms

to lower the total energy. The accumulation of certain types of species at the GB region is GB segregation, resulting in embrittlement[11] or can be used to improve the ductility.

GB net can also hinder the movement of dislocation, therefore, strengthening the materials. The strengthening extent depends on the energy required for dislocations to break through these defects that blocked their movement. There is an inevitable trade-off between the strength and ductility in conventional metals when the strengthening mechanisms mentioned above are employed. However, in MPEAs, it is promising to overcome the strength-ductility trade-off because the presence of twin boundaries enables some partial dislocations to glide along the twin boundaries, which relieved the stress from dislocation pile-up to some extent[12].

1.3 Solid solution strengthening

Most metals in applications do not consist of only one type of atom; they include impurity or purposely introduced foreign atoms. The solid solution (alloying) is created by adding a significant amount of secondary species into the original host metal, forming a homogenous chemical mixture. The size difference between the host and impurity species results in local lattice distortions, which obstruct the migration of dislocations, strengthening the alloys. Alloying had been used to improve mechanical strength since the Bronze Age, which is named after the widespread use of bronze, an alloy consisting of primary Cu alloying with Sn, Al, Mn, Ni, Zn, etc. Unlike traditional alloying, which only has one primary base metal, a new alloying strategy of multiple alloying elements in near-equiatomic proportion was proposed and experimentally presented in 2004 by Yeh et al.[13] The multi-principal element alloys (MPEAs) usually form a single-phase alloy, and have better mechanical properties than traditional alloys. As there are multiple principal elements, there is no obvious solute or solvent. Nevertheless, the local lattice strain exists due to the size difference of different elements. The new alloying strategy significantly increases the tunable composition space for alloy design.

1.4 Atomic-scale materials modeling

Throughout this thesis, we used two types of atomic-scale modeling methods to explore the structures and evolution of various defects discussed in the previous section. This section will briefly introduce these two methods, the quantum mechanical modeling method, and classical molecular dynamics simulation.

1.4.1 Quantum-mechanical computation

The quantum mechanical wavefunction contains all the information, such as the allowed energy states of a system. In principle, we can get the wavefunction by solving the Schrödinger equation. However, it is impossible to solve the many-body Schrödinger equation. Therefore, density functional theory (DFT) is introduced to obtain an approximate solution to the many-body Schrödinger equation by solving the Kohn-Sham equations[14]. The increasing computational power enabled us to calculate the effects of defects, especially interfacial defects, on the properties of materials.

1.4.2 Classical molecular dynamics simulation

The classical molecular dynamics (MD) simulation method is used to explore the evolution of atoms within a period of time. The trajectories of atoms are determined by solving Newton's equations of motion. The potential energy and force of atoms are calculated using interatomic potentials (IAPs). Therefore, the accuracy of the potential directly affects the simulation results and the physical conclusion based on calculations. Recently, machine learning has been successfully used to develop the interatomic potentials (ML-IAPs), achieved a highly accurate relationship between local environment descriptors and the potential energy surface. Recently developed ML-IAP for MoNbTaW MPEA has great accuracy in calculating defect properties such as dislocation structure, interface energy, etc. As such, it will be selected to explore the

effects of various defects on the MPEA.

1.5 Objectives and projects summary

In this thesis, we will explore the effects of various defects and their interactions on mechanical properties in intermetallic $MoSi_2$. We will present the grain boundary energy distributions of 58 common metals with bcc, fcc, or hcp structures from the GB database generated base on DFT calculations. We will also reveal the mechanisms of different strengthening mechanisms using highly accurate ML-IAP for equimolar MoNbTaW MPEA.

This thesis includes three projects organized into three chapters.

Chapter 2 presents the oxygen interstitial point defects that can cause embrittlement of intermetallic $MoSi_2$. Introducing Zr as substitutional point defects mitigates the detrimental effects from oxygen interstitial defects at $MoSi_2$ grain boundaries by being a charge donor to oxygen. However, introducing Zr as a secondary getter phase has a more substantial effect compared to Zr substitution to Mo. As the strengthening mechanism of introducing Zr involves the formation of ZrO_2 and $ZrSiO_4$ as the passivation from further oxidation. We designed an efficient screening approach to identify other potential getter elements using simple thermodynamic reaction descriptors, which can be extended to other alloy systems of interest.

Chapter 3 introduces the largest database of grain boundary properties of elemental metals based on DFT calculations. The database currently encompasses 327 GBs of 58 elemental metals, including 10 common twist or symmetric tilt GBs for body-centered cubic (bcc) and face-centered cubic (fcc) systems and the $\Sigma 7$ [0001] twist GB for hexagonal close-packed (hcp) systems. We develop an improved predictive model for the GB energy of different elements based on the cohesive energy and shear modulus using this large GB dataset. The availability of GB energies of various elements enables analysis for GB segregation preference in various alloys, which would help guide the future design of polycrystalline materials.

Chapter 4 presents the application of the machine learning interatomic potential (ML-IAP) for MoNbTaW multi-principal element alloys (MPEAs). The local chemical short-range orders (SROs) can be achieved from heat treatment. Higher values of SROs can increase various defect formation energies, such as stacking fault energies (SFEs), anti-phase boundary energies (APBEs), and the critical resolved shear stresses (CRSS) of screw dislocation, as well as the ruggedness of spatial SFE and APBE landscapes. This rugged energy landscape introduces more friction for dislocation migration, therefore, strengthening the MPEA. Uniaxial tensile and compressive strains were applied to samples with different degrees of SROs, and the samples with higher SROs correspond to higher ultimate tensile stress and ductility under deformation. The improved ductility is attributed to the twinning mechanism. The interaction between coherent twins and dislocations can decrease the stress from dislocation pile-up under tension. These results present a promising way to tune the mechanical properties of MPEAs through temperature-controlled chemical SROs.

Chapter 2

Role of Zr in strengthening $MoSi_2$ from density functional theory calculations

2.1 Introduction

Molybdenum disilicide ($MoSi_2$) is a refractory intermetallic with important high-temperature applications such as heating components, thermal barrier coatings, and turbine engines. This is due to its high melting point (2030 °C)[15,16], moderate density (6.24 g/cm3)[16] and excellent resistance to oxidation at high temperatures up to 1600°C due to the formation of a protective coating of SiO_2[16]. However, a major impediment to the widespread application of $MoSi_2$ is its inherent brittleness at intermediate temperatures (400-600 °C)[17,18]. It has been suggested that the primary cause is grain boundary embrittlement caused by short-circuit diffusion of O2, a phenomenon known as pesting[16,18].

A common approach to suppress pesting in $MoSi_2$ and other Mo-based intermetallics (such as Mo_3Si and Mo_5SiB_2) is by alloying with "getter" materials, i.e., materials that preferentially react with parasitic oxygen, to improve ductility. These getters commonly exist as nanoparticles embedded in the Mo and Mo-based alloy matrix[19,20]. Examples of ductilizing components include light elements (B, C, Al, Mg)[21–29], transition metals (Zr, Ti, V, Nb, Re, Hf)[20–23,26–28,30–33], the rare earth metal Er[34] and oxides (La_2O_3, Y_2O_3, Sc_2O_3 and $MgAl_2O_4$)[35–38]. In particular, Zr is one of the most commonly used getters that has been shown to efficiently reduce the embrittling effect of O in Mo and Mo-based systems[20–23]. Zr addition increases both ductility and strength in Mo-Si solid solutions and single-phase Mo-1.5Si alloy. Previous experiments on Mo–1.5 at.% Si alloys have attributed these beneficial effects to three reasons[23]. First, Zr addition reduces the grain size of the alloy. Second, Zr reacts with oxygen to form ZrO_2 particles, which can pin the GBs. Finally, Zr reduces the concentration of Si segregation at the GB through the formation of $ZrSiO_4$[15,38,39].

First-principles calculations using density functional theory (DFT)[26,40–43] are an important complementary probe to experiments in studying the effects of dopants/impurities and heterogeneous interface in alloys. For example, Lenchuk et al. have explored the influence of

Zr and Si on the strength of pure Mo GBs[43–45]. Their results show that although the presence of Zr and Si results in a lower work of separation in Mo tilt Σ5 (310) [001] and twist Σ5 [001] GBs[44], the formation of an ultrathin film of ZrO_2 results in a higher work of separation[45]. The embrittling effects of Zr and other impurities in pure Mo GBs have also been studied in a recent comprehensive investigation by Tran et al[46]. For $MoSi_2$, Waghmare et al.[26] have shown that the substitution of Mo by V or Nb, and substitution of Si by Mg or Al in $MoSi_2$ single crystals can improve ductility using DFT calculations[26]. We note that these previous studies either focus on just pure Mo metal, or on substitutional dopants in bulk $MoSi_2$; the mechanisms behind the strengthening effects of Zr on the GB and interfaces of Mo-Si alloys remain an important open question.

In this work, we attempt to address this question by comprehensively exploring multiple mechanisms for Zr incorporation into $MoSi_2$ and its interplay with embrittling oxygen contaminants using DFT calculations. We will show that Zr as a dopant has an inherent embrittling effect in the $MoSi_2$ GBs, but a mitigating effect on oxygen embrittlement at sufficiently high concentrations by acting as a charge donor. We will also show that Zr as a getter nanoparticle significantly enhances the inherent strength of $MoSi_2$ while mitigating the detrimental effects of oxygen impurities. Finally, we will discuss the implications of these findings for the future development of Mo and other alloys, and outline a simple computational approach to screen for other potential getter materials for both Mo and other structural materials using the Materials Project database[47–49].

2.2 Methods

2.2.1 DFT calculations

All DFT calculations were performed using the Vienna ab initio Simulation Package (VASP)[14,50] within the projector augmented wave (PAW) approach[51]. The exchange-correlation

interactions were modeled using the Perdew-Berke-Ernzerhof (PBE) generalized gradient approximation (GGA) functional[52]. All calculations were spin-polarized, and a plane-wave cutoff energy of 400 eV was used. The energies and atomic forces were converged within 5×10^{-4} eV and 0.02 eV/Åsrespectively. Consistent k-point grids of $4\times4\times1$, $2\times2\times1$ and $1\times1\times1$ were used for the 1×1, $\sqrt{2}\times\sqrt{2}$ and 2×2 ((scalefactors refer to just the GB/interface plane)) supercell GB models, respectively. For the α-Zr/$MoSi_2$ and β-Zr/$MoSi_2$ interfaces, gamma-centered k-point grids of $1\times1\times1$ and $4\times4\times1$ were used, respectively. All the *k*-point grids have a density of at least 14 / $Å^{-1}$ in the GB/interface plane, and convergence tests with respect to both energy cutoff and *k*-point grid (Figure A.1) show that the work of separation, the main quantity of interest in this work, is converged to within 0.02 J/m^2. The lattice parameters and atomic positions were fully relaxed for the undoped GB and interface structures, while only the atomic positions were relaxed for the cleaved and doped structures. The construction of all structural models and all analyses were performed using the Python Materials Genomics (pymatgen) library[47].

2.2.2 Derived quantities

Several quantities are derived from the DFT energy calculations to assess the influence of Zr on the mechanical properties of $MoSi_2$.

Grain boundary/Interface energy. The GB/interface energy is used to determine the most stable grain boundary or interface, and is given by the following expression:

$$\gamma_{GB/interface} = \frac{E_{GB/interface} - \sum_L E_{bulk(L)} - \sum_i \Delta n_i \mu_i}{NA_{GB/interface}} \tag{2.1}$$

where $E_{GB/interface}$ is the energy of the supercell containing the GB/interface; $E_{bulk(L)}$ is the energy of the corresponding bulk material L ($MoSi_2$ or Zr); μ_i is the chemical potential of species i; Δn_i is the difference in the number of atoms of species i between the GB/interface supercell and the bulk; N is a normalization constant to account for the number of GB/interface.

For a stoichiometric GB/interface, Δn_i=0 for each species. For non-stoichiometric GB/interfaces, $\sum_i \Delta n_i \mu_i$ is calculated by considering the chemical potential range of interest as outlined by Wei et al.[53], and the corresponding lower bound is listed in Table 2.1.

Table 2.1: Grain boundary energies (γ_{GB}) and interface energies ($\gamma_{interface}$) with different terminations.

GB	γ_{GB} (J/m^2)
Si-Si	2.50
Mo-Mo	1.95
Mo-Si	2.60
Interface (Zr/$MoSi_2$)	$\gamma_{interface}$ (J/m^2)
Zr-Si	0.33
Zr-Mo	1.15

Dopant formation energy. The dopant formation energy E_d is used to determine the most favorable site for a particular dopant (O or Zr). The expression for E_d is given as follows:

$$E_d = E^{doped}_{bulk/GB/interface} - E^{pristine}_{bulk/GB/interface} - \sum_{i=1} n_i \mu_i \tag{2.2}$$

where $E^{pristine}_{bulk/GB/interface}$ and $E^{doped}_{bulk/GB/interface}$ are the energies of the clean and doped bulk/GB/interface, respectively. n_i is the number of species i being added ($n_i \geq 0$) or removed ($n_i \leq 0$) to form the doped structure, and μ_i is corresponding chemical potential of species i. In this work, $MoSi_2\mu_i$ is approximated by the calculated energy per atom of the elemental species i, e.g., solid Zr/Si/Mo and gaseous O_2 to determine dopant site preferences. The energy of gaseous O_2 was obtained via fitting to reproduce the formation energies of main group oxides, in line with the approached detailed by Wang et al.[54].

Work of separation. The mechanical strength of GBs/interfaces is characterized by the work of separation W_{sep}, which is defined as the energy difference between the cleaved

GB/interface ($E^{cleave}_{GB/interface}$) and the uncleaved GB/interface ($E^{uncleave}_{GB/interface}$) normalized by the surface area AGB/interface[45], as follows:

$$W_{sep} = \frac{E^{cleaved}_{GB/interface} - E^{uncleaved}_{GB/interface}}{nA_{GB/interface}} \tag{2.3}$$

Here, n is a normalization constant to account for the number of interfaces cleaved. For the GB structures, a single GB is cleaved by introducing a vacuum layer. For the Zr/$MoSi_2$ interface, two interfaces were cleaved to form four surfaces (see later section).

2.3 Results

The focus of this work is on the effect of Zr on the strength of oxygen-contaminated $MoSi_2$, both as a dopant in the GBs, as well as a getter nanophase. Two different structural models as shown in Figure 2.1, were used to explore these effects. The conventional unit cell of tetragonal $C11_b$ $MoSi_2$ [space group: I4/mmm (No.139)] shown in Figure 2.1(a) with fully relaxed DFT lattice parameters of a = 3.220 Å and c = 7.877 Å was used as a fundamental unit in both models. $MoSi_2$ comprises repeating layers of -Si-Mo-Si- atoms. As shown in Table 2.1, the Si-terminated $MoSi_2$ slab provides the lowest energy $\gamma_{GB/interface}$ for both the GB as well as the Zr/$MoSi_2$ interfaces. All subsequent analysis will henceforth utilize the Si-terminated $MoSi_2$ GB/interfaces.

2.3.1 Structural model for $MoSi_2$ GB

To explore the effect of Zr as a dopant, the Σ5 (001) twist GB of $MoSi_2$ (henceforth, the term GB in this work is used to refer to this specific GB) was constructed using the coincident site lattice (CSL) model[55], as shown in Figure 2.1(b, c). Each model contains two grains forming two equivalent GBs due to periodic boundary conditions. To minimize the interactions between GBs, each grain comprises two unit cells along the direction perpendicular to the GB plane, with

approximately 16 Å separating the two GBs. After full relaxation, the lattice parameters of $MoSi_2$ GB are a = 7.182 Å and c = 32.714 Å.

For doped GBs, equal number of dopants were introduced on both sides of the GB, i.e., both sides of green line within the green dashed line box in in Figure 2.1(c), to ensure that a non-polar surface model is created after cleavage. This is of critical importance to exclude the effect of dipole interactions across periodic boundary images. It is assumed that any defects introduced is charge-compensated by changes in the Mo or Si oxidation states, i.e. no background charge is applied in the calculations. In all cases, all symmetrically distinct dopant configurations within the 1×1 GB were evaluated, and the lowest energy configuration was used as the basis for analysis. All the configurations and their corresponding energies are provided in Figure A.2 and Table A.1. Different impurity coverages were achieved by using the $\sqrt{2} \times \sqrt{2} \times 1$ (240 atoms) and $2 \times 2 \times 1$ (480 atoms) supercells of the GB model from Figure 2.1(c) (120 atoms), while ensuring that the distances between dopants are maximized and the local environment around each dopant is similar to that of the relaxed 1×1 cell.

2.3.2 Site preference of single O and Zr dopant in bulk $MoSi_2$

To understand the site preference of Zr and O dopants/impurities in $MoSi_2$, we first calculated the dopant formation energies for Zr/O substitution on the Mo and Si site (Zr_{Mo}, Zr_{Si}, O_{int}, and O_{Si} in Kröger–Vink notation) and O substitutional defects on the Si site (O_{Si}) and Zr/O interstitials (Zr_{int} and O_{int}). Table 2.2 shows the calculated dopant formation energies (E_d) of four types of single dopant in $\sqrt{5} \times \sqrt{5} \times 4$ supercell of bulk $MoSi_2$, which has approximately the same dimensions as the $MoSi_2$ GB model. We find that Zr prefers to substitute on the Mo site rather than the Si site in $MoSi_2$, which is unsurprising given that the atomic radius of Zr (1.55 pm) is much closer to that of Mo (1.45 pm) than Si (1.1 pm). For oxygen impurities, we find that the formation of the oxygen interstitial is much more favorable than substitution on the Si site. This is consistent with previous XPS results showing O signals in the high binding energy region

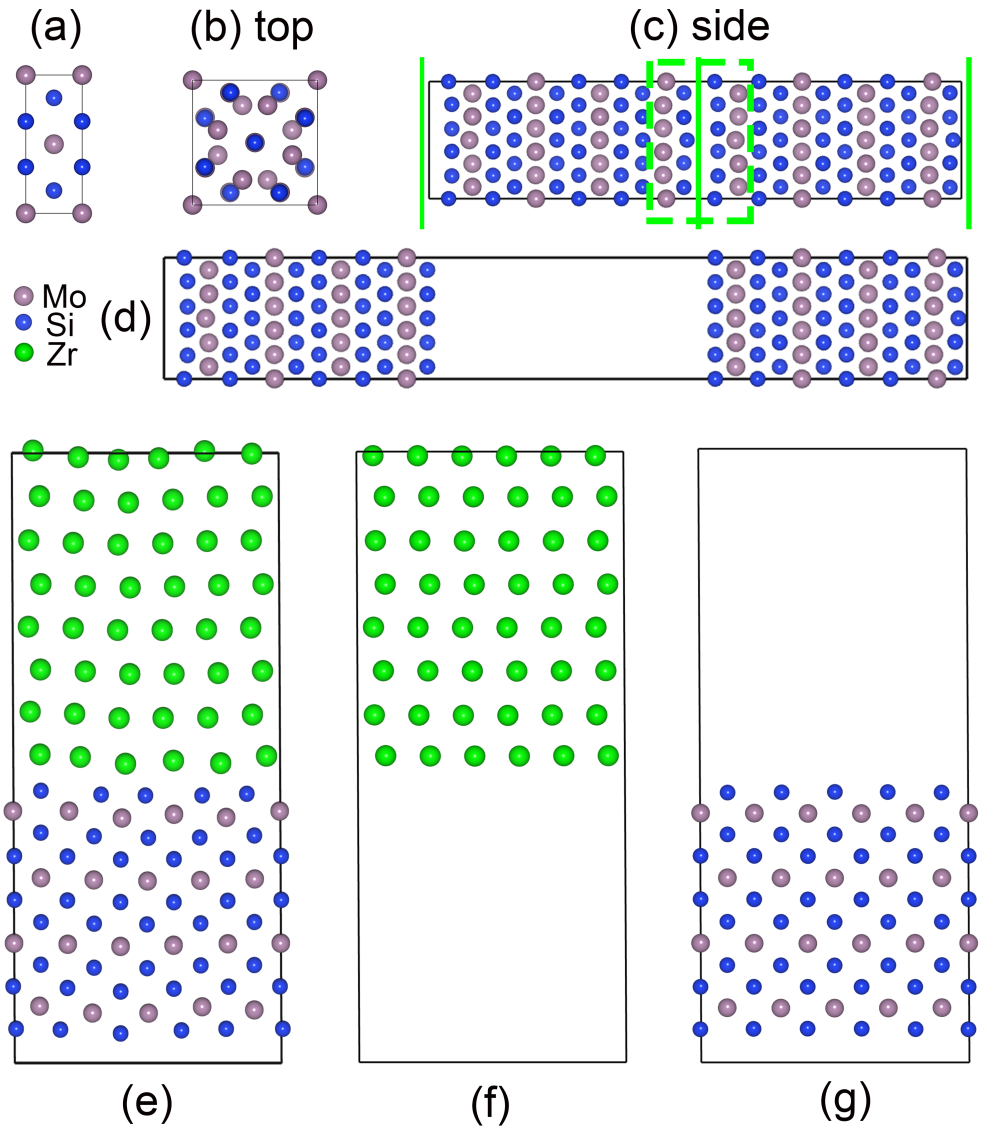

Figure 2.1: Models of the clean structures used in this work. (a) Conventional unit cell of tetragonal C11b $MoSi_2$ (space group: I4/mmm). (b) Top view and (c) side view of the $MoSi_2$ $\Sigma 5$ (001) twist grain boundary model, with the green lines illustrating the periodicity of the GB. The sites in the green dashed line box show substitutional and interstitial sites considered. (d) "Cleaved" $MoSi_2$ GB, with a vacuum layer of thickness 15 Å into the GB model. (e) α-Zr/$MoSi_2$ interface model. (f) Zr and (g) $MoSi_2$ slabs obtained after cleaving α-Zr/$MoSi_2$ interfaces.

from interstitial oxygen in $MoSi_2$[56]. O_{int} is also recognized as one of the causes of brittleness of $MoSi_2$-Mo_5Si_3 composite microstructures[34]. In the remainder of this work, we will therefore focus on Zr_{Mo} and O_{int} as the primary defects of interest.

Table 2.2: Dopant formation energy (E_d) of four types of dopant in bulk $MoSi_2$

Type of dopant	E_d(eV)
Zr_{Si}	1.98
Zr_{Mo}	1.29
Zr_{int}	7.74
O_{Si}	1.07
O_{Mo}	5.47
O_{int}	0.54

2.3.3 Zr effect on O embrittlement of $MoSi_2$ GB

The effects of Zr and O dopants on the strength $MoSi_2$ GB were studied by introducing Zr_{Mo} and O_{int} in the Σ5 (001) twist GB of $MoSi_2$ (Figure 2.1(c)). Potential oxygen interstitial sites in the $MoSi_2$ GB were identified using a Voronoi tessellation method[57]. Three dopant compositions were considered:

- Four O_{int} (two on each side of the GB).
- Two Zr_{Mo} (one on each side of the GB).
- Four O_{int} and two Zr_{Mo} (one ZrO_2 on each side of the GB).

Figure 2.2 summarizes the calculated work of separation W_{sep} for the clean GB and doped GB with different dopant compositions at three coverages. To calculate W_{sep}, a 15 Å thick vacuum layer is inserted into one of the periodic regions shown by the green line in Figure 2.1(c) to

generate the "cleaved" model in in Figure 2.1(d). We have considered all distinct cleavages for each model (see Figure A.2 and Table A.1), and plotted the lowest W_{sep} in Figure 2.2. We may observe that Zr_{Mo} has a mild strengthening effect on the Σ5 (001) twist GB of $MoSi_2$, though this effect becomes progressively weaker at higher coverages. W_{sep} increases from 2.15 J/m^2 for the clean GB to around 2.16 J/m^2, 2.21 J/m^2 and 2.23 J/m^2 at a coverage of 2 Zr_{Mo} per 51.6 Å^2, 103.0 Å^2, and 206.3 Å^2. Oxygen interstitials, however, have a significant embrittling effect on $MoSi_2$ GBs. W_{sep} drops precipitously by 34.42% to 1.42 J/m^2, even at an high coverage of 4 O_{int} per 51.6 sÅ^2. As the oxygen coverage decreases, the detrimental effect of oxygen also decreases.

The most interesting result comes from comparing the W_{sep} of the 4 O_{int} + 2 Zr_{Mo} configuration with that of the 4 O_{int} and 2 Zr_{Mo} configurations. We find that even though both O_{int} and Zr_{Mo} are predicted to have an embrittling effect on the $MoSi_2$ GB, the W_{sep} of the 4 O_{int} + 2 Zr_{Mo} is higher than that of the 4 O_{int} at intermediate and high coverages. This result indicates that the presence of Zr in the $MoSi_2$ GB mitigates the severe embrittling effect of the O_{int} at $MoSi_2$ GBs.

2.3.4 Structural model for Zr/$MoSi_2$ interface

To explore the effect of Zr as a secondary getter nanophase, a Zr/$MoSi_2$ interface model was constructed by interfacing the (0001) surface of α-Zr (hcp) with (001) Si-terminated $MoSi_2$. The pesting effect of $MoSi_2$ that results in formation of MoO_3 and SiO_2 is the strongest at 500°C[17,18] where Zr is in its α phase. It should be noted that β-Zr undergoes a phase transition to the β bcc phase at 863°C.[58], which is within the temperature range where problematic formation and evaporation of MoO_3 occurs[59]. We have done a similar study using the (110) surface of β-Zr as well, and the results are qualitatively similar. As such, we will focus our discussion on the α-Zr, and the corresponding results for the β phase are available in the Supplementary Information. The α-Zr/$MoSi_2$ model was constructed using a search algorithm to minimize the lattice mismatch while keeping the total number of atoms in the model to around 500 atoms. The resulting model

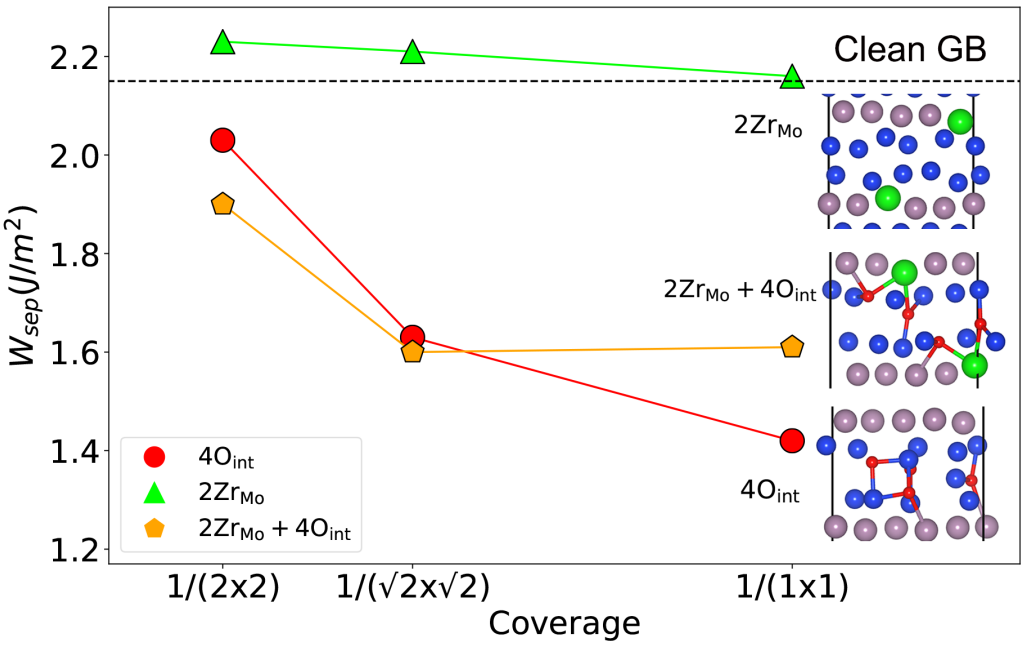

Figure 2.2: Work of separation W_{sep} of $\Sigma 5$ (001) twist GB of $MoSi_2$ with $4O_{int}$, $2Zr_{Mo}$, and $(4O_{int} + 2Zr_{Mo})$ with respect to coverage (supercell size in the GB plane). The cross-sectional area of the three coverages are 51.6 Å (1×1), 103.0 Å $(\sqrt{2} \times \sqrt{2})$ and 205.9 Å 2. Colored lines between points are drawn merely to guide the eyes. The Wsep of the clean GB is indicated by the black dashed line. The atomic models for the doped GB for the $1/(1 \times 1)$ coverage are shown.

comprises a $MoSi_2$ supercell of 300 atoms interfaced with an α-Zr supercell of 240 atoms (Figure 2.1(e)). The lattice mismatch is less than 5% (0.64% along a, 4.58% along b). Several relative shifts of the $MoSi_2$ and Zr supercells were investigated, and the lowest energy configuration was used in subsequent studies. After a full relaxation, the lattice parameters are 16.32 Å, 16.14 Å and 36.91 Å in the a, b and c directions, respectively.

2.3.5 Relative oxygen affinities of Zr and $MoSi_2$

The relative O affinities of Zr and $MoSi_2$ were probed by inserting a single O_{int} at various symmetrically distinct locations in the Zr/$MoSi_2$ interface model, and performing a DFT relaxation of the atomic positions only. Figure 2.3 plots the relative energies (ΔE) of the O_{int}-doped α-Zr/$MoSi_2$ interface against the distance from the interface. The corresponding results for the β-Zr/$MoSi_2$ interface are given in Figure A.3. It is clear that O_{int} has a strong thermodynamic driving force (∼6 eV) to move from $MoSi_2$ to Zr. Interestingly, the lowest energy position for the O_{int} is in the subsurface region between the two Zr layers closest to the α-Zr/$MoSi_2$ interface (position 10 in Figure 2.3). These results confirm the effectiveness of Zr as a getter for O contaminants in $MoSi_2$. Furthermore, nanoparticles with high surface area to volume ratio would be the most effective getter, consistent with experimental findings[60].

2.3.6 Mechanical properties of the clean and O-contaminated α-Zr/$MoSi_2$ interface

The W_{sep} of the Zr/$MoSi_2$ interface (Figure 2.1(e)) was calculated by cleaving both interfaces to form Zr and $MoSi_2$ slabs (Figure 2.1(f)(g)). Similar to the GB study, different cleavages of the Zr/$MoSi_2$ interface were considered (Table A.6), and the lowest W_{sep} for the doped and undoped Zr/$MoSi_2$ interfaces are plotted in Figure 2.4. We observed that not only do the undoped α-Zr/$MoSi_2$ and β-Zr/$MoSi_2$ interfaces have higher W_{sep} than the clean $MoSi_2$ GB,

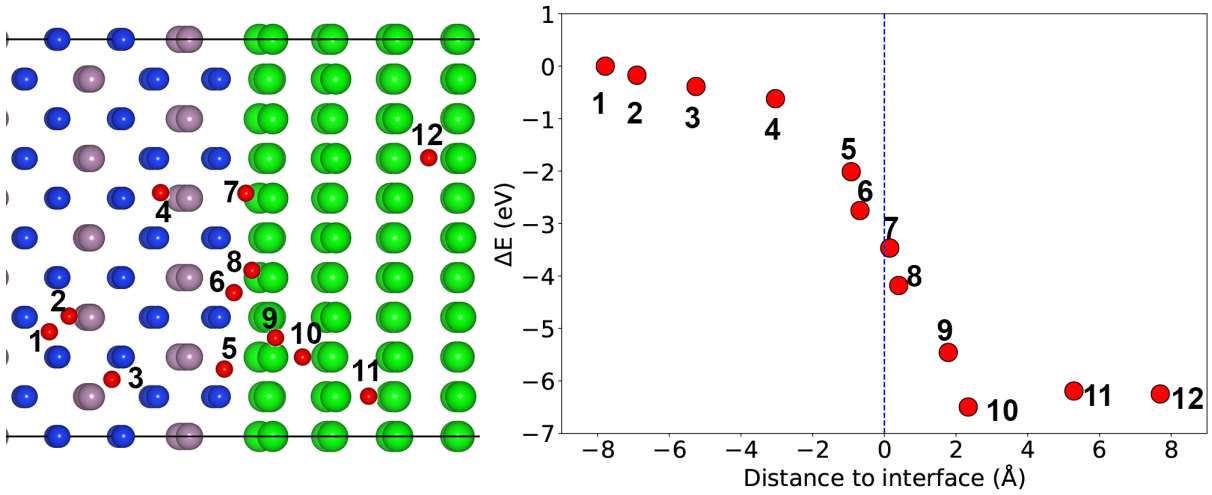

Figure 2.3: Relative energies (ΔE) of one O_{int} defect at different regions of α-Zr/MoSi2. The zero of the energy is set at the energy of the structure with O_{int} in bulk-like $MoSi_2$ (position 1).

but the α-Zr/$MoSi_2$ and β-Zr/$MoSi_2$ interfaces contaminated with 4 O_{int} also have substantially higher W_{sep} than the clean $MoSi_2$ GB. In other words, the presence of Zr as a secondary phase not only preferentially absorbs O interstitial contaminants, the Zr/$MoSi_2$ interface, whether oxygen contaminated or not, is also substantially stronger (higher W_{sep}) than $MoSi_2$ GBs. It should also be noted that the observed changes in W_{sep} are much larger in magnitude compared to variations in surface energies as a result of strain (see Table A.7).

2.4 Discussion

From the results above, we have provided clear evidence from first principles calculations of the multiple mechanisms in which Zr mitigates oxygen-caused embrittlement in $MoSi_2$.

2.4.1 Zr as a dopant

At high coverages, the presence of Zr dopants has a mitigation effect on O-contaminated $MoSi_2$ GBs; the work of separation W_{sep} of the 2 Zr_{Mo} + 4 O_{int} doped GB is higher than that of the 4 O_{int}-doped GB. We performed electron localization function (ELF) and Bader analysis to

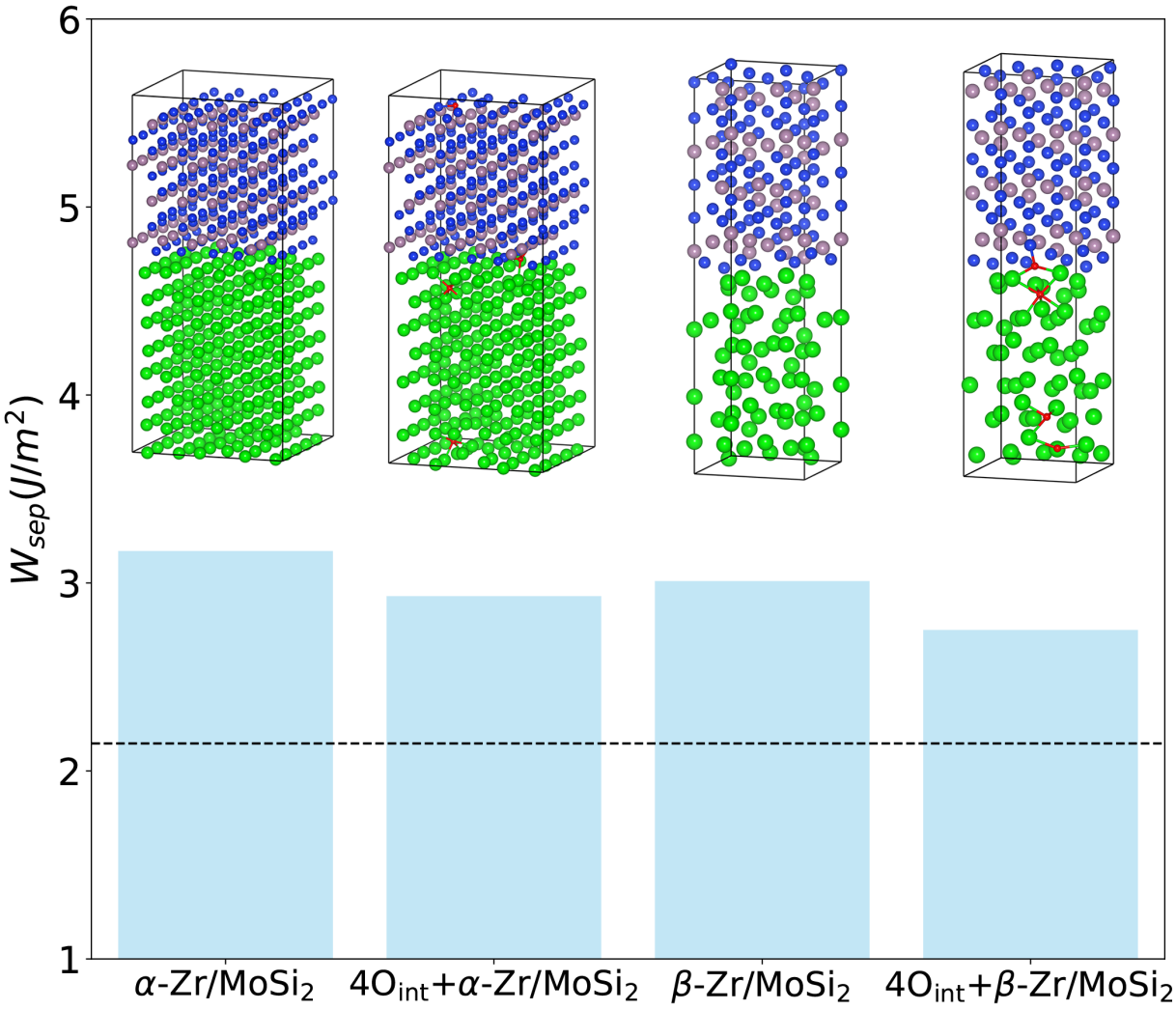

Figure 2.4: Work of separation (W_{sep}) of clean and O_{int}-contaminated Zr/MoSi2 interfaces. The black dashed line indicates the W_{sep} of the clean Σ5 (001) twist GB of $MoSi_2$ as a reference.

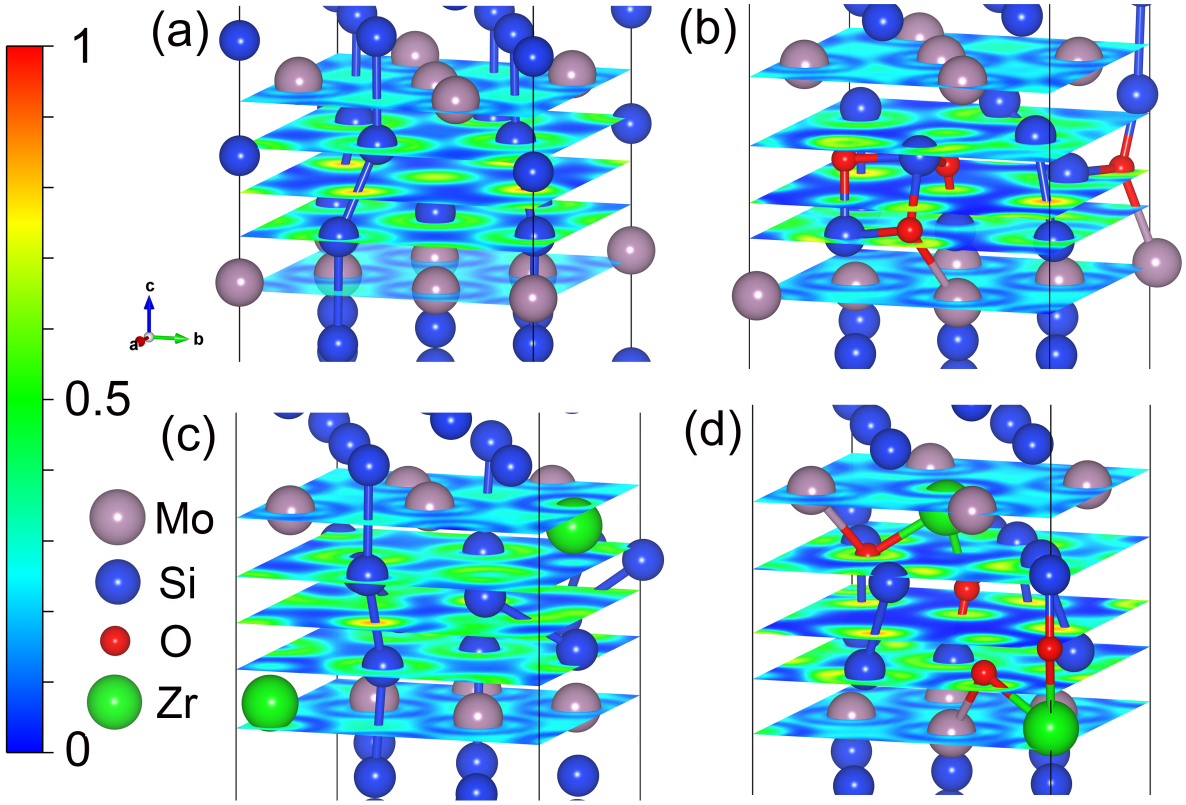

Figure 2.5: Electron localization function (ELF) distribution of (a) clean $MoSi_2$ grain boundary (GB), (b) $4O_{int}$ doped GB, (c) $2Zr_{Mo}$ doped GB and (d) $4O_{int}$ + $2Zr_{Mo}$ doped GB.

reveal how charges transfer between different elements upon the introduction of O_{int} and Zr_{Mo} dopants in $MoSi_2$ (see Figure 2.5). Bonding in $MoSi_2$ is known to have hybrid metallic and covalent character[26]. The ELF plots show that electrons in the $MoSi_2$ GB are highly localized (covalent-like) between out-of-plane Si-Si bonds at the clean GB (ELF: yellow). O_{int} introduced into the GB attracts electrons (due to the higher electronegativity of O), resulting in electrons being localized around the O atoms (ELF: orange to red) and a weakening of the covalent bonding between out-of-plane Si. We speculate that this effect causes a reduction in the strength (embrittlement) of the $MoSi_2$ GB. Conversely, the introduction of Zr_{Mo} replaces Mo with a more electropositive element Zr, which donates electrons to O_{int} and mitigates the embrittling effect of O_{int}. These qualitative observations are supported by Bader analysis (Tables A.2, A.3 , A.4, A.5, and Figure A.4, A.5, A.6, A.7), which show similar trends in charge transfer between dopants and $MoSi_2$.

2.4.2 Zr as a getter

Our calculations show that Zr has a far more substantial effect on the strength of $MoSi_2$ as a getter compared to as a dopant. We find a strong thermodynamic driving force for O_{int} to migrate from $MoSi_2$ to the Zr subsurface region of the Zr/$MoSi_2$ interface (Figure 2.3). Though the W_{sep} of the Zr/$MoSi_2$ interface is slightly reduced with Zr-subsurface O_{int}, it is still higher than that of the $MoSi_2$ GB. The subsurface nature of this getting effect of Zr implies that nanoparticles with high surface area to volume area would be most effective as getters. Indeed, these findings are consistent with previous experimental studies[60], which find that the addition of Zr promotes the formation of spherical nano-scale particles (ZrO_2, Mo_2Zr) that are mainly located at GBs as well as partially within the grains. These nanoparticles tend to pin the GBs, further enhancing the mechanical properties of the alloy[23].

2.4.3 Screening for getter materials

The effect of Zr as a getter for $MoSi_2$ is due to (i) its higher affinity for oxygen interstitials, and (ii) the interface formed by Zr and $MoSi_2$ having a higher W_{sep} and greater resistance to oxygen embrittlement than $MoSi_2$ alone. These insights provide us with the basis to formulate a strategy to computationally screen for other effective getters for $MoSi_2$.

It is clear that performing similarly detailed first principles studies on all possible getter elements would not be feasible, given the computationally- and human-intensive nature of such calculations. However, we can devise readily available proxy computational and experimental descriptors that would allow for an efficient screening:

- Oxygen exchange reaction energy. To estimate the relative oxygen affinity of an element A relative to Mo, we use the computed reaction energy for the following oxygen exchange reaction: MoO_3 + 3x/y A $\longrightarrow$ 3/y AxOy + Mo where AxOy is the most stable oxide (most negative formation energy) formed by the element A. These reaction energies are computed using pymatgen by querying for the pre-computed data from the Materials Project retrieved via the Materials API[47–49]. The oxygen exchange reaction energy is normalized per MoO_3 for comparison across all elements.

- Silicate formation energy. A secondary effect of the Zr getter is its ability to decrease glassy SiO_2 from the interface via formation of more stable and crystalline silicate $ZrSiO_4$ [15,38,61]. As a proxy for an element's bonding strength to Si and affinity for silicate formation, we use the lowest formation energy of the AxSiyOz silicate as follows: x A + y Si + z/2 O_2 $\longrightarrow$ AxSiyOz Again, AxSiyOz is chosen to be the most stable A-containing silicate in the Materials Project database. The silicate formation energy is normalized to a per atom basis for comparison across all elements.

- Melting point. The getter element should have a relatively high melting point given that the major application of $MoSi_2$ are in high-temperature applications.

Figure 2.6 plots the three proxy descriptors for 55 potential element getters in the periodic table. An ideal getter should be in the bottom left of the plot (region I, i.e., with a negative oxygen exchange reaction energy and a silicate formation energy lower than $ZrSiO_4$) with a high melting point. Elements in region II can still serve as oxygen getters, but silicate formation is less favorable than $ZrSiO_4$. An important validation of our proposed screening strategy is that experimentally well-established strengthening elements such as B, Al, Mg, Zr, Ti, V, Nb, Hf[20–28,30–32] mostly lie within regions I and II. Furthermore, the oxides La_2O_3, Y_2O_3, Sc_2O_3 and $MgAl_2O_4$[35–38] are also well-established getters, and all contain elements within regions I and II.

In addition to the known getters, other potential elements in region I are Sc, Y, La, Ce, Pr, Nd, Sm, Gd, Tb, Dy, Ho, Er, Tm, and Lu. Unfortunately, most of these candidates are rare-earth metals with significant supply risks and competing commercial applications. Nonetheless, the more abundant elements such as La and Ce are potentially interesting candidates for further experimental study.

For elements in region II, we will focus on elements with oxygen exchange reaction energies that are more negative, i.e., greater affinity for oxygen, than well-known getters such as Nb and V, which set the upper bound among the known getter materials. Elements in region II satisfying this criterion include Li, Be, Na, Ca, Sr, Ba, Eu, Yb. Among these, Li and Na have too low melting points to be of practical interest. The alkaline-earth metals Ca, Ba and Sr are potentially interesting, though all are relatively soft metals. Ba, in particular, is one of the most well-known getter materials used in vacuum tube applications[62]. Be is another interesting candidate that is expected to outperform Zr in terms of oxygen affinity, though with a slightly less negative silicate formation energy.

It should be noted that there are no silicates in the Materials Project database for the elements Ru, Ta, Re, Au, Ac, Ir, Os, Pt, and Rh, and hence, these are not plotted in Figure 2.6. Among these, Ta, Re, and Ac have negative oxygen exchange reaction energies, and therefore are potential oxygen getters. Indeed, Re is well-known ductilizer for Mo[19]. Ta is especially

interesting due to its relative abundance and refractory nature.

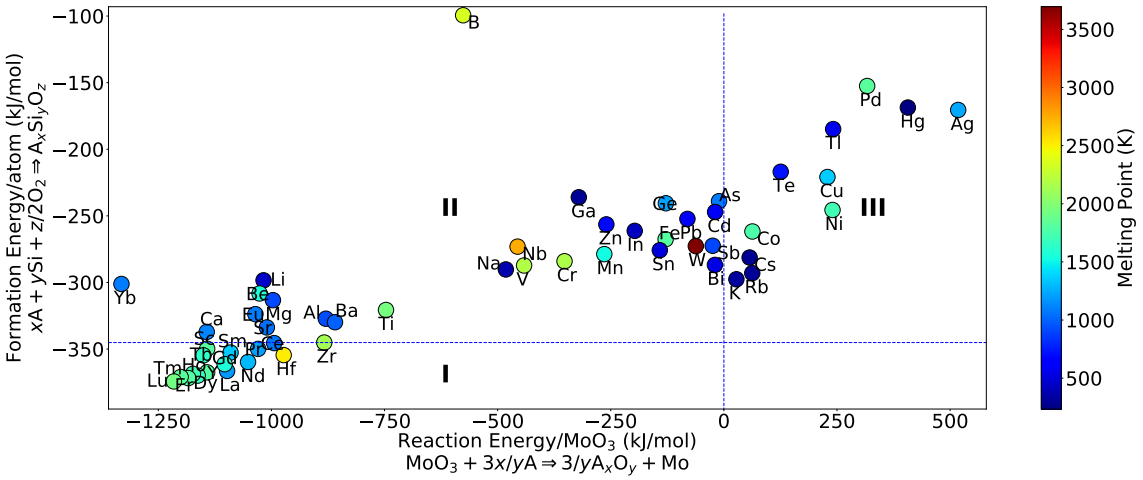

Figure 2.6: Plot of silicate formation energy versus oxygen exchange reaction energy for 55 elements in the periodic table. Marker colors represent the melting temperature of each element. A horizontal line is drawn passing through Zr. The regions are labelled as follows: I: oxygen exchange reaction favored and silicate formation energy is lower (more exothermic) than Zr; II: oxygen exchange reaction favored and silicate formation energy is higher (less exothermic) than Zr; III: oxygen exchange reaction not favored but silicate formation energy is negative.

While we have focused primarily on $MoSi_2$ in this work, the screening approach and descriptors outlined above can be readily adapted to other alloy systems. We note that proper conclusions about the effectiveness of a potential getter need to consider the relative W_{sep} of the oxygen-contaminated interface between the getter and the host, compared to the oxygen-contaminated host GB. Therefore, the above screening process should be considered only as an initial pre-screening for subsequent detailed investigations. Using the large quantity of pre-computed data in the Materials Project, a rapid screening can be conducted that would at least significantly narrow down the list of candidates that need to be considered for further first principles (e.g., the GB and interface studies in this work) and experimental studies.

2.5 Conclusion

To conclude, we have investigated two mechanisms for Zr incorporation into $MoSi_2$ – as a dopant and as a getter secondary phase using density functional theory calculations. We find that though Zr dopants mitigate the embrittling effect of oxygen interstitials in MoSi2 GBs, a far more significant effect is observed when Zr is present as a secondary phase. There is a strong thermodynamic driving force for oxygen interstitials to migrate to the Zr subsurface of the Zr/$MoSi_2$ interface, and the resulting interface has a higher work of separation than $MoSi_2$ GBs. Using simple thermodynamic descriptors, we have also identified other elements that may serve as possible getter materials for $MoSi_2$. These insights pave the way for rational design of $MoSi_2$ and other alloys for improved oxidation resistance.

Chapter 2, in full, is a reprint of the material "Role of Zr in strengthening $MoSi_2$ from density functional theory calculations" as it appears on Acta Materialia 2018, 145, 470–476. Hui Zheng Richard Tran, Xiang-Guo Li, Balachandran Radhakrishnan, Shyue Ping Ong. The dissertation author was the primary investigator and author of this paper.

Chapter 3

Grain boundary properties of elemental metals

3.1 Introduction

The majority of engineering materials are polycrystals, comprising a large number of grains whose interfaces form grain boundaries (GBs). The GB character distribution (GBCD)[63], i.e., the type and frequency of GBs present, strongly affects a material's mechanical properties[64,65] such as hardness[66], brittleness[67,68], creep-strength[69], corrosion resistance[70], fatigue strength[71], and weldability[72]. For instance, intergranular fracture is the primary origin of severe brittleness and fatigue failure, and GBs are the preferential sites for the nucleation and propagation of fatigue cracks[67,73]. Manipulating the GBCD through various processing techniques is a common pathway to improving the mechanical properties of structural metals and alloys.[65,67,71,74,75].

The GBCD of a material is related to the relative GB formation energies[76]. In thermodynamic equilibrium, the lower the formation energy for a particular type of GB (otherwise simply known as the GB energy or γ_{GB}), the greater its prevalence in the polycrystal[67,76,77]. A variety of experimental techniques (e.g., thermal groove, orientation imaging microscopy) have been applied to investigate γ_{GB} , but the data sets were limited due to the difficulty of measuring accurate γ_{GB}[78–84]. Recently Rohrer et al. have developed a high-throughput (HT) experimental method to measure γ_{GB} for large ensembles of GBs by inversely correlating it with the statistical abundance of GB types present in the polycrystal[76,85,86]. This method has been applied to fcc Ni[7], Ni-based alloys[76], W thin film[87], ferrite (mainly bcc Fe)[88], austenitic steel (mainly fcc Fe)[89] and hcp Ti[90]. Such HT studies have significantly increased the available experimental data for γ_{GB}[7,77]. However, this statistical approach suffers from a strong dependence of the uncertainty in the measured γ_{GB} on the frequency of observed GBs, leading to unreliable measurements for GBs of lower frequency. Furthermore, the method yields relative, rather than absolute, γ_{GB}.

Computationally, there have been many investigations of γ_{GB} using both empirical and first principles methods. Studies using empirical interatomic potentials (IAPs) such as the embedded atom method (EAM)[91–93] and Lennard-Jones[91,92] potentials are typically limited to

a few elemental systems belonging to a specific crystal prototype (e.g., fcc or bcc), but cover a broad range of GB types [1,2,94–97]. The reason is because the fitting of sufficiently accurate IAPs is a relatively complex and resource-intensive process, but once fitted, it is inexpensive to use the IAP to compute many GB structures comprising thousands or even millions of atoms. For instance, Olmsted et al. [1], Holm et al. [96,98] have calculated γ_{GB} for 388 distinct GBs of fcc Ni, Al, Au, and Cu using EAM and found that GB energies in different elements are strongly correlated. For bcc metals, Ratanaphan et al. [2] have computed the energies of 408 distinct GBs in bcc Fe and Mo ranging from $\Sigma 3$ to $\Sigma 323$. Their results show that GB energies are influenced more by GB plane orientation than by lattice misorientation or lattice coincidence.

With computing advances, calculations of γ_{GB} using accurate, but expensive first-principles methods such as density functional theory (DFT) have become increasingly common. In contrast to IAP-based studies, DFT studies tend to be broader in chemical scope but narrow in the range of GB structures studied (typically limited to low Σ GB models of hundreds of atoms). This is due to the universal applicability, but high computational expense, of DFT methods. For example, Scheiber et al. [99] have computed 14 types of GBs for W, Mo and Fe using DFT, while Wang et al. [100] have calculated 11 types of low sigma ($\Sigma < 13$) symmetrical tilt GBs and 2 twist GBs for bcc Fe. Bean and McKenna [101] have also used DFT calculations to verify a small subset of symmetric tilt GB structures acquired from EAM calculations in Cu and Ni systems.

In this work, we report the development of the Grain Boundary DataBase (GBDB), a comprehensive database for GB properties (γ_{GB}, work of separation W_{sep}) for a broad range of low-index GB structures (tilt and twist) for fcc, bcc, and hcp elemental metals using high-throughput DFT calculations. At the time of writing, this GBDB contains data on 327 GB structures for 58 elements, with more GB types and elements continually being added. This GBDB has been made available via the Materials Project and its Application Programming Interface [102,103], together with a user-friendly web application called Crystal Toolkit for the generation of GB structures. A critical enabler to the construction of the GBDB is an innovative lattice scaling approach,

which substantially lowers the computational effort in performing GB calculations for similar crystal types across different elements. Finally, we rigorously validate the GBDB against prior experimental and computed data, and using this large dataset, develop an efficient model for predicting γ_{GB} for different elements.

3.2 Methods

3.2.1 Grain boundary model generation

Figure 3.1 shows the schematic of the GB model generation algorithm, which is based on the coincident-site lattice (CSL) method[104]. For two grains misoriented by a rotation angle about a rotation axis, the superposition of the two crystals result in coincident sites forming a sublattice of the two crystal lattices, i.e., a CSL. An important parameter characterizing the CSL is the Σ value, defined as the ratio of the unit cell volume of the CSL to the volume of the generating bulk cell. A GB can be completely and unambiguously described by five macroscopic degrees of freedom (DOFs)[10], e.g. Σ5 36.87°[100](031). Three DOFs describe the mutual misorientations between two adjoining grains, two of which define the rotation axis (two DOFs, e.g. [100]) and one of which defines the rotation angle, e.g. 36.87 °. The remaining two DOFs describe the GB plane, e.g. (031). In addition to these five independent macroscopic DOFs, three microscopic DOFs characterise a rigid body translation of two grains relative to each other[10]. The steps in the algorithm are as follows: 1. Starting from the unit cell (primitive or conventional cell) with lattice type of cubic, tetragonal, orthorhombic, hexagonal or rhombohedral, a series of lattice vector transformations is performed to create an unit cell of CSL with the a and b lattice vectors parallel to the input GB plane. 2. Two grains are created and rotated relative to each other based on the inputs (rotation axis and angle, expansion times of the CSL unit cell along *c* direction). 3. The two grains are then stacked to form the periodic GB structure. The relative shifts between the two grains along the *a*, *b* and *c* directions can be adjusted. 4. Finally, sites that are too close to each

other based on a distance tolerance set by the user are merged.

The above algorithm is implemented in the open-source Python Materials Genomics (pymatgen) materials analysis library[102], together with methods for finding all sigma values and their corresponding rotation angles for any given input structure and rotation axis. A user-friendly graphical user interface to the algorithm is also available on Materials Project website Crystal Toolkit application (https://materialsproject.org/#apps/xtaltoolkit).

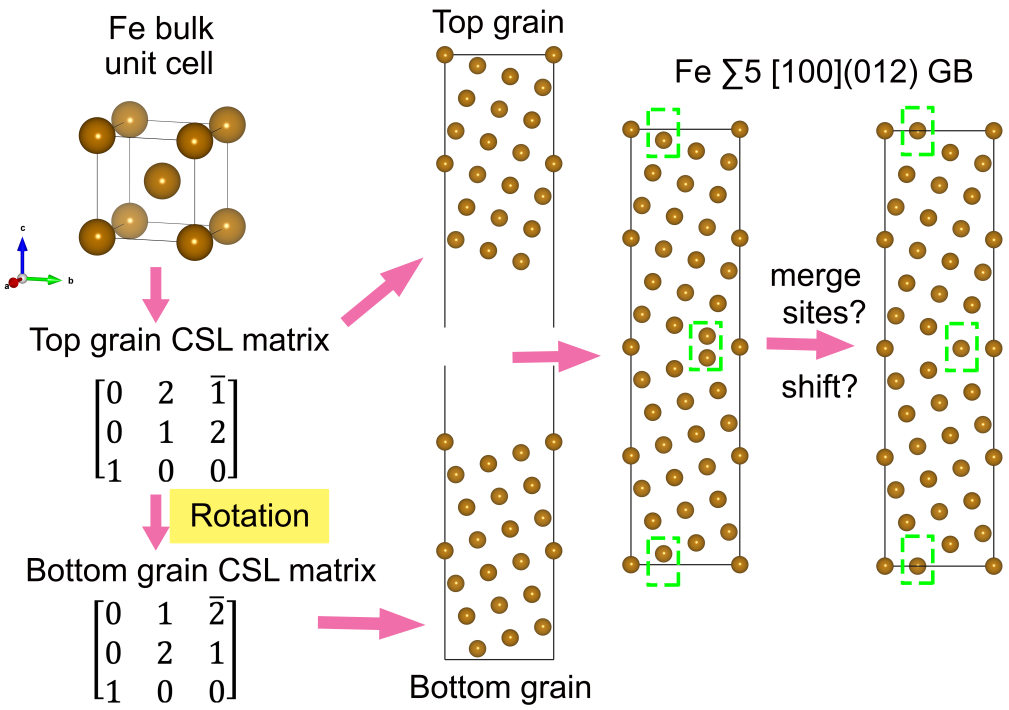

Figure 3.1: Grain boundary generation process

3.2.2 GB property computation

The GB energy (γ_{GB}) is defined by the following expression:

$$\gamma_{GB} = \frac{E_{GB} - n_{GB}E_{bulk}}{2A_{GB}} \tag{3.1}$$

where E_{GB} and n_{GB} are the total energy and number of atoms of the GB structure,

respectively, A_{GB} is the cross-sectional area of the GB, E_{bulk} is the energy per atom of the bulk, and the factor of 2 in the denominator accounts for the two grain boundaries in the GB model.

Another GB property of interest is the work of separation W_{sep}, which is a measure of the energy required to cleave the GB into the free surfaces and is correlated to the fracture toughness[105–108]. W_{sep} is given by the following expression:

$$W_{sep} = 2\gamma_{surf} - \gamma_{GB} \tag{3.2}$$

where γ_{surf} is the corresponding surface energy for the facet (hkl) formed by cleaving the GB. Previously, some of the current authors have already constructed a comprehensive database of the surface energies of the elements[109], which are used in this work in the computation of W_{sep}.

3.2.3 DFT computations

All DFT energy calculations were performed using the Vienna Ab initio Simulation Package (VASP)[14] with the projector augmented wave (PAW)[50,51] method. The exchange-correlation effects were modeled using the Perdew-Berke-Ernzerhof (PBE)[52] generalized gradient approximation (GGA) functional. The plane wave energy cutoff is 400 eV. The k-point grid for structure relaxation is 30 per Å^{-1} in a and b directions (GB plane), and a denser grid of 45 per Å^{-1} is applied for single-point energy calculations. The energies and atomic forces of all calculations were converged within 10^{-4} eV and 0.02 eV Å^{-1} (see Table S1 for force convergence tests on Mo). Through a series of convergence tests (see Fig B.3), it was determined that a minimum normal distance of ~ 25 Å between periodic boundaries ($2 \times$ the distance between GBs) is sufficient to minimize interactions between the two grain boundaries, such that γ_{GB} is converged to within 0.05 J m^{-2}. It should be noted that this 25Å refers to the minimum distance, and the average distance between periodic boundaries is ~ 40 Å (see Fig B.4).

3.2.4 Scope and Availability of Data

Our database covers a total of 58 elements (see Figure 3.2), with 10 GB types for fcc and bcc and one GB type for hcp and double-hcp (dhcp) elements (see Table 3.1), with a total of 327 GB structures. We limit the GB types in this study with the following criteria:

1. $\Sigma < 10$
2. Maximum Miller index (MMI) of rotation axis ≤ 1
3. MMI of GB plane ≤ 3.
4. All tilt GBs are symmetric.

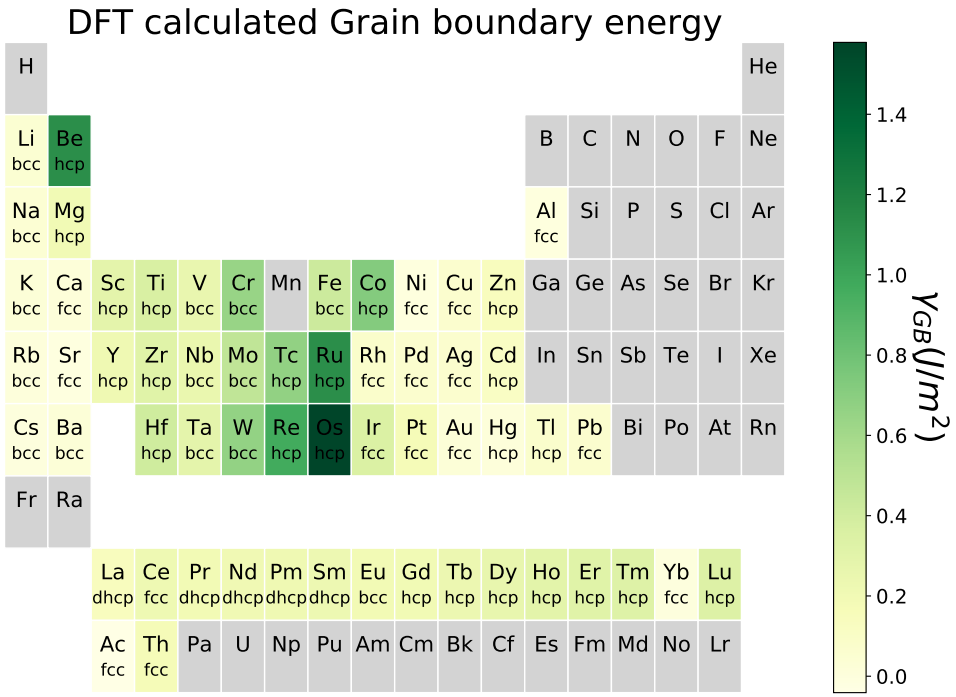

Figure 3.2: DFT calculated GB energy. For bcc and fcc, the lowest γ_{GB} types, i.e., $\Sigma 3[110](112)$ for bcc and $\Sigma 3[111](111)$ for fcc are plotted. For hcp, and double-hcp (dhcp) elements, $\Sigma 7(0001)$ GBs are chosen to be represented in this periodic table heatmap.

Table 3.1: GB types calculated in this work. Note: The $\Sigma 7[111](111)$ twist GBs of bcc Li, Na, K, Rb, Cs and Ba have 336 atoms instead of 168.

Sigma	type	R-axis	R-angle	GB-plane	Join-plane	No. of atoms	
						bcc	fcc
3	tilt	[110]	109.47	(1 $\bar{1}$ $\bar{2}$)	($\bar{1}$ 1 $\bar{2}$)	24	46
3	tilt	[111]	180	(1 $\bar{1}$ 0)	(0 1 $\bar{1}$)	48	56
3	twist	[111]	60	(1 1 1)	(1 1 1)	48	24
5	tilt	[100]	36.87	(0 $\bar{1}$ $\bar{2}$)	(0 2 1)	38	38
5	tilt	[100]	53.13	(0 $\bar{1}$ $\bar{3}$)	(0 3 1)	40	58
5	twist	[100]	36.87	(1 0 0)	(1 0 0)	80	80
7	twist	[111]	38.21	(1 1 1)	(1 1 1)	168*	84
7	tilt	[111]	38.21	(1 $\bar{3}$ 2)	($\bar{2}$ 3 $\bar{1}$)	54	54
9	twist	[110]	38.94	(1 1 0)	(1 1 0)	126	180
9	tilt	[110]	38.94	(2 $\bar{2}$ $\bar{1}$)	(2 $\bar{2}$ 1)	70	70
						hcp/dhcp	
7	twist	[0001]	21.79	(0 0 0 1)	(0 0 0 1)	112	

All GB structures and properties are available on the Materials Project (`https://materialsproject.org/`)[102,103] and Crystalium (`http://crystalium.materialsvirtuallab.org`)[109] websites. A visual inspection of all 327 GB structures revealed no abnormal structures.

3.3 Results

3.3.1 Benchmarking

A major bottleneck to calculations of GBs is that the large system sizes combined with difficult convergence of atomic positions, especially close to the GB region, render such com-

putations relatively expensive compared to bulk crystal calculations. Furthermore, in order to obtain the global minimum configuration, it is necessary to perform a complete grid search over translations of the grains in all three crystallographic directions. However, such an effort would be prohibitively expensive for a high-throughput database construction. To accelerate such computations, we designed a scheme to find reasonable low-energy (not necessarily the global lowest) GB configurations. A fundamental hypothesis explored in this work is that similar crystal structures (e.g., bcc, fcc, or hcp) tend to lead to similar low-energy GB configurations, and an efficient step-wise translation search scheme was used as opposed to a full grid search to identify low-energy GB configurations.

The efficient search scheme proceeds by applying rigid body translation[97] of two grains to each type GBs and performing a static calculation for each translation vector. The search was performed in two steps. First, a search was performed for the optimal inter-grain separation by translating the two grains along the $\boldsymbol{c}$ direction in increments of 10% of the lattice parameter of the conventional unit cell. In the second step, a grid search for the optimal $\boldsymbol{a}$ and $\boldsymbol{b}$ translations in increments of 5% - 12.5% of the basal lattice vectors ($\boldsymbol{a}$ and $\boldsymbol{b}$) was performed using the optimal $\boldsymbol{c}$ translation from the first step. The results (see Figures B.1 and B.2) show that basal plane translations contribute to an energy difference of < 0.05 J m^{-2} for most GBs of Mo and Nb, with the largest energy difference of 0.125 J m^{-2} for $\Sigma 5(013)$ twist GB of Mo (see Tables B.2). As such, for the purposes of the high-throughput GB data generation, the GBs were generated with no basal plane translations. We also note that a full grid search in all three crystallographic directions using 12 GBs of Nb and Mo reached similar conclusions, justifying the use of the step-wise search (see Table B.3). For symmetric tilt GBs, atoms at the interface that are less than 70% of the bulk interatomic distance apart are merged.

Based on these results, we have developed a high-throughput workflow for GB calculations using the Atomate software package[102,110,111], as shown in Figure 3.3. For each structural prototype (bcc, fcc, hcp and dhcp), we first compute a series of fully-relaxed GB templates

for all the GB types investigated in this work (see Table 3.1), using Mo, Cu and Be/La as the templates for bcc, fcc and hcp/dhcp structures, respectively. Initial structures for GB computations of each element M are then created from these GB templates by applying a scaling factor of $\frac{a_M}{a_{prototype}}$ to the template GB lattice constants for all materials, where a_M and $a_{prototype}$ are the bulk lattice parameters of the metal M and prototype element respectively. No scaling is applied for Zn and Cd, which are hcp elements with anomalous c/a ratios (1.986 and 1.915, respectively, from our PBE calculations, which is consistent with previous DFT studies[112]) that deviate substantially from the ideal ratio of 1.633, and their GB structures were generated directly from the bulk structure. A full relaxation is then performed on the scaled GBs. The use of the scaled GB templates significantly reduces the computational resources for the most time-consuming structural relaxation step by a factor of $\sim 3-6$, with higher speed-ups for GBs with larger number of atoms and GBs that are very different from bulk (Table 3.2). More accurate static calculations with denser *k*-point meshes were then performed to obtain the final total energy of the GB structures. The results were then automatically inserted into a MongoDB document-based database.

We believe our step-wise search scheme combined with the GB template strategy provides a highly efficient approach to generating low-energy GB configurations with energies that are reasonably close to the global minimum. Furthermore, the database can be readily updated to incorporate new lower energy GB configurations as they are reported.

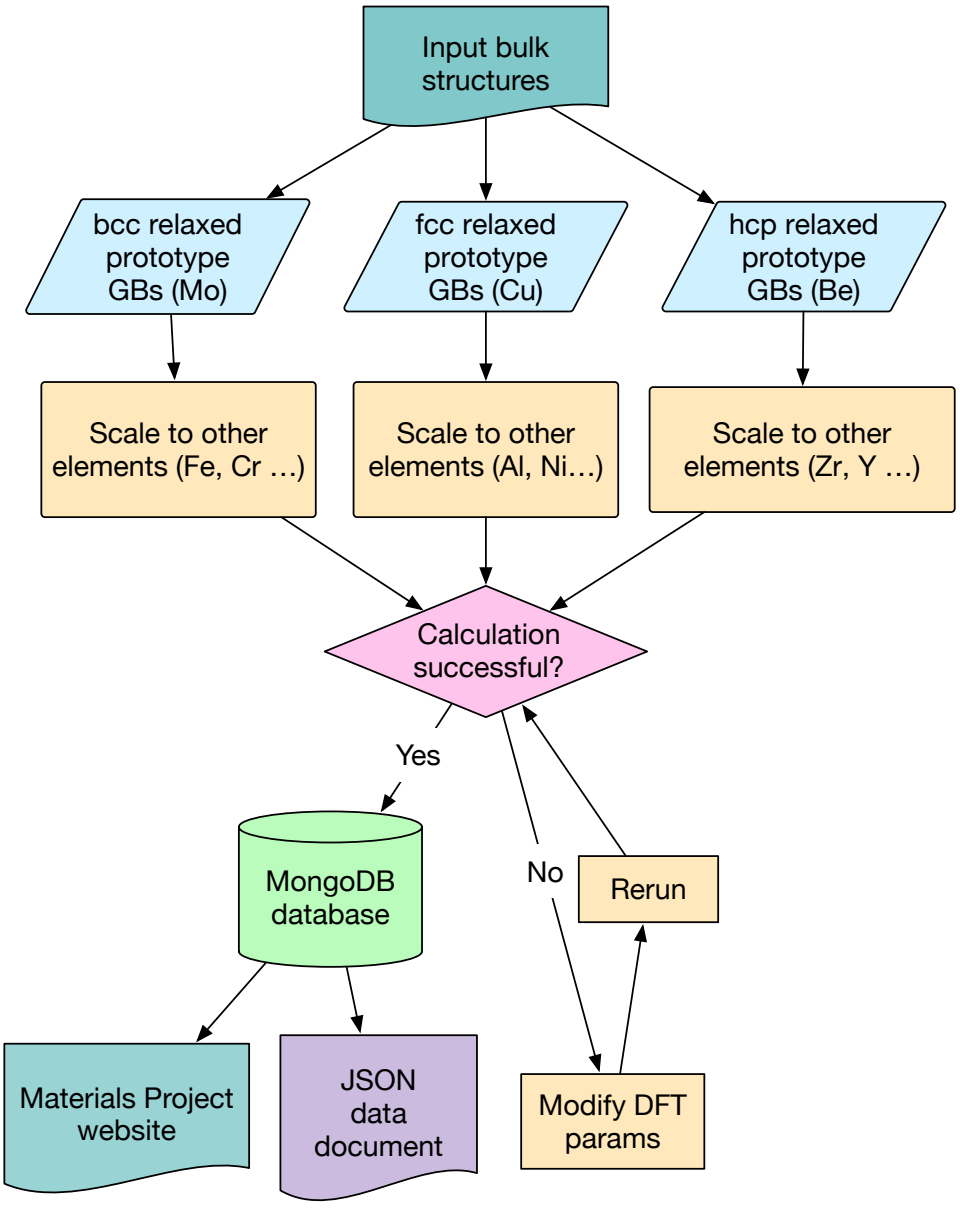

Figure 3.3: High-throughput computational workflow for elemental grain boundaries.

Table 3.2: CPU hours for GB relaxation with and without the use of scaled prototype templates.

			CPU hours		
Element	GB type	# of atoms	No template	With template	Speed up
bcc-Ba	Σ3(111)	48	2560.00	716.80	3.57
bcc-Fe	Σ9(110)	126	2340.00	508.33	4.60
fcc-Sr	Σ5(100)	80	2128.05	344.29	6.18
fcc-Ag	Σ5(013)	80	97.67	97.55	1.00
hcp-Ti	Σ7(0001)	112	24.28	13.94	1.74
dhcp-Nd	Σ7(0001)	112	218.39	59.08	3.70

3.3.2 Grain boundary energies

Figure 3.4 shows the distribution of γ_{GB} for bcc, fcc, and hcp elements. All values are tabulated in Table B.4 and B.5 for reference. For bcc elements (Figure 3.4a), we can observe a substantial jump in γ_{GB} from alkali/alkaline earth metals to transition metals; the γ_{GB} for alkali and alkaline earth metals are less than 0.3 Jm^{-2}, while those for the transition metals are at least four times higher. γ_{GB} for fcc elements follows a similar trend but with a more gradual increase (see Figure 3.4b). Group VIII elements have high γ_{GB} while group IB, IIA, and IIB elements have relatively low γ_{GB}. Figure 3.4c shows the γ_{GB} distribution for hcp/dhcp Σ7(0001) grain boundaries. For transition metals, we observe that γ_{GB} peaks at groups VIIB and VIII (Tc, Co, Re, Ru, and Os). All the rare earth and group IIA elements have lower GB energies than the transition metals with the exception of Be, which has a much higher GB energy. The rare earth elements show a gradual increase in γ_{GB} as group number increases.

The γ_{GB} distribution across different GB types varies with the crystal type. The two coherent twin boundaries, Σ3(111) for fcc and Σ3(112) for bcc, have the lowest γ_{GB} within the respective crystal prototypes. GBs terminated by the most atomically-dense planes ((111) for fcc

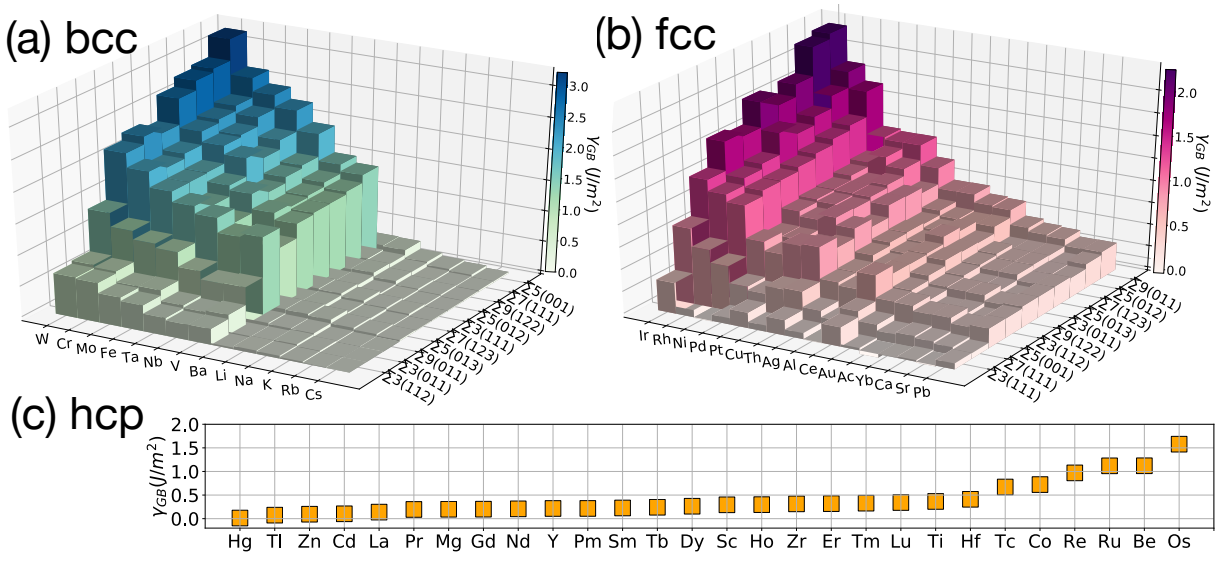

Figure 3.4: GB energy γ_{GB} distribution for (a) bcc, (b) fcc, and (c) hcp/dhcp elemental metals, sorted by increasing γ_{GB}.

and (110) for bcc) have lower γ_{GB} than other planes in general. Consequently, the fcc Σ 7 (111) and bcc Σ3(011) GBs correspond to the second lowest γ_{GB} for fcc and bcc, respectively. This is in agreement with both previous atomistic calculations[2,92,93,96,113] and experimental results[6,77,87,98]. For example, it has been observed experimentally that the most frequently observed GB for fcc Ni and Al is the Σ3(111) twin boundary, and other GBs terminated with the (111) plane also have a high population[6,7]. For bcc metals, our data shows that the Σ3(112) symmetric tilt GB (twin) has the lowest energy, which agrees with experiments performed in bcc W thin films[87] with nanoscale grain sizes and bcc ferritic/interstitial free steel[5,88]. It should be noted that a few GBs have unphysical negative γ_{GB} values that are very close to zero ($< 0.02\ Jm^{-2}$). These can be attributed to small numerical convergence errors. Most of these GBs are coherent twin boundaries of fcc Sr, Ni, and Al, which are well-known to have extremely small GB energies.[7]

Figure 3.5 shows the validation of our computed γ_{GB} with previous DFT calculations[99,100 101,114–149], atomistic calculations[150] using machine-learned spectral neighbor analysis potentials (SNAP)[3,4] and the embedded atom method (EAM)[1,2,98], and experimental data[5,7,77,87]. From Figure 3.5a and Table B.8, we may observe that the most frequently studied systems are Fe[151–153]

[99,100,114–118,132–135,142,154,155], Al [120–125], Cu [101,127–131,156–158], Mo [99,119,136–138,159], W [147] [99,119,146,148,159,160] and Ni [101,118,132,137,139–141,143,144] due to their important applications in steel, automobile, and aerospace industries. The high computational cost of DFT methods and the lack of efficient GB generation tool limit the previous studies to mostly low sigma symmetric tilt GBs, such as $\Sigma5[100](012)$ [100,101,115,120–129,132,137,139–141,143,144,148], $\Sigma5[100](013)$ [116–119,135–137,142,156] [99,100,127,130,131,138,148], $\Sigma3[110](111)$ [99–101,114–116,126,132–134,139,145,147,148], $\Sigma3[110](112)$ [116,120,146] [99–101,117,127,135,147,148], etc. Our GBDB includes both these popular GB types and some other twist GB types for 58 elemental systems. When comparing to these GB data available in previous DFT work, our computed γ_{GB} have an excellent agreement, with a R^2 close to unity and a very small standard error of 0.013 J/m^2.

Similarly, we find good agreement between the calculated γ_{GB} for different GBs of Mo and Ni with those computed using the state-of-the-art SNAP models [3,4], while the EAM predicted GB energies [1,2] are substantially underestimated as shown in Figure 3.5(b) and (c). For bcc Mo, values of γ_{GB} using SNAP are slightly larger than most DFT values with the exception of the $\Sigma5(012)$ GB where SNAP slightly underestimates DFT values. For fcc Ni, the γ_{GB} values of both EAM and SNAP are consistent with our DFT values, further supporting the conclusion that EAM performs better in fcc systems than bcc systems. [4]

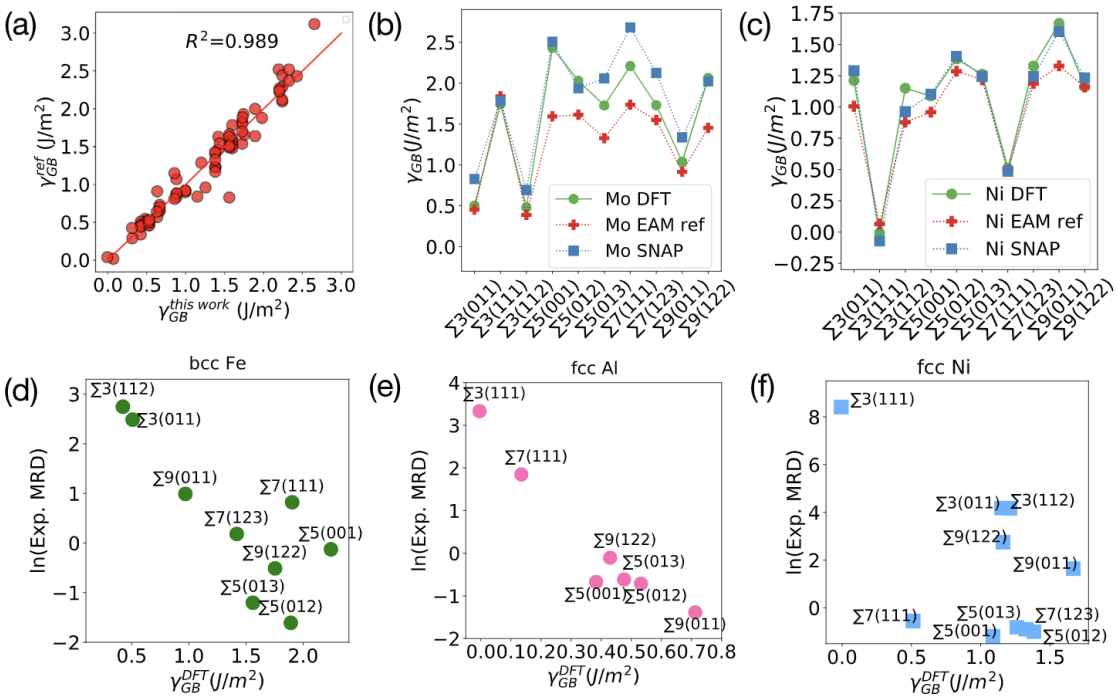

Figure 3.5: Comparison of γ_{GB} between this work and (a) previous DFT values; (b, c) EAM[1,2] and SNAP[3,4] values. (d), (e) and (f) compare our the calculated γ_{GB} of bcc Fe, fcc Al, and fcc Ni with experimentally measured MRD[5–7].

Figures 3.5(d) and (e) plot the natural log of the experimentally measured multiples of random distribution (MRD), i.e. the experimental average population of GBs, against the DFT calculated GB energy (γ_{GB}^{DFT}) for Fe and Al, respectively. We observe a negative correlation between the $\ln(MRD)$ and γ_{GB} similar to that reported previously for Ni[7]. Figure 3.5 (f) plots the experimental GB energy (γ_{GB}^{exp})[7] against our γ_{GB}^{DFT} values for Ni. All values of γ_{GB}^{exp} are derived from a statistical average of the MRD and given in arbitrary units. We also observe a general positive correlation between γ_{GB}^{exp} and γ_{GB}^{DFT}.

3.3.3 Work of separation

The thermodynamic threshold energy for GB fracture, or work of separation (W_{sep}), can be defined as the difference between the surface energy and GB energy as shown in equation (3.2) . Since the formation of surfaces and GBs both relate to bond breaking and distortion, we expect

GB energy γ_{GB}, surface energy γ_{surf} and work of separation W_{sep} to be positively correlated with cohesive energy. This is demonstrated in Figure 3.6 for bcc Σ3(110), fcc Σ3(111) and hcp Σ7(0001) GBs. The values of W_{sep} for all other GB types are provided in Table B.6 and B.7. This positive correlation is in agreement with previous bond breaking arguments[94,95]. The variation trend of W_{sep} is mainly dominated by γ_{surf} due to the small value of γ_{GB}. In general, the variation in anisotropic surface energies across different surfaces is smaller compared to the GB energy variation across different types of GBs as shown in Figure B.5. As such, we can expect a negative correlation between GB energy and work of separation as shown in Figure B.6 and B.7.

Figure 3.7 plots the experimentally measured ultimate tensile strength (UTS)[8] against the calculated W_{sep} for the GB with lowest γ_{GB}, i.e., the likely dominant GB type. A general positive relationship is observed between W_{sep} and UTS, as expected. The non-monotonic relationship may be due to the different processing methods (e.g., annealing, heat treatment, cold-worked) that can significantly affect micro-structure, and hence measured UTS.

3.3.4 Multiple linear regression model for γ_{GB}

Using the extensive set of computed γ_{GB}, we have developed a multiple linear regression (MLR) model for γ_{GB} for each GB type by fitting to the following equation:

$$\widehat{\gamma_{GB}} = \beta_1 E_{coh} a_0^{-2} + \beta_2 G \cdot a_0 \tag{3.3}$$

where $\widehat{\gamma_{GB}}$ is the fitted GB energy, E_{coh} is the cohesive energy, a_0 is the lattice parameter of corresponding conventional bulk cell (Å), and G is the Voigt-Reuss-Hill shear modulus (Jm^{-3})[161,162]. This model choice is an amalgamation of models proposed in previous works. Ratanaphan et al. have found that the γ_{GB} of bcc Fe and Mo are strongly correlated with the cohesive energy $(E_{coh})^2$. Previous EAM-based GB databases have also found that γ_{GB} for fcc metals such as Al, Au, Cu and Ni are strongly correlated to the the c_{44} elastic constant[1,96].

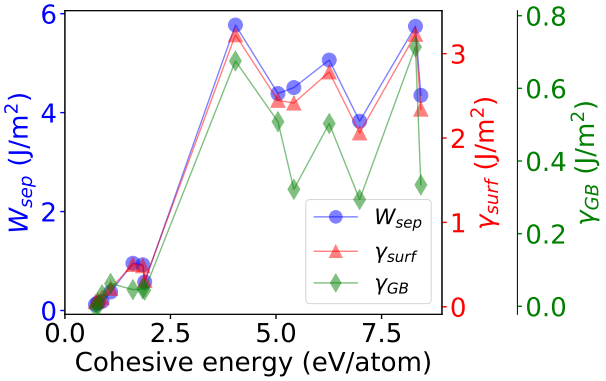

(a) bcc Σ3(110)

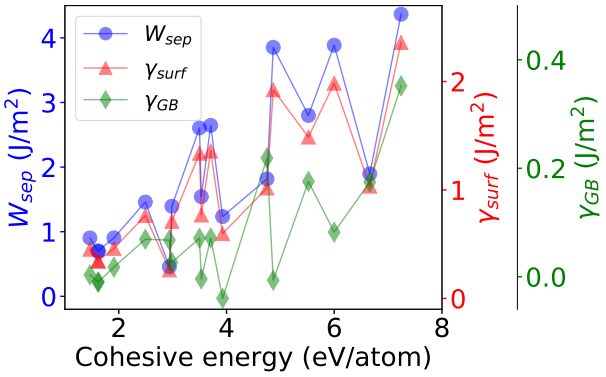

(b) fcc Σ3(111)

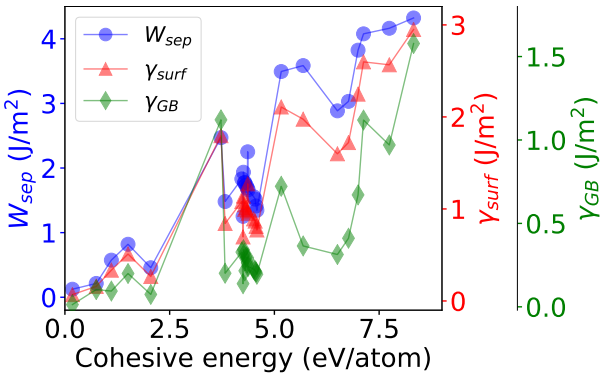

(c) hcp Σ7(0001)

Figure 3.6: Comparison between surface energy (γ_{surf}), GB energy (γ_{GB}) and work of separation (W_{sep}) for (a) bcc Σ3(110), (b) fcc Σ3(111) and (c) hcp Σ7(0001) GBs, plotted in order of ascending cohesive energy E_{coh} of the element. While all three quantities show a general positive trend with the cohesive energy, the range of W_{sep} is much larger than γ_{surf}, which are in turn much larger than γ_{GB}.

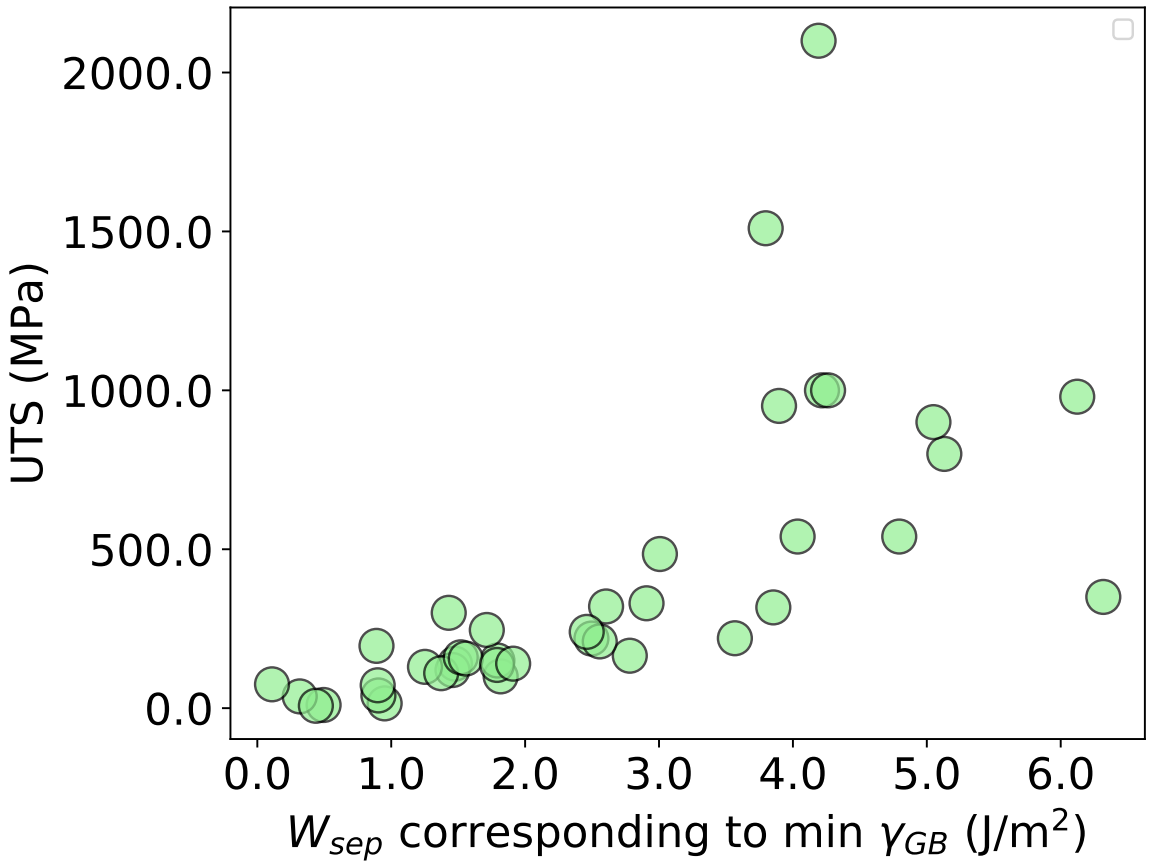

Figure 3.7: Relationship between calculated work of separation W_{sep} for GB with lowest γ_{GB} and experimentally measured ultimate tensile strength (UTS)[8].

Furthermore, the Read-Shockley dislocation model[163] treats GBs with small misorientation angles as an array of dislocations whose energy is proportional to a shear modulus. In essence, the $E_{coh}a_0^{-2}$ term in equation (3.3) accounts for the contribution of broken bonds to γ_{GB}, while the $G \cdot a_0$ term accounts for the contributions from distorted (stretched, compressed) bonds. Both terms have been scaled by powers of the lattice constant such that the coefficients β_1 and β_2 are dimensionless.

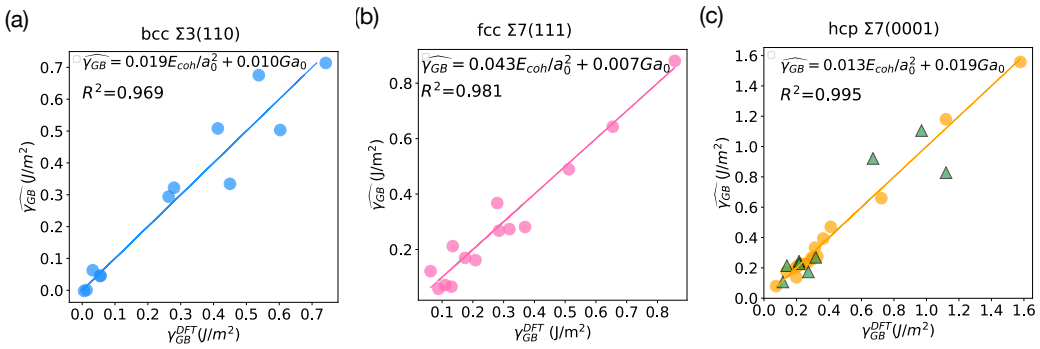

Figure 3.8: Multiple linear regression models for the (a) bcc $\Sigma3(110)$, (b) fcc $\Sigma7(111)$, and (c) hcp $\Sigma7(0001)$ GBs.

Figure 3.8 shows the fitting results for three GB types (see Figure B.8 and B.9 for the remaining GB types). In general, the MLR models exhibit good predictive accuracy across all GB types, with $R^2 > 0.9$. We note that each GB type has different fitted values of the dimensionless coefficients β_1 and β_2 due to different contributions from bond breaking and bond distortion. We provide an example to show the predictive ability of our linear regression model. In Figure 3.8(c), the orange circles are the data points used to build the MLR model, and the green triangles are a "test set" of elemental GBs. It can be seen that the performance on the "test set" is similar to that of the training set. We show that these results hold for all the GB structures computed in this work, and we believe it will hold for GB structures of larger Σ values for which the model GB structure can contain many more atoms and hence are more expensive to compute. The implication of these results is that a predictive MLR model can potentially be constructed using a smaller set of elements with a range of E_{coh} and G, and use to extrapolate to other elements.

3.4 Conclusion

The GBDB is, to the best of our knowledge, the most comprehensive database of DFT computed GB energies and work of separation to date, spanning 10 different of GB types, including both tilt and twist GBs, across 58 types of metals. This GBDB has been rigorously validated with previous computational values as well as experimental observations of the GBCD[2,5,6,64,76,77,87]. The linear regression model provides an inexpensive estimate for the GB energy of elemental metals using cohesive energy and shear modulus.

Chapter 3, in full, is a reprint of the material "Grain boundary properties of elemental metals" as it appears on Acta Materialia 2020, 186, 40–49. Hui Zheng Xiang-Guo Li, Richard Tran, Chi Chen, Matthew Horton, Donald Winston, Kristin Aslaug Persson, Shyue Ping Ong. The dissertation author was the primary investigator and author of this paper.

Chapter 4

Predictive processing of NbMoTaW multi-principal element alloy to tune short-range order and mechanical properties

4.1 Introduction

Multi-principal element alloys (MPEAs) are solid solutions composed of equiatomic multi-principal elements that are in contrast to the conventional alloys based on one principal element[13,164,165]. These compositionally complex alloys have excellent mechanical properties, e.g., high strength, ductility, and exceptional fracture toughness[166–169]. The high strength of MPEAs can be attributed to the dislocation motion being hindered by different defects, such as vacancies, stacking faults, twins, grain boundaries, etc. Specifically, for MPEAs, concentrated solutions also act as obstacles to dislocation motion. The ductility in MPEAs is explained by dislocation pile-up stress relief due to certain twin boundaries allowing partial dislocations to glide along their interfaces[12].

Initially, the research on MPEAs was focused on the random solid solution (RSS)[13]. More recently, researchers have also shown interest in local chemical short-range order (SRO)[170–177]. Both experimental and computational results have shown the existence of SROs due to the effect of enthalpic interactions at low temperatures.[170,172,178,179]

The metastable nature of MPEAs renders them with a large range of SROs, from RSS to fully ordered ground-state intermetallics[170,176,179,180]. However, it is debatable how the composition fluctuations or elemental distribution, such as short/long chemical orders[180,181], affect the deformation mechanism and mechanical properties. In the fcc NiCoCr ternary MPEA system, it is under contentious debate whether SRO has a significant impact on strengthening mechanical properties.[175–177,182,183]. Computationally, Ding et al. revealed a positive correlation between SFEs and SROs in NiCoCr MPEA using first-principles calculations.[175] Later on, Zhang et al.[177] verified computational findings by using energy-filtered transmission electron microscopy. They observed that the increasing amounts of chemical order give rise to both higher SFE and hardness. While almost at the same time, Yin et al.[183] reported that SRO has a negligible influence on alloy strength and hardness for samples annealed at 600 and 700 °C (i.e.,873 and

973K). Despite the disagreement on the effects of SRO, they propose that SRO likely develops during the slow furnace cooling in the regime of T $<$ 600 °C. Here, the key factor is that the annealing temperature must be low enough to enable the SRO formation. This finding provides a promising future for tailoring the SRO by low-temperature annealing.

In the bcc refractory MPEA systems, a few works[170,176,179,180,184] have explored the effects of chemical order on mechanical properties. Due to the presence of multi-principal elements, computational works often require relatively large supercells, which are computational expensive using first-principles calculations. The current authors have previously developed spectral neighbor analysis potential (SNAP) for the quaternary NbMoTaW system[176]. The SNAP model has great accuracy and transferability compared to classical force field models[185].

With newly developed SNAP, we demonstrate that chemical SRO can be tailored by changing the annealing temperatures (T_a) as revealed by Monte Carlo (MC)/molecular dynamic (MD) simulations. By annealing the bcc MPEA at temperatures from 300 K to 2400 K, different chemical SROs are attained. The statistical distributions of SFE, APBE, and CRSS of screw dislocation motion show that higher SRO leads to higher SFE, APBE, and CRSS. In tensile/compressive tests at room temperature, the samples with higher SRO correspond to higher ultimate tensile/compressive strength and better ductility/malleability. Usually, a decrease in temperature will cause decreased ductility, while the MPEA behaves differently. Ductility first decreases from 2400 K to 1500 K and then increases from 1500 K to 300 K. The existence of SRO increases the ductility/malleability of MPEA at low temperatures. These phenomena provide a promising tool to tailor the properties of MPEA through the selection of annealing temperature.

4.2 Methods

All the atomistic simulations using SNAP model[176] were performed using the LAMMPS code[186]. Hybrid MC/MD simulations under isothermal-isobaric (npt) ensemble were carried out

to obtain the equilibrium configurations at different annealing temperatures T_a. The initial MPEA bulk structure of NbMoTaW has random elements distribution. The structure consists of N = 3456 atoms with x, y, and z along [100], [010], and [001] crystal directions, respectively. The dimensions of the simulation box are about 39 Å$\times$ 39 Å$\times$ 39 Å. Periodic boundary conditions were applied in all directions. The MD time step was set to 2 fs. A Nose-Hoover thermostat was used to control the temperature. For every one MD step, there is one MC cycle. A total of 1,000,000 steps were carried out for each T_a to achieve converged SRO. The converged configurations were then quenched to 300 K, and energy was minimized at 0 K for subsequent property calculations. e.g., SFE, APBE.

4.2.1 Chemical SRO parameters

The pairwise SRO parameter[173,176] is defined as below:

$$\alpha_{ij}^{k} = (p_{ij}^{k} - c_j)/(\delta_{ij} - c_j) \tag{4.1}$$

where α_{ij}^{k} quantifies the chemical order around a central atomic species i with other species j within the k-th nearest-neighbor shells, p_{ij}^{k} denotes the average probability of finding a j-type atom around an i-type atom in the k-th shell, c_j is the average concentration of j-type atom in the system and δ_{ij} is the Kronecker delta function. For pairs of the same species (i.e., $i = j$), a positive α_{ij}^{k} means the tendency of attraction and a negative value suggests the tendency of repulsion in the k-th shell. For pairs of different elements (i.e., $i \neq j$), the interaction tendency is the opposite. i.e., a negative α_{ij}^{k} reflects the tendency of attraction between i-type atoms and j-type atoms within the k-th shell, while positive α_{ij}^{k} means repulsive preference between i-type atoms and j-type atoms.

4.3 Results

4.3.1 The effect of annealing temperature on SRO

The initial RSS structure is annealed at different temperatures (T_a) using hybrid MC/MD simulation until equilibrium is reached. We calculated the pairwise multi-component SRO parameters of the corresponding equilibrium configurations as shown in Fig. 4.1(a). The absolute values of SROs are the highest when annealing temperature is 300 K. With increasing annealing temperature, the absolute values of SROs of different element pairs first decrease dramatically from 300 K to 800 K, then decrease gradually from 800 K to 2400 K until converging to approximate zero. Three equilibrium atomic structures from annealing temperatures of 300, 600, and 1200 K are selected to represent the configurations of different SROs in Fig. 4.1(b), (c), and (d). The elements that belong to the same group are colored with similar color (Red and orange for Nb and Ta, respectively; light blue and blue for Mo and W, respectively). In Fig. 4.1(b), we can observe the alternating layers of warm colors (red and orange) (Nb, Ta) and cool colors (light blue and blue) (Mo, W) atoms along [001], [100], and [010] directions. The alternation of chemical occupancy is similar to a pseudo-binary cesium-chloride structure (Strukturbericht B2, Pearson type cP2), i.e., one class of atoms (group 5 elements Nb, Ta) prefers to occupy cube vertices, and another class of atoms (group 6 elements Mo, W) prefers cube centers. This indicates the large magnitudes of first nearest neighbor (1NN) SRO of repulsive pairs within the same element group (W-Mo and Nb-Ta), and attractive pairs within different element group (Nb-W, Nb-Mo, W-Ta, and Ta-Mo) as quantitatively shown in 4.1(a). This observation matches with the bonding preference reported by Widom et al. [170]

The SRO parameters of different element pairs in the second nearest neighbor shell (2NN) show similar magnitudes but opposite signs compared to 1NN SRO parameters. i.e., elements from the same group tend to be attractive while elements from different groups tend to be repulsive in 2NN shell. This is also reflected in Fig. 4.1(b). 2NN interactions correspond to the

atoms within each atomic layer along [001] direction where atoms are composed of similar color (elements within the same group). Compared to the structure annealed from 300 K, the structure annealed from 600 K starts presenting chemical disorder while still retaining some chemical order as shown Fig. 4.1(c). The structure annealed from 1200 K shows great chemical disorder as shown in Fig. 4.1(d).

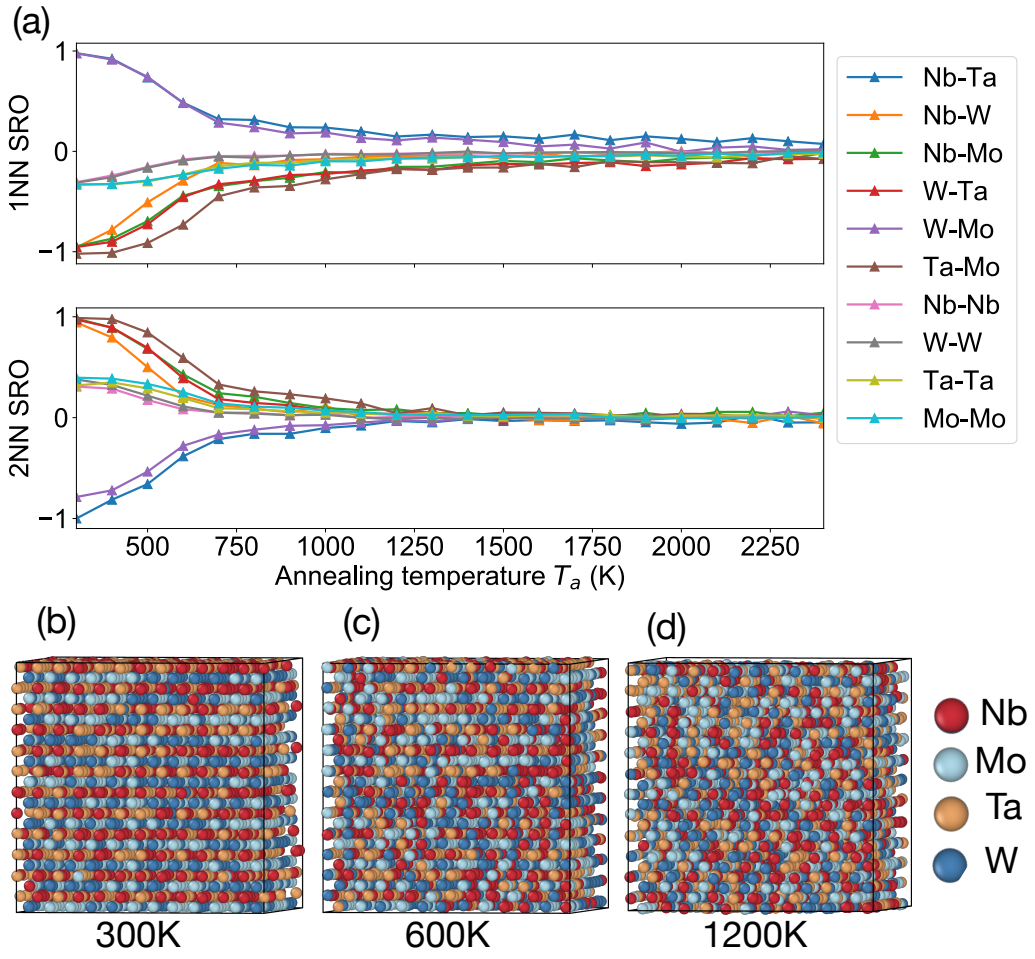

Figure 4.1: Short-range order (SRO) of bulk MPEA from different annealing temperatures T_a. (a) Pairwise SRO of bulk MPEA annealed from different temperatures from 300 K to 2400 K. (b-d) Atomic structure representatives after 2 ns MC/MD calculations at T_a= 300, 600, and 1200 K, respectively.

4.3.2 The kinetics and thermodynamics of SRO

We obtained thermodynamically preferred structures with varying degrees of local chemical SROs by employing MC/MD annealing at different temperatures. We will explore the kinetics of diffusion to achieve these SROs in this section. Based on the assumption that the presence of SROs caused by atomic movements is related to vacancy formation and migration, we calculated vacancy formation energy (E_f^V), the kinetically resolved activation barriers of migration (E_{KRAB})[187] of different diffusing elements in NbMoTaW MPEA. The sum of these two gives the activation energy of self-diffusion (E_a) as shown in Fig. 4.2. We observe that Nb corresponds to the lowest E_f^V, E_{KRAB}, and E_a with the minimum E_{KRAB} of 619 meV.

The ascending order of E_f^V is Nb, Mo, Ta, W, which aligns with the atomic number order. i.e., the elements of period number 5 (Nb and Mo) correspond to lower values of E_f^V compared to the elements with period number 6. While the ascending order of E_{KRAB} is Nb, Ta, Mo, and W, which shows that elements of group VB (Nb, Ta) correspond to the lower value of E_{KRAB} relative to elements of group VIB (Mo, W). The values of E_f^V dominate the values of E_a, therefore the E_a has the same element order as E_f^V.

The ascending order of E_f^V and E_{KRAB} of MPEA align with the corresponding values of pure elements as reported by Ma et al.[188]. The values of E_f^V, E_{KRAB}, and E_a in MPEA are within a range (box plot) compared to the single value in pure elemental cases (bright green line segments) as shown in Fig. 4.2. The majority values of E_a in MPEA are larger than those in the referenced pure metals (Ta, Mo, W) except the Nb case.

Nb has the lowest E_a as a diffusing element in MPEA. This explains the preference of Nb segregation into grain boundary in polycrystalline MPEA, as reported in our previous work[176]. The diffusing difference among Nb, Ta, Mo, and W in MPEA enables the formation of SRO. Those variations in E_a create the rugged energy landscape, which produces the sluggish diffusion just like other MPEAs, as reported in Ref.[189,190].

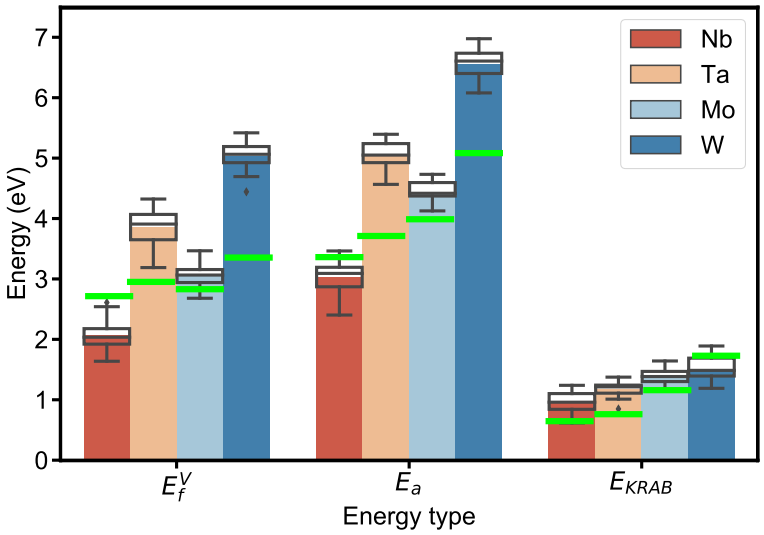

Figure 4.2: Vacancy formation energy (E_f^V), the kinetically resolved activation barriers of migration (E_{KRAB}), and the sum of E_f^V and E_{KRAB} named as activation energy of self-diffusion (E_a) for Nb, Ta, Mo and W in the alloy. The energies in NbMoTaW MPEA are plotted using boxplot. The bright green line segments are the energies of corresponding pure elemental metals (energy values are obtained from Ref.[188]).

4.3.3 The effects of SRO on stacking fault energy and anti-phase boundary energy

The strength and hardness reflect the resistance of a material to plastic deformation. In crystalline solids, plastic deformation most often involves the motion of dislocations. Typically, dislocations prefer to move on the densest plane (slip plane) and along the direction (slip direction) with the highest linear density. $\{110\} < 111 >$ represents the most favorable slip plane and direction combination (i.e., slip system) for bcc alloys. Other possible slip systems for bcc crystal also include $\{112\} < 111 >$ and $\{123\} < 111 >$. The motion of dislocation depends on the stacking fault energy (SFE) and anti-phase boundary energy (APBE).

Fig. 4.3(a) shows the atomic structure we used for SFE and APBE calculations on the $\{110\}$ and $\{112\}$ planes. The x, y, and z correspond to $[112]$, $[\bar{1}10]$, and $[11\bar{1}]$ crystal directions, respectively. The fault on $\{110\}$ plane is obtained by cutting the crystal on $\{110\}$ plane and

shifting the upper part with respect to the lower part along $\langle 111 \rangle$ direction. Similarly, fault on $\{112\}$ can be produced by cutting on $\{112\}$ plane and shifting half of the crystal relative to the other along $\langle 111 \rangle$ direction. The lattice is allowed to relax in the direction perpendicular to the plane of fault. Fig. 4.3 (b) and (c) are the examples of energy landscapes along $\langle 111 \rangle$ direction on $\{110\}$ and $\{112\}$ planes, respectively. Considering the composition fluctuation in MPEA, we sampled 460 faults/APB on $\{110\}$ plane and 100 faults/APB on $\{112\}$ plane. The distribution of SFE and APBE can be seen in Fig. 4.3(e)-(h). The wide range of calculated SFE values is in contrast to a single value for a pure or perfectly ordered crystalline alloy. The mean values of SFE of fault on $\{110\}$ plane are 1390.6, 1379.1, 1363.8, and 1351.2 $\mathrm{mJ/m^2}$ corresponding to annealing temperatures of 300 K, 600 K, 900 K, and 1200 K, respectively. By comparison, the mean values of SFE of fault on $\{112\}$ plane are 1594.0, 1576.4, 1557.5, 1538.0 $\mathrm{mJ/m^2}$ from annealing temperatures of 300 K, 600 K, 900 K, and 1200 K, respectively. The values of SFE of faults on $\{110\}$ plane are about 200 $\mathrm{mJ/m^2}$ lower than the values of SFE of the faults on $\{112\}$ plane of the faults annealed from the same temperature. The SFE strongly correlates with SRO. The sums of the absolute values of SRO of different pairs $|\alpha^1_{ij}|_{sum}$ of structures annealed from different temperatures are shown in Fig. 4.3(d). The value of $|\alpha^1_{ij}|_{sum}$ increases with decreasing annealing temperature. The SFE values increase with the increasing magnitude of SRO. A similar trend has been observed in fcc NiCoCr MPEA system by Ding et al.[175]. Such variation in SFE will affect the mechanical deformation mechanism and hence the mechanical properties. The magnitude of SRO can be controlled by heat treatment. SRO can be used to tune the SFE.

The APBE distribution is shown in Fig. 4.3(g) and (h). For the structures with high SROs (T_a=300 K), APBE is a bimodal distribution. This is a reflection of the pseudo-binary B2 structure. The alternation of chemical occupancy on neighboring sites (i.e., group 5 elements Nb-Ta prefer to occupy cube vertices and group 6 elements Mo-W prefer cube centers) renders APBEs into two sets. The mean values for the low and high energy sets are 9.81 $\mathrm{mJ/m^2}$ and 59.02 $\mathrm{mJ/m^2}$, respectively. The γ-surface for Mo-Nb B2 structure, reported by Natarajan et al.[191], shows the

origin of the bimodal feature of APBE. For structures with relatively low SROs (T_a=600 K, 900 K, 1200 K), the APBE bimodal distributions do not exist. This is because the way we sample the SFE and APBE is by changing the cleavage plane position. Several reference APBEs $\approx 0\ J/m^2$ are attributed to the first peak in APBE distribution in T_a = 600 K, 900 K, 1200 K cases. The mean values of APBE on $\{110\}$ are 59.02, 45.82, 35.54, 34.38 $\mathrm{mJ/m^2}$ from annealing temperatures of 300 K, 600 K, 900 K, and 1200 K, respectively. The mean values of APBE on $\{112\}$ are 78.58, 50.16, 44.71, 39.32 $\mathrm{mJ/m^2}$ from annealing temperatures of 300 K, 600 K, 900 K, and 1200 K, respectively. The lower annealing temperature leads to structures with higher chemical order, which in-turn leads to higher APBE.

4.3.4 SRO-dependent critical resolved shear stress distribution

It is known that 1/2<111> screw dislocation plays an important role in the plasticity of bcc transition metals[192]. Recent experimental studies also revealed the dominant role of screw dislocation in bcc refractory MPEAs[193,194]. Critical resolved shear stress (CRSS) of screw dislocation is a key factor to the strength of the materials. We present how the chemical SRO affects the CRSS as shown in Fig. 4.4. We started from bulk structures that are annealed from T_a = 300 K, 600 K, 900 K, 1200 K which correspond to different SROs. We then created a cylinder shape and implanted one 1/2<111> screw dislocation at the center of the cylinder along the z axis. We sampled the dislocation local environment by varying the center of the cylinder along the intersection points of a 10×10 grid. Therefore, there were 100 samples of dislocation for each SRO. We applied distance-dependent strain rate to enable the dislocation glide on 110 plane along the $< 112 >$ direction and record the stress when the dislocation starts to move (i.e., CRSS). The mean values of CRSS of 1/2<111> dislocations are 1924.1, 1631.0, 1523.5, 1355.8 MPa of SROs from annealing temperatures of 300 K, 600 K, 900 K, and 1200 K, respectively. The higher the SROs, the higher the stress is needed to enable the migration of screw dislocation. Comparing the T_a = 300 K and 1200 K cases, the mean values of CRSS from T_a =300 K is 30% higher than

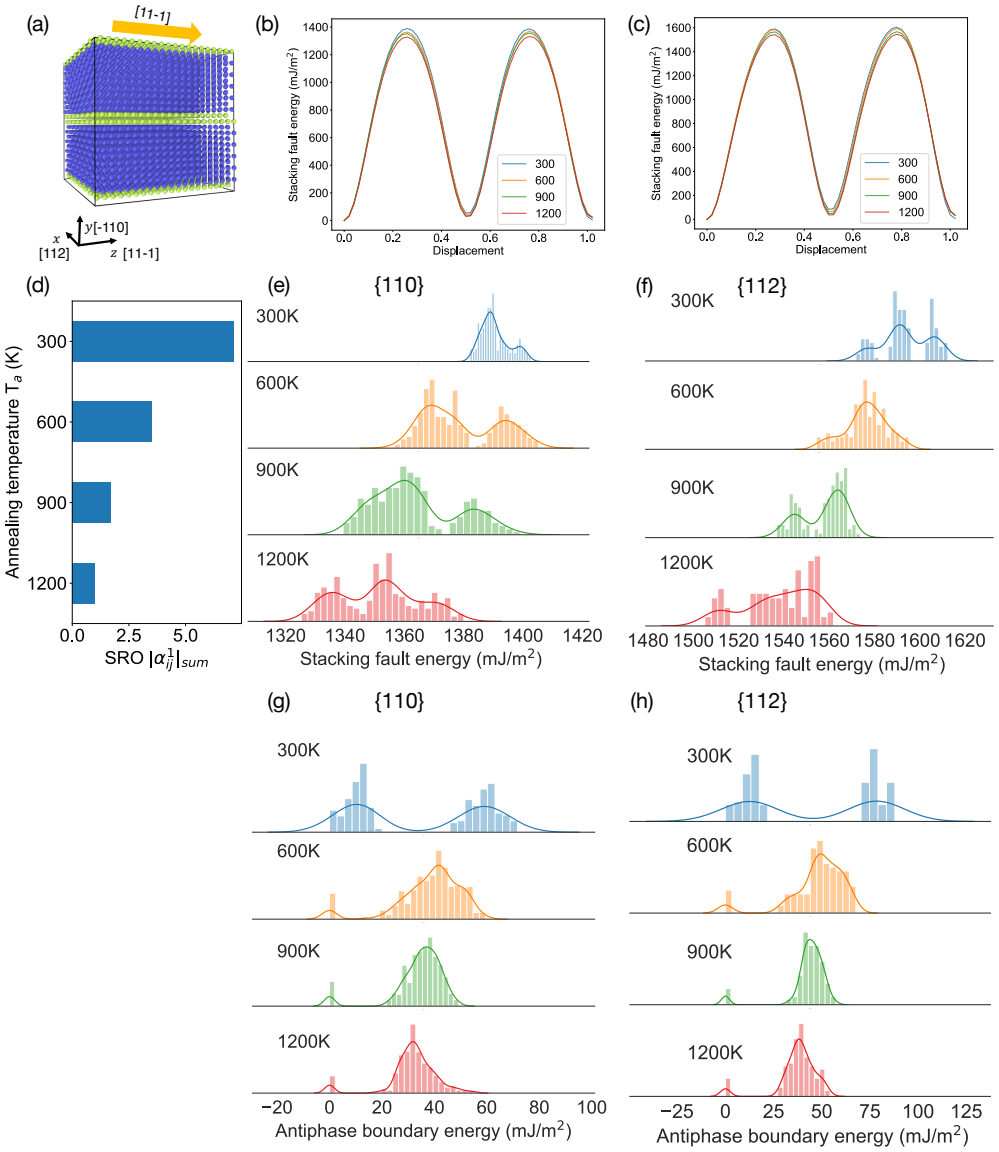

Figure 4.3: Calculated stacking fault energy (SFE) from structures annealed at T_a= 300, 600, 900, and 1200 K, respectively. (a) Representative structure used in SFE calculation. The fault is obtained by cutting the crystal on $\{110\}$ plane and shifting the upper part with respect to the lower part along $\langle 111 \rangle$ direction. (b) and (c) are examples of SFE landscape of faults on $\{110\}$ and $\{112\}$ planes, respectively. The legends represent annealing temperatures. (d) The sum of the absolute values of SRO of different pairs $|\alpha_{ij}^1|_{sum}$ can be tailored by different annealing temperatures. (e) and (f) are the distributions of SFE of faults on $\{110\}$ and $\{112\}$ planes, respectively. (g) and (h) are the distributions of anti-phase boundary energy on $\{110\}$ and $\{112\}$ planes, respectively.

from T_a =1200 K. This indicates that the effect of SRO is quite significant. We can strengthen the materials by increasing the SRO.

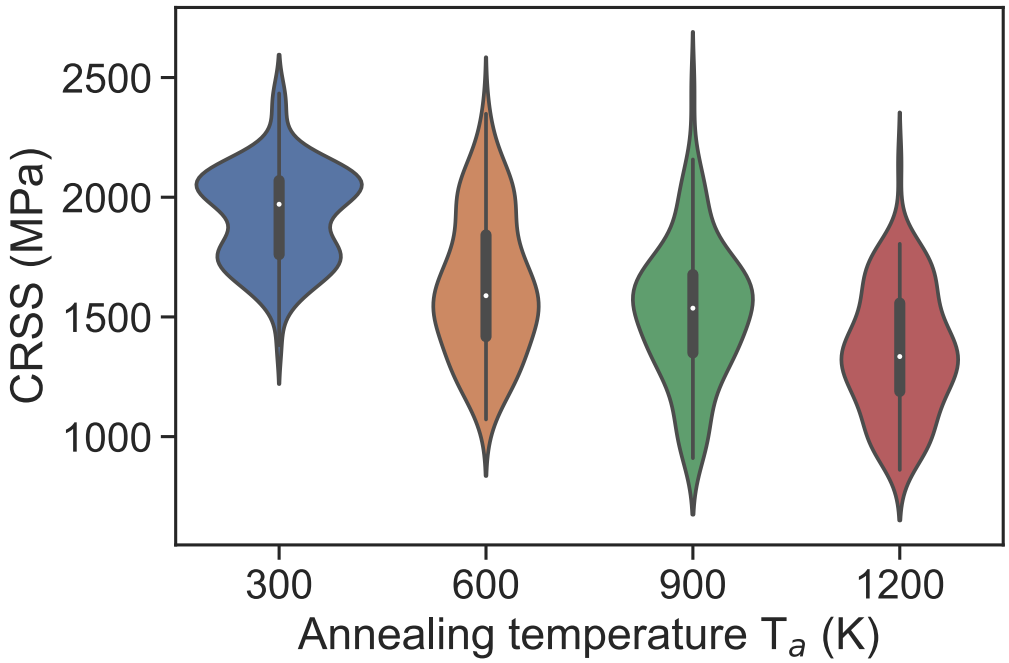

Figure 4.4: The distribution of CRSS is affected by various SROs which correspond to T_a= 300, 600, and 1200 K.

We further investigate how CRSS of dislocation migration is affected by the spatial distribution of SFE and APBE, as shown in Fig. 4.5. For SFE, samples annealed from T_a =300 K have obviously high values of SFE compared with the samples annealed from T_a=600 K, 900 K, 1200 K. The heterogeneous SFEs distribution is observable from the heatmap. There are samples of layers corresponding to higher values of SFE in contrast to other samples of layers. In the heatmap of APBE, an obvious striped pattern is present. This is because the high SROs in samples annealed from 300 K have pseudo-binary B2 structures. This leads to two sets of values of APBE. One set has values close to zero $\mathrm{mJ/m^2}$, and the other set has much higher APBE values. The mountains and valleys of potential energy surfaces contribute to the high value of CRSS. This striped pattern is slightly observable in the sample annealed at 600 K, but not visible in samples annealed from 900 K and 1200 K.

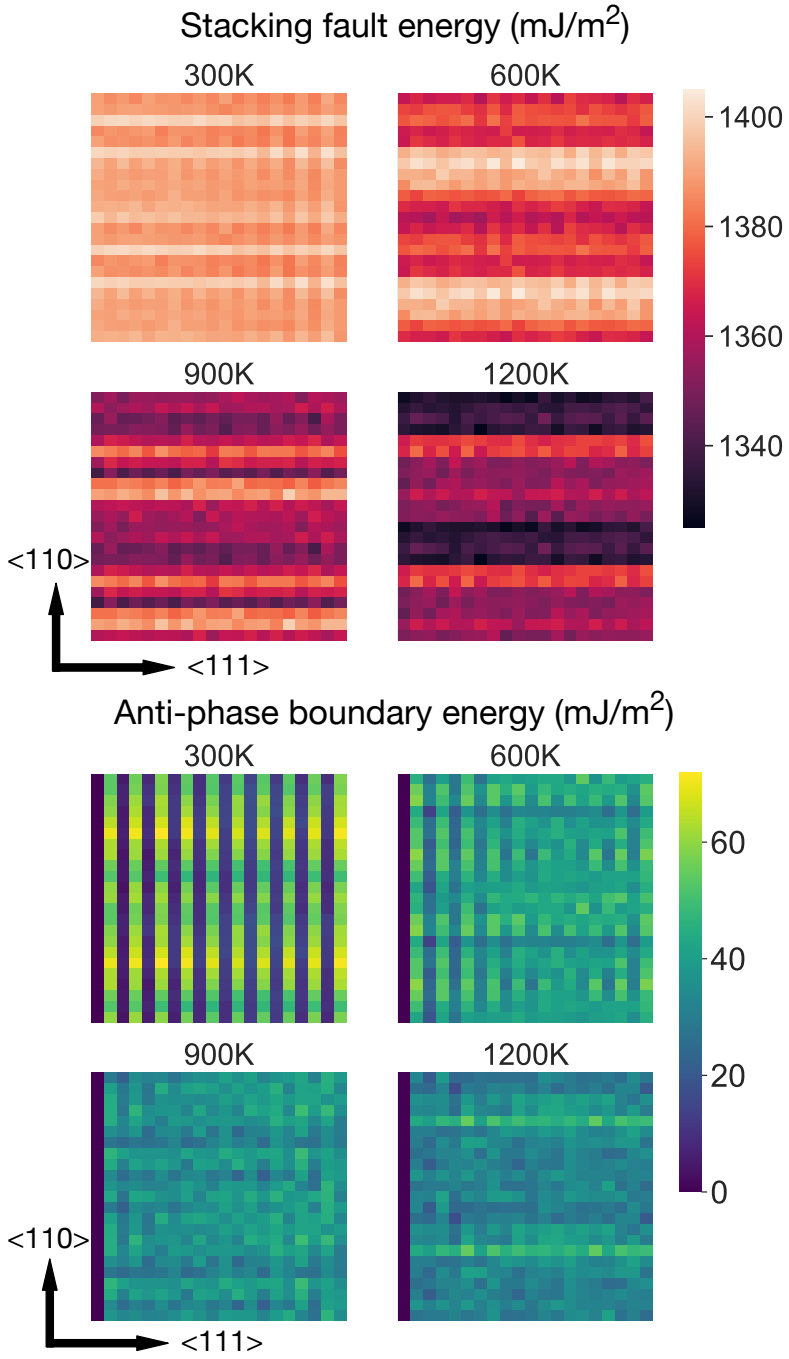

Figure 4.5: The spatial distributions of stacking fault energy and anti-phase boundary energy in samples annealed from T_a = 300 K, 600 K, 900 K, and 1200 K.

4.3.5 The strength and ductility affected by SRO and temperature

Fig. 4.6 shows the uniaxial tensile/compressive tests of MPEA along [001] direction. First, MPEA bulk structures are annealed at different temperatures using MC/MD calculations until equilibria are reached. Then, uniaxial tensile/compressive tests are conducted on these structures. The strain is applied along [001] direction at the same temperatures that are equal to the annealing temperatures as shown in Fig. 4.6(a) legend.

However, in Fig. 4.6(b), the tensile tests are performed at room temperature, and the temperatures shown in the legend are the annealing temperatures at which the structures are processed. i.e., the differences in strain stress curves are solely attributed to the different values of SRO in MPEA structures. In general, compared with Fig. 4.6 (a) and (b), the temperature has a much larger effect on the strength and ductility of MPEA relative to SRO.

For the compressive test, the strength and ductility of MPEA increase monotonically as operating temperature decreases from 2400 K to 300 K, as shown in Fig. 4.6(a). This is different from the tensile test, where the strength and ductility first decrease from 2400 K to 1500 K, then increases from 1200 K to 300 K. Fig. 4.6(b) reveals the sole effect of SRO on strength and ductility. Both strength and ductility increase with the increasing magnitude of SRO. However, the sole SRO effect is not as obvious as the synergy effect of both temperature and SRO. Fig. 4.6(c)-(e) and (f)-(h) correspond to the snapshot of structures of 300 K from compressive and tensile tests, respectively. (c) and (f) are the structures before the magnitude of stress drops dramatically, and (d) and (g) are the snapshot of structures right after the stress drops. The SRO is visible before the stress drop. The snapshot after the stress drop shows the order-disorder transition due to the deformation. Fig. 4.6(e) and (h) are the common neighbor analysis (CNA)[195] for structures corresponding to Fig. 4.6(d) and (g), respectively.

Twins have been observed in the constituent bcc metals, i.e., Nb, Ta, Mo, and W[197]. In the quaternary MPEA, we also observed the twinning under uniaxial tensile deformation as shown in Figure 4.7. Compared with two initial perfect bulk structures, one with RSS and another one

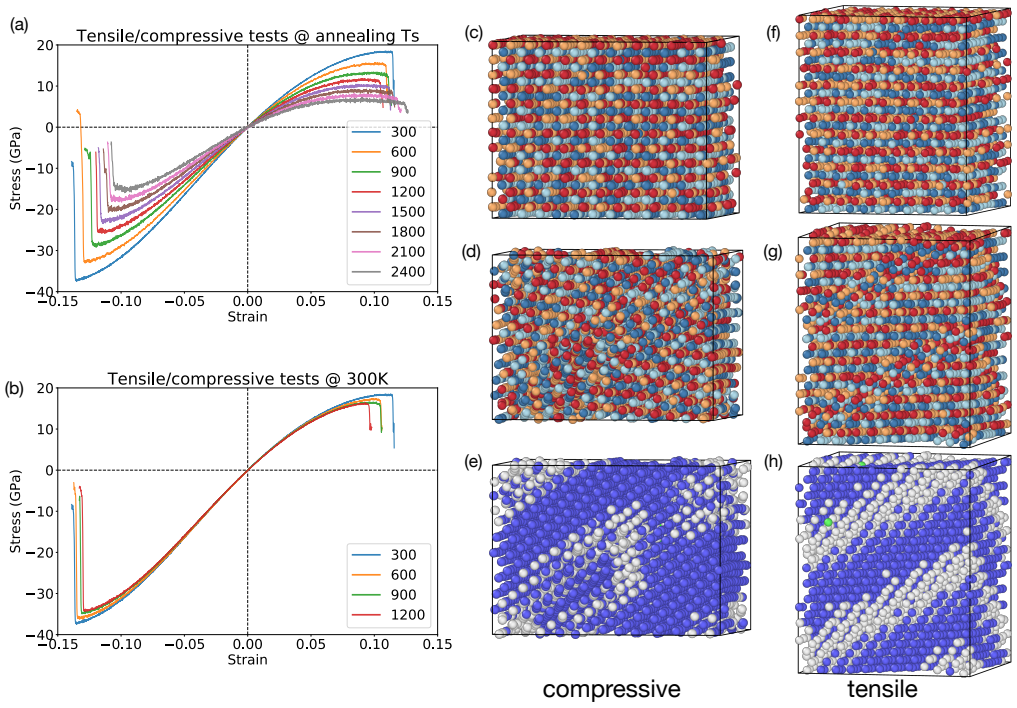

Figure 4.6: Uniaxial tensile/compressive tests of bulk MPEA structures annealed from different temperatures. (a) Uniaxial tensile/compressive tests are conducted at the temperatures shown in the legend, which are equal to T_a. (b) Tests are performed at room temperature. (c) and (f) are the structures (annealed at 300 K) before the magnitude of stress drops dramatically and (d) and (g) are the snapshot of structures right after the stress drops. (e) and (h) are the common neighbor analysis (CNA) for structures of (d) and (g).

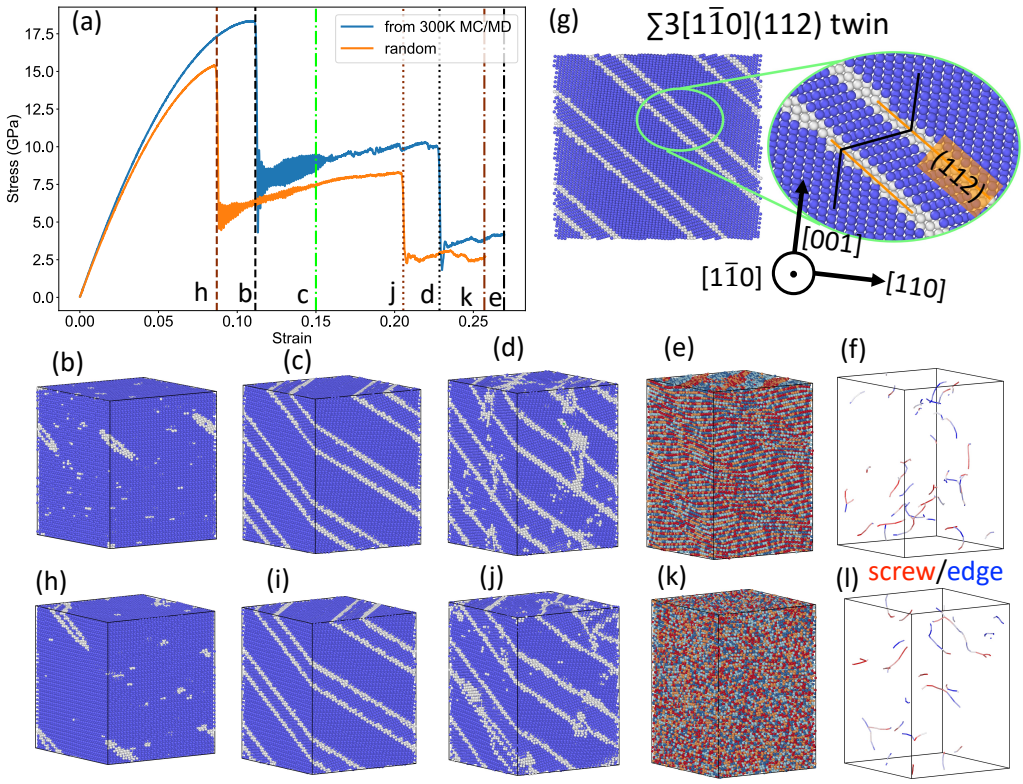

Figure 4.7: Structure evolution under uniaxial tension of bulk MPEA structures with SROs and RSS (a) Strain stress curve of the bulk structures annealed from 300K MC/MD and RSS. (b)-(e) and (h)-(k) correspond to the snapshots of the structures with SROs and RSS, respectively. The letters annotated in (a) directly correspond to the snapshot letters except that the snapshot of 4.7 (i) corresponds to the annotation of green vertical dashed segment c in 4.7(a). 4.7(g) is a slice of structure (c) along $[1\bar{1}0]$ direction to present the (112) twinning. The directions are annotated according. (e) and (k) are the last snapshot of structures with SROs and RSS, respectively. The atoms are colored according to the element types, which are the same as these in Figure 4.1. (f) and (l) are the last snapshots of structures without showing atoms, such that the dislocation lines are visible. Red and blue lines corresponds to screw and edge dislocations, respectively. Snapshots of (b)-(d), (h)-(j), and (g) are colored using the dislocation analysis (DXA)[196] to distinguish bulk and defects atoms.

with large SROs annealed from 300K MC/MD. Twinning is observed in both cases. However, the structure with SROs can bear larger strain before the nucleation of twins. The snapshots of structure evolution are shown in Figure 4.7(b)-(e), and (h)-(k)), where the letters correspond to the annotation letters in Figure 4.7(a) except Figure 4.7(i) corresponds to the annotation letter c in Figure 4.7(a). Figure 4.7(g) is a sliced sample from Figure 4.7(g) along $[1\bar{1}0]$, showing the mirror feature of twinning along (112) plane.

4.3.6 The thermostability of SROs and Nb segregation in nanocrystalline MPEA

To test the thermodynamic stability of chemical SRO, we performed MD simulation at different temperatures for polycrystalline MPEAs with/without SRO. The structures are inherited from our previous work[176]. One is annealed from room temperature MC/MD with SRO and Nb segregation, and the other is a random solid solution. The SRO evolution of two types of polycrystalline MPEA is shown in Fig. 4.8. The high values of SRO are reserved up to 2400 K, as shown in the top panel of Fig. 4.8. While the bottom panel shows that the SRO value is almost invariant at zero, reflecting the RSS feature of the polycrystalline MPEA.

We also observed that the Nb segregation is stable until 2400 K. The presence of SRO and Nb segregation also inhibits the grain coarsening. Fig. 4.9 shows the comparison of structure evolution of polycrystalline MPEA with/without SRO(Nb segregation) at 2400 K. Fig. 4.9(a) is the polycrystalline MPEA started with high SRO and Nb segregation, and Fig. 4.9(b) is the one started with RSS. Under 2400 K MD simulation, we observe that grain sizes in (a) are almost invariant. I.e., SRO and Nb segregation significantly suppressed the grain coarsening. However, in (b) RSS polycrystalline MPEA case, the nanoscale grains coarsen through GB migration and gradually become a single crystal at 2400 K. This phenomenon is quantified in Fig. 4.10. For RSS polycrystalline MPEA, the orange and light orange lines correspond to GB and bcc fractions, respectively. We observed that the GB fraction decreases from 35% to 10%, and the bcc fraction

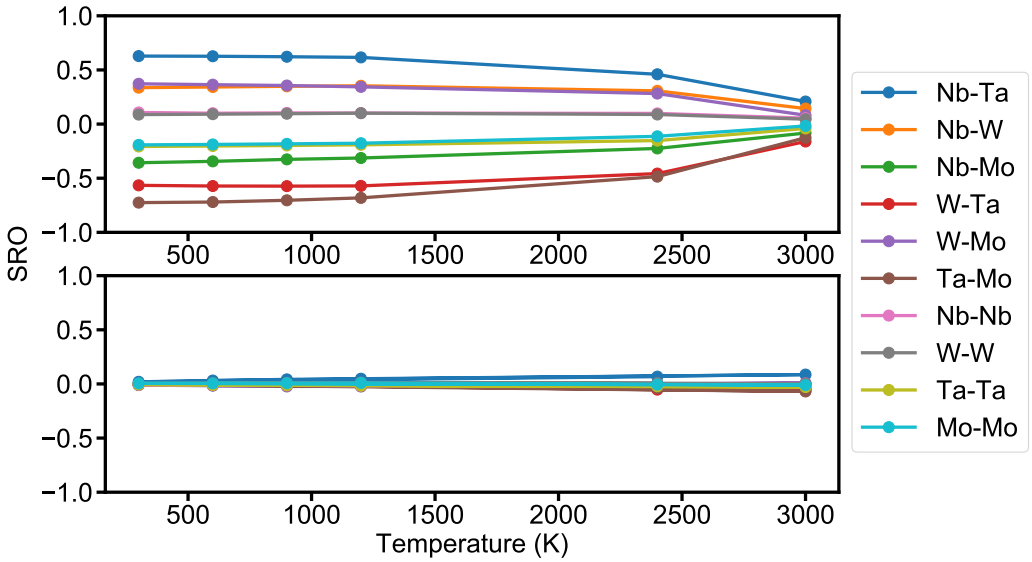

Figure 4.8: The SRO evolution of polycrystalline MPEAs under different temperatures of MD simulations. The top panel corresponds to the structure with Nb segregation and the large SRO. The bottom panel corresponds to a RSS.

bulk increases from 65% to 90% due to the grain growth at 2400 K. While for the polycrystalline MPEA with Nb segregation and high-value SRO, the fraction of bulk bcc and GB region stay invariant through the whole equilibrium status at 2400 K.

The nanoscale grains and Nb GB segregation are reserved up until 2400 K. This reflects the fact that the existence of Nb segregation and SRO pin the GBs and dramatically slow down the migration of GB in contract to the RSS case. This phenomenon also indicates the thermal stability of SRO and Nb segregation up to the ultra-high temperature of 70% T_m.

4.4 Discussion

Using atomistic simulation, we revealed that the annealing temperature in alloy processing controls the local chemical order in bcc NbMoTaW MPEA. The lower the annealing temperature, the higher the SRO. Those chemical fluctuations cause a wide range of SFE, APBE, and CRSS. The higher the local chemical order, the higher the SFE, APBE, and CRSS. The presence of SRO

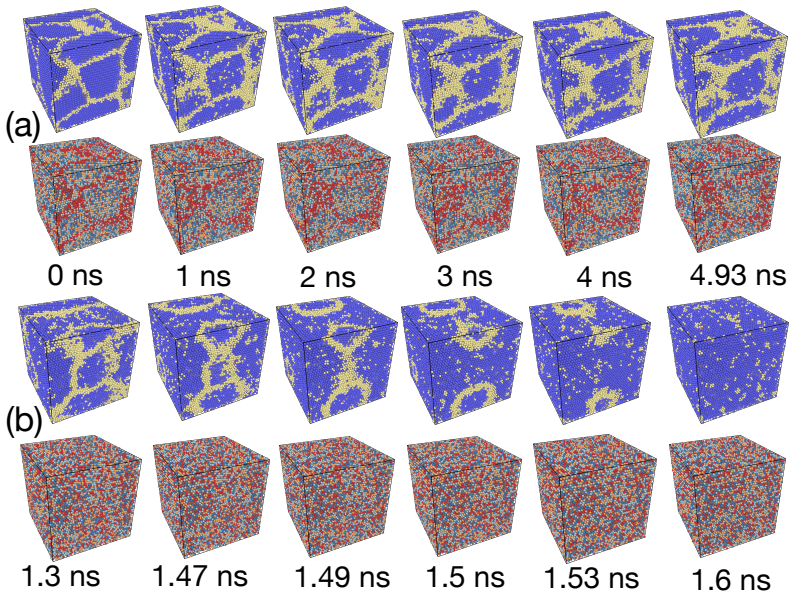

Figure 4.9: The polycrystalline MPEA evolution under 2400 K MD simulation. (a) starts with the initial crystalline MPEA with Nb segregation, and SRO (b) starts with SS polycrystalline MPEA. The first and third rows of atomic structures are colored according to the common neighbor analysis[195] OVITO[198] to distinguish the bcc regions (blue) and grain boundary regions (light yellow). In the second and third rows of structures, atoms are colored using the same code, as shown in Fig. 4.1 where Red, orange, light blue, and blue are corresponding to Nb, Ta, Mo, and W, respectively.

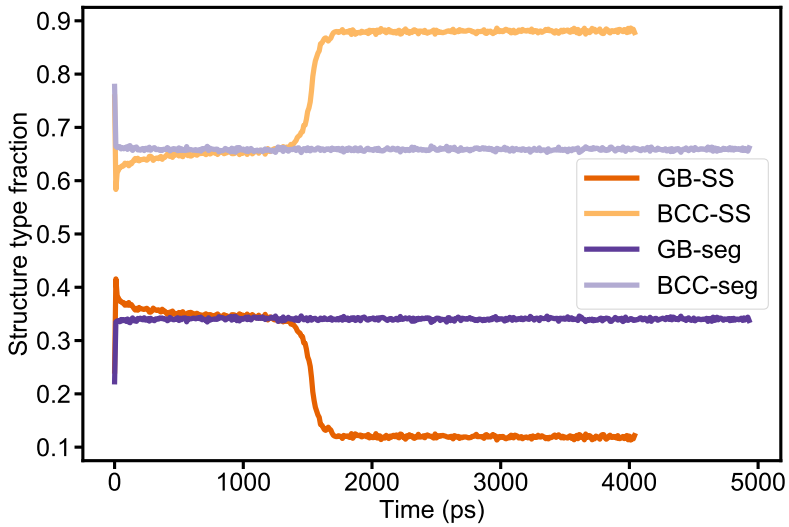

Figure 4.10: The polycrystalline MPEA structure evolution at 2400 K for both random solid solution structure (orange: GB and light orange: bcc bulk) and the structure with high SRO and Nb segregation (purple: GB and light purple: bcc bulk).

also increases the ruggedness of spatial SFE and APBE landscapes, introducing more friction for dislocation migration. This tunable chemical order introduces an additional degree of freedom in producing the designed mechanical properties of bcc MPEA. Similar findings in fcc MPEA have been reported[173,175].

Because the ordered pseudo-binary B2 phase shows the highest strength and ductility. The microstructure with the duplex combination of a disordered bcc phase and an ordered strengthening B2 phase could be a promising design, as reported in other refractory MPEA systems such as $AlMo_{0.5}NbTa_{0.5}TiZr$, $Al_{0.5}Mo_{0.5}NbTa_{0.5}TiZr$, and $Al_{0.25}NbTaTiZr$ systems[169].

The SRO and Nb segregation in polycrystalline MPEA significantly increase the thermal stability of nanocrystalline MPEA against grain coarsening at the temperature of 70% of the melting point. In contrast, grain coarsening usually occurs at temperatures below half of the melting point.

Considering the difficulty in making the single crystal form of bcc NbMoTaW MPEA due to the high melting temperature of the corresponding elemental metals, nanocrystalline MPEA could be an alternative option for high-temperature applications. This is because coarse-grained polycrystalline MPEAs are usually created using arc melting techniques, while nanocrystalline MPEAs can be deposited using magnetron co-sputtering techniques[199]. In addition, our results show that the SRO and Nb segregation can stabilize the grain size and inhibit the grain coarsening up to 2400K. As a result, the desired strength and ductility can be achieved and reserved in nanocrystalline MPEA. As reported in the experiment of NbMoTaW, the yield strength of nanocrystalline MPEA is 1 order of magnitude higher than the corresponding coarse-grain form and 5 times higher than the single crystal form[199].

In a chemically similar system, nanocrystalline (NC) VNbMoTaW is reported to have extremely high hardness (11.4 GPa) compared to the corresponding coarse grain MPEA case (5.25 GPa)[200]. The authors attribute the ultra-high hardness of NC MPEA mainly to the GB strengthening using the Hall-Patch relationship, besides solid solution and dislocation harden-

ing[200].

Besides tuning the SRO, Nb segregation, and grain size, the grain boundary distribution can also be a variable when designing the MPEA with desired properties. As reported recently, the minimal-interface structures constrained by twin boundary networks in polycrystalline Cu achieved extremely fine grains (a few nanometers). Grain coarsening is inhibited until extremely high temperature (equilibrium melting point). The nanocrystalline Cu strength is close to the theoretical value[201]. This finding provides a promising tuning factor in MPEA design. With our ML-IAP, we will be able to explore the effects of grain size and specific grain boundary distribution on the properties of MPEA in the future.

4.5 Conclusion

The mechanical properties of bcc equiatomic NbMoTaW MPEA can be tuned by tailoring the chemical SROs. The SROs can be controlled by adjusting the homogenization annealing temperatures during alloy processing. Samples annealed at intermediate and low annealing temperatures ($T_a \leq 700$ K) present significantly high chemical orders and rugged spatial energy landscapes. In comparison, samples annealed at medium-high (700 K $< T_a \leq 1200$ K) and high-temperature range ($T_a > 1200$ K) show much lower chemical orders and less rugged energy landscapes. The statistical distributions of SFE, APBE, and CRSS of samples with high SROs correspond to high mean values. This positive correlation between SROs and the properties of MPEA (e.g., SFE, APBE, and CRSS) presents a new degree of freedom we can use to tune the mechanical properties of MPEA. The samples with high SROs also show higher strength and ductility under uniaxial tensile and compressive strain due to the twinning mechanism. The SRO and Nb segregation inhibit the grain coarsening in nanocrystalline, which leads to great thermal stability up to temperatures of 70% melting point for MPEA. This stability enables promising practical applications of nanocrystalline MPEA. Achieving the combination of good strength at

high temperatures and good ductility at room temperature is the grand goal for refractory MPEA application. Introducing SRO and Nb segregation by low-temperature annealing is an applicable method to achieve this goal.

Chapter 4, in full, is under preparation for publication of the material ”Predictive processing of NbMoTaW multi-principal element alloy to tune short-range order and mechanical properties” Hui Zheng, Luke Nibbelink, Xiang-Guo Li, Yunxing Zuo, Chi Chen, Shyue Ping Ong. The dissertation author was the primary investigator and author of this paper.

Chapter 5

Summary and Outlook

In this thesis, we have employed quantum mechanics and molecular dynamics computations to investigate various defects, their interactions, and their effects in intermetallic compound $MoSi_2$, 58 types of elemental metals, and equimolar MoNbTaW MPEA.

In the first work, we investigated the interactions between different defects and subsequent effects on $MoSi_2$ using DFT calculations. We revealed that incorporating Zr in the form of interstitial mitigates the embrittling effect of oxygen interstitials at $MoSi_2$ GB. When Zr is introduced as a secondary phase and forming the interface with $MoSi_2$, oxygen interstitials have a strong thermodynamic driving force to migrate to the subsurface of Zr/$MoSi_2$ interface. The interface with/without contaminated oxygen corresponds to higher work of separation compared to the pure $MoSi_2$ GB. The results advance our understanding of Zr as an oxygen getter for $MoSi_2$. Using simple thermodynamic descriptors, we have also identified other elements that may serve as possible getter materials for $MoSi_2$. A similar strategy can be extended to design/screen other potential oxygen getter additives for other alloys/intermetallic systems for improved oxidation resistance and mechanical properties.

The second work presents the most comprehensive database of DFT computed GB energies and work of separation to date, spanning 10 GB types across 58 types of metals. This GB database has been rigorously validated with previous computational values as well as experimental observations. The database provides an overview of the landscape of GB energy distribution of different elements, which has been used as a parameter for estimating the grain size that can achieve the highest ultimate strength in nanocrystalline metals[202,203]. The linear regression model provides an inexpensive estimate for the GB energy of elemental metals using cohesive energy and shear modulus. However, the DFT calculations still limit the size of the simulation cell. Therefore, the types of GBs with large sigma values or with different jointing GB planes. The potential solutions can be made by applying the machine learning multi-fidelity models. Combining the available DFT calculated GB data with ML-IAP calculated GB data with limited elements but covered comprehensive types of GBs to develop a general model that can predict

GB energies of any elements of any given general GB types.

In the third work, we explored the mechanical properties and deformation mechanism of bcc equiatomic NbMoTaW MPEA using the ML-IAP. We found that heat treatment can tailor the local chemical SROs, and consequent stacking fault energy, antiphase boundary energy. Samples annealed at intermediate and low annealing temperatures ($T_a \leq 700$ K) present significantly high SROs and rugged spatial energy landscape than the samples annealed at medium-high (700 K $< T_a \leq 1200$ K) or high-temperature range ($T_a > 1200$ K). The mean values of SFE, APBE, and CRSS of samples with large SROs are higher than those with small SROs. The samples with high SROs also show higher strength and ductility under uniaxial tensile and compressive strain. The trade-off of strength and ductility is overcome by twinning and the presence of local chemical SROs. The local SROs increase the twinning energy. The twins can alleviate the accumulated stress from dislocation pile-up under increasing strain, therefore, increase the ductility. In nanocrystalline, annealing at low temperatures can achieve SROs and Nb segregation. The presence of SROs and Nb segregations increases the thermostability of the nanocrystalline structure by inhibiting the grain coarsening at temperatures as high as 70% melting point for MPEA. This stability enables promising practical applications of nanocrystalline MPEA. Achieving the combination of high strength and ductility at room temperature is the grand goal for refractory MPEA application. Introducing SRO and Nb segregation by low-temperature annealing is an applicable method to achieve this goal. For future work, there is ample space to tune the desired mechanical properties of MPEAs by tunning the composition, which is not covered in this thesis but deserves further exploration.

Appendix A

Supporting information: Role of Zr in Strengthening $MoSi_2$ Grain Boundaries from Density Functional Theory Calculations

Table A.1: Work of separation (in J/m^2) for different cleavages of doped grain boundaries.

Cell scale	1×1			$\sqrt{2} \times \sqrt{2}$			2×2		
Dopant type	2Zr	4O	2Zr+4O	2Zr	4O	2Zr+4O	2Zr	4O	2Zr+4O
Cleave I (mid plane)	2.16	1.82	1.86	2.21	1.80	1.69	2.23	2.03	2.00
Cleave II	4.02	1.42	1.61	4.06	1.63	1.60		2.10	1.90
Cleave III	4.70	3.98	3.66	4.67	3.72	3.34			
Cleave IV		5.72	5.08						

Table A.2: Bader analysis of clean $MoSi_2$ GB as shown in Figure A.4. Negative values indicate electron donors, and positive values indicate electron acceptors

index	58	52	54	56	50
GB Mo	-0.13	-0.13	-0.24	-0.13	-0.13
index	4	6	8	0	2
GB Si	0.15	0.09	0.09	0.08	0.08
index	71	73	75	77	79
GB Si	0.13	0.13	0.16	0.12	0.12
index	101	103	105	107	109
GB Mo	-0.27	-0.14	-0.14	-0.14	-0.14

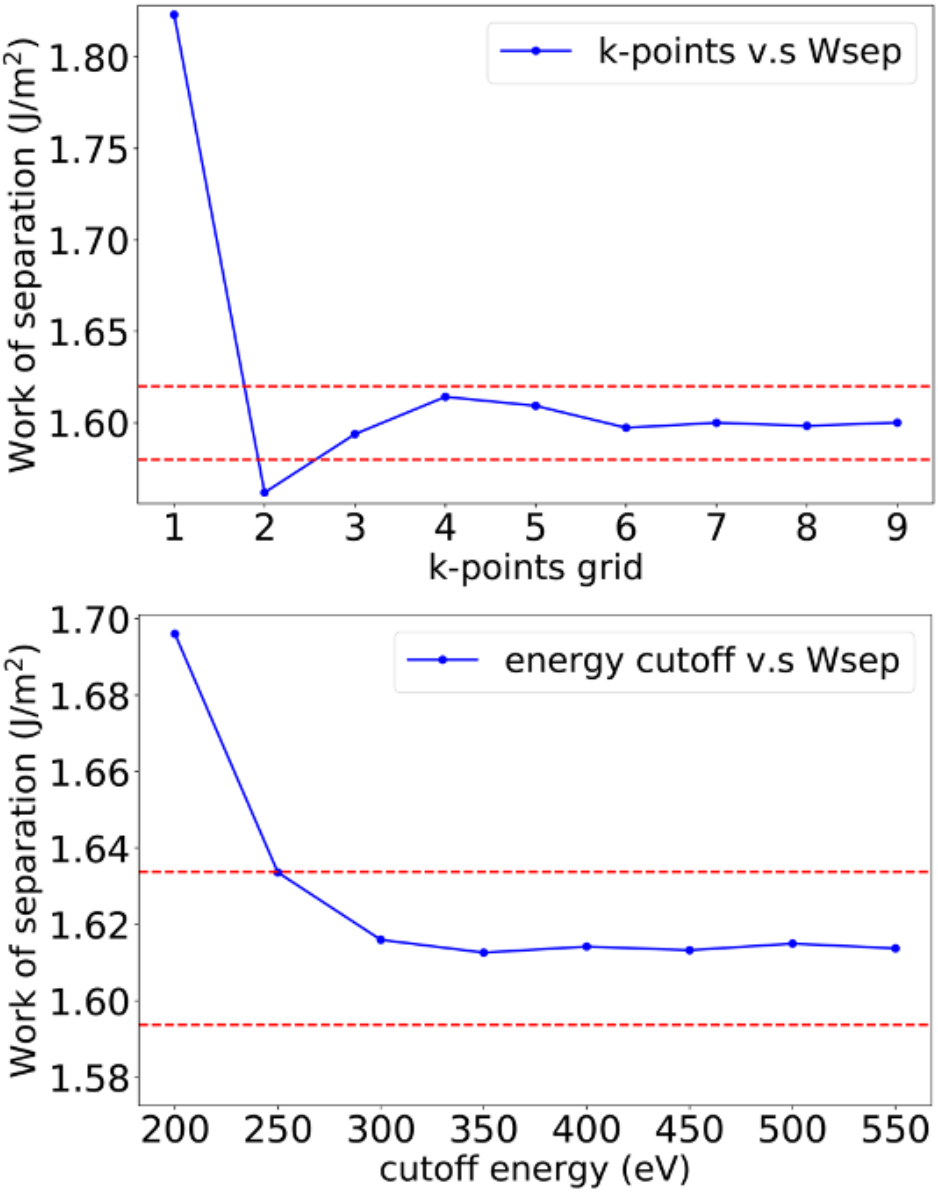

Figure A.1: Convergence of work of separation (W_{sep}) with respect to k-points grid and cutoff energy for ($4O_{int}$ +$2Zr_{Mo}$) doped $MoSi_2$ grain boundary. The W_{sep} are converged to ± 0.02 J/ m^2, as indicated by the red dashed lines.

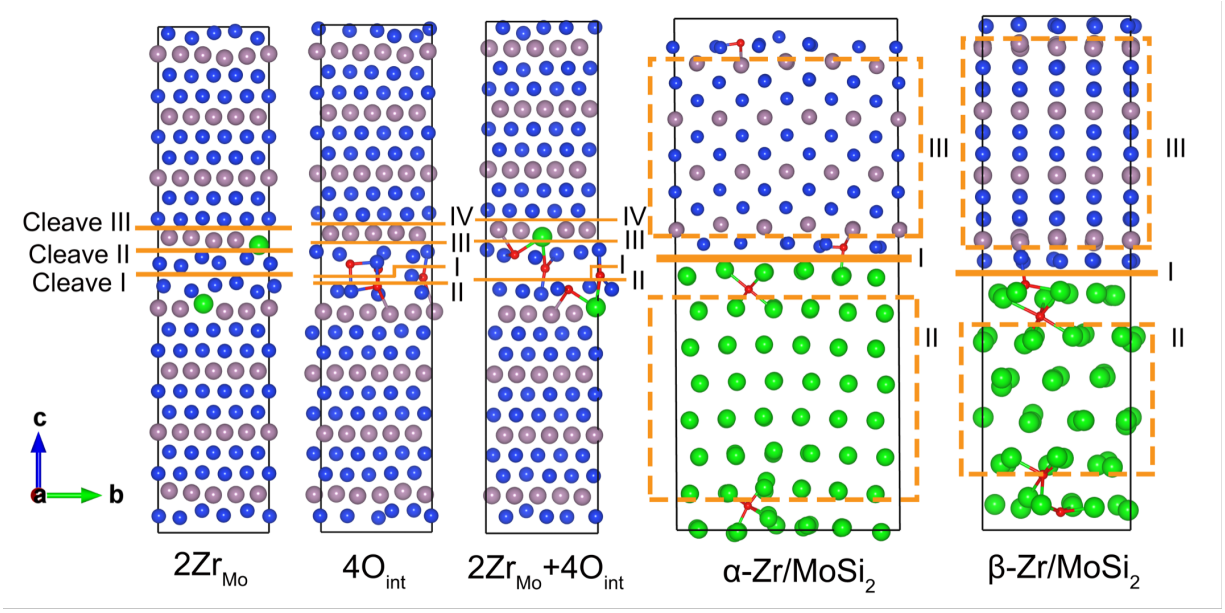

Figure A.2: Schematic showing different cleavages for doped grain boundaries and interfaces.

Table A.3: Bader analysis of $4O_int$ doped $MoSi_2$ grain boundary as show in Figure A.5. Negative values indicate electron donors, and positive values indicate electron acceptors.

index	98	92	94	96	90
Mo	-0.23	-0.26	-0.31	0.06	-0.18
index	4	6	8	0	2
Si	-0.98	0.06	-2.44	0.19	-0.12
index	51	53	55	57	59
Si	0.08	-1.68	-0.79	-0.88	0.01
index	101	103	105	107	109
Mo	-0.36	-0	-0.31	-0.35	-0.14
Index	120	121	122	123	
O	1.96	2.03	1.94	2.05	

Table A.4: Bader analysis of Zr_{Mo} doped $MoSi_2$ grain boundary as shown in Figure A.6. Negative values indicate electron donors, and positive values indicate electron acceptors.

index	5	2	3	4	0 (Zr)
Mo	0.04	0.34	0.054	0.29	-1.30
index	14	16	18	10	12
Si	0.06	0.12	0.06	-0.02	0.12
index	61	63	65	67	69
Si	-0.02	0.13	0.116	0.16	0.20
index	6	7	1(Zr)	8	9
Mo	0.23	0.05	-1.30	0.16	0.04

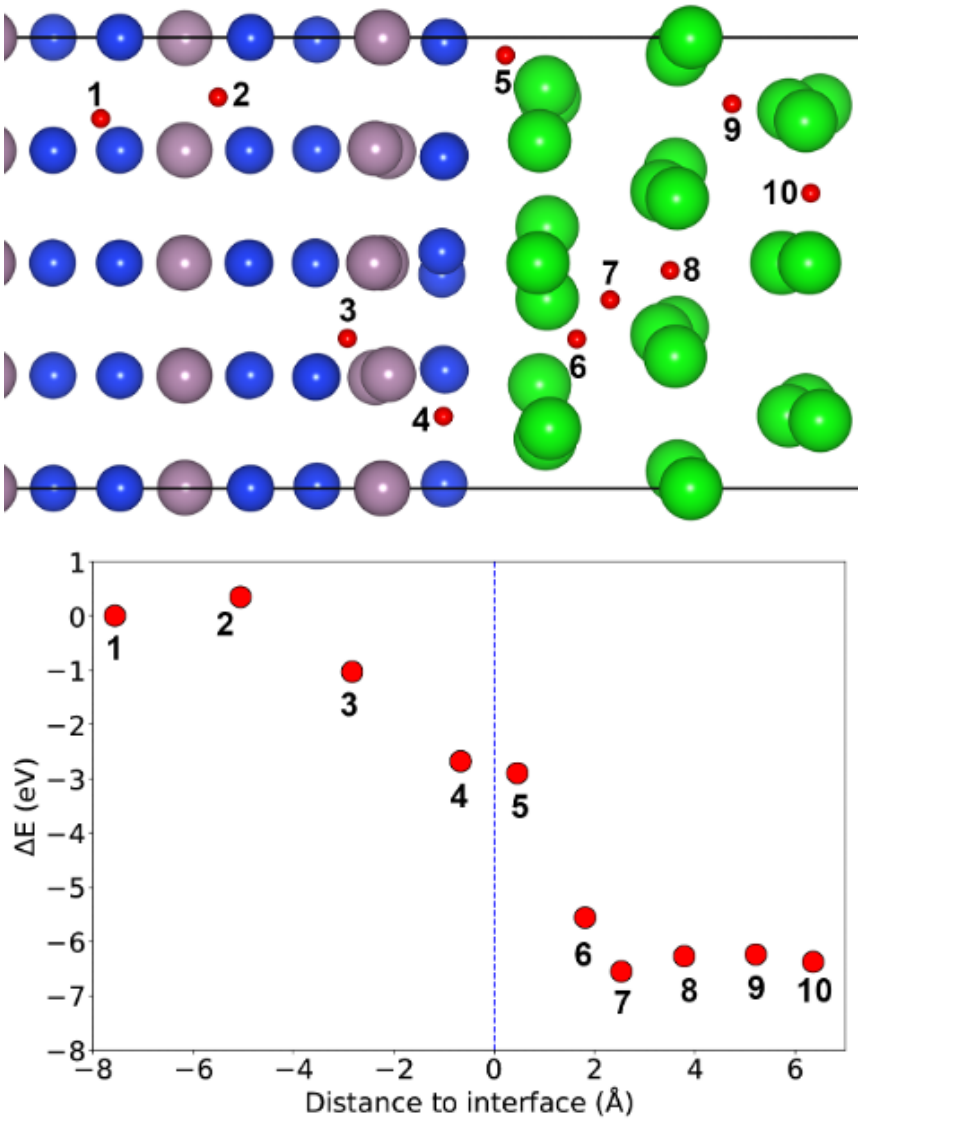

Figure A.3: Relative energies (ΔE) of one O_{int} defect at different regions of β-Zr/$MoSi_2$. The zero of the energy is set at the energy of the structure with O_{int} in bulk-like $MoSi_2$ (position 1)

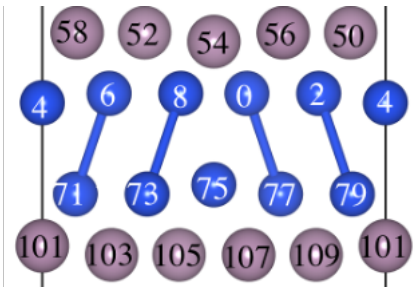

Figure A.4: Bader analysis of clean $MoSi_2$ GB as shown in Table A.2. Negative values indicate electron donors, and positive values indicate electron acceptors.

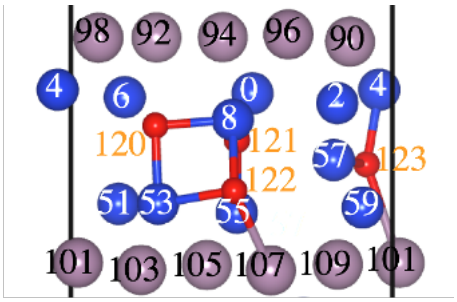

Figure A.5: Bader analysis of $4O_int$ doped $MoSi_2$ grain boundary. Negative values indicate electron donors, and positive values indicate electron acceptors.

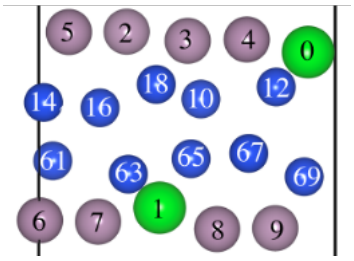

Figure A.6: Bader analysis of Zr_{Mo} doped $MoSi_2$ grain boundary. Negative values indicate electron donors, and positive values indicate electron acceptors.

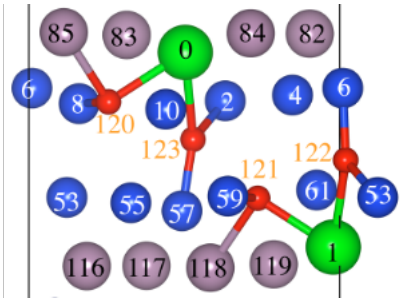

Figure A.7: Bader analysis of $4O_{int}$+$2Zr_{Mo}$ doped $MoSi_2$ GB. Negative values indicate electron donors, and positive values indicate electron acceptors.

Table A.5: Bader analysis of $4O_{int}$+$2Zr_{Mo}$ doped $MoSi_2$ GB as shown in Figure A.7. Negative values indicate electron donors, and positive values indicate electron acceptors.

index	85	83	0 (Zr)	84	82
Mo	-0.28	-0.00	-1.63	-0.13	-0.0372
index	6	8	10	2	4
Si	-0.91	-0.99	0.08	-0.66	0.059
index	53	55	57	59	61
Si	-0.66	0.03	-0.93	-0.91	0.08
index	116	117	118	119	1 (Zr)
Mo	-0.09	0.01	-0.31	-0.01	-1.64
index	120	123	121	122	
O	1.66	2.05	1.67	2.06	

Table A.6: Work of separation W_{sep} in J/m^2 for different cleavages of doped/un-doped $\alpha - Zr/MoSi_2$ and $\beta - Zr/MoSi_2$ interface.

	$\alpha - Zr/MoSi_2$	$\alpha - Zr/MoSi_2$	$\beta - Zr/MoSi_2$	$\beta - Zr/MoSi_2$
	Un-doped	$4O_{int}$-doped	Un-doped	$4O_{int}$-doped
Cleave-I mid-plane	3.57	3.52	3.54	3.21
Cleave II	3.17	2.93	3.01	2.75
Cleave III	5.20	4.46	4.80	4.56

Table A.7: Strain effect on the surface energy for the cleavage (II in Figure A.2) with the lowest work of separation of α-Zr/$MoSi_2$ interface.

Surface	$\gamma_{strainfree}$ (J/m^2)	$\gamma_{strained}$ (J/m^2)	% change
Hcp Zr slab	1.52	1.54	1.32 %
$MoSi_2$ + 2 Zr Layers	1.97	1.96	-0.51 %

Appendix B

Supporting information: Grain boundary properties of elemental metals

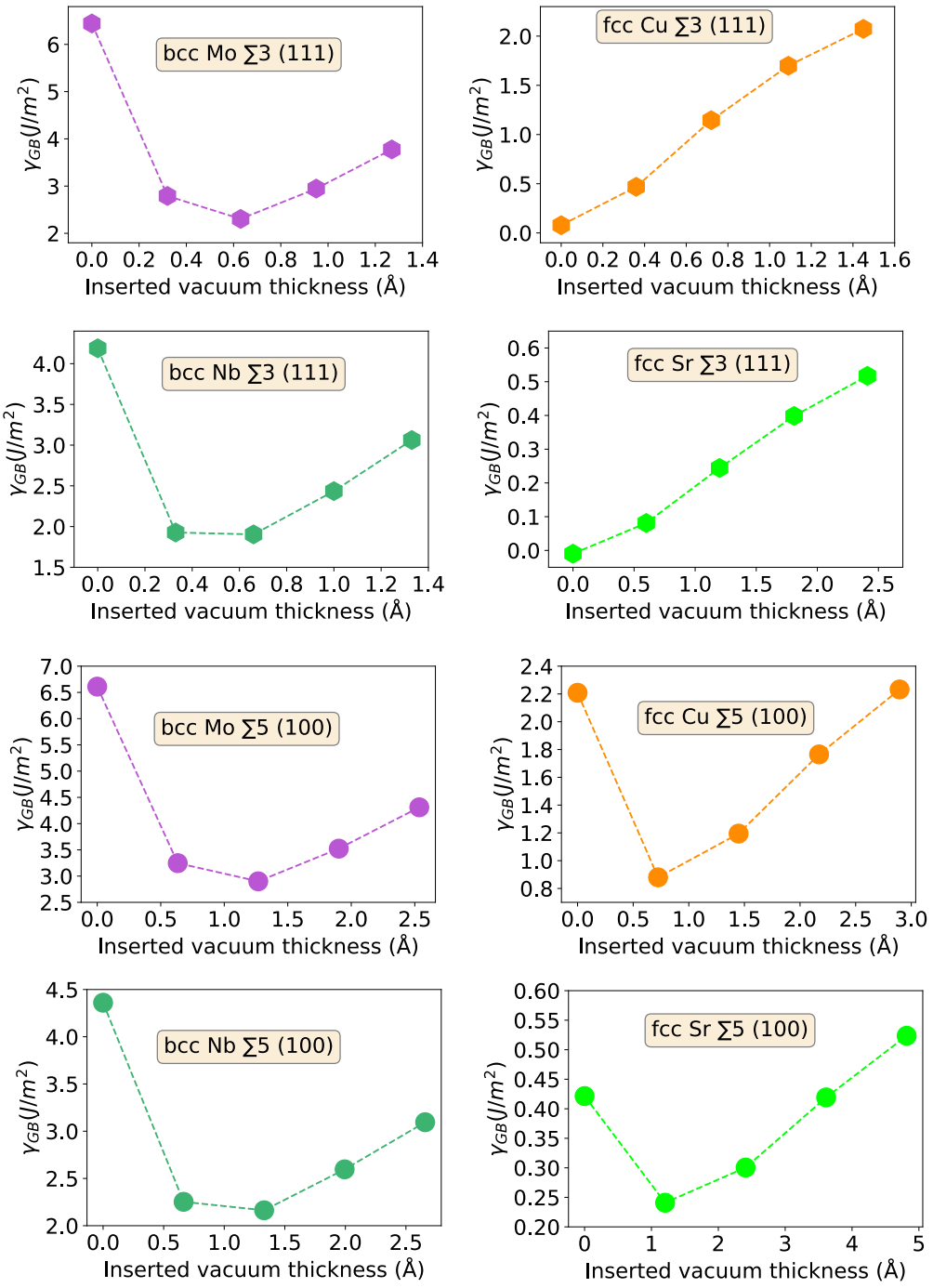

Figure B.1: Lattice translation tests (along *c* direction) for twist GBs.

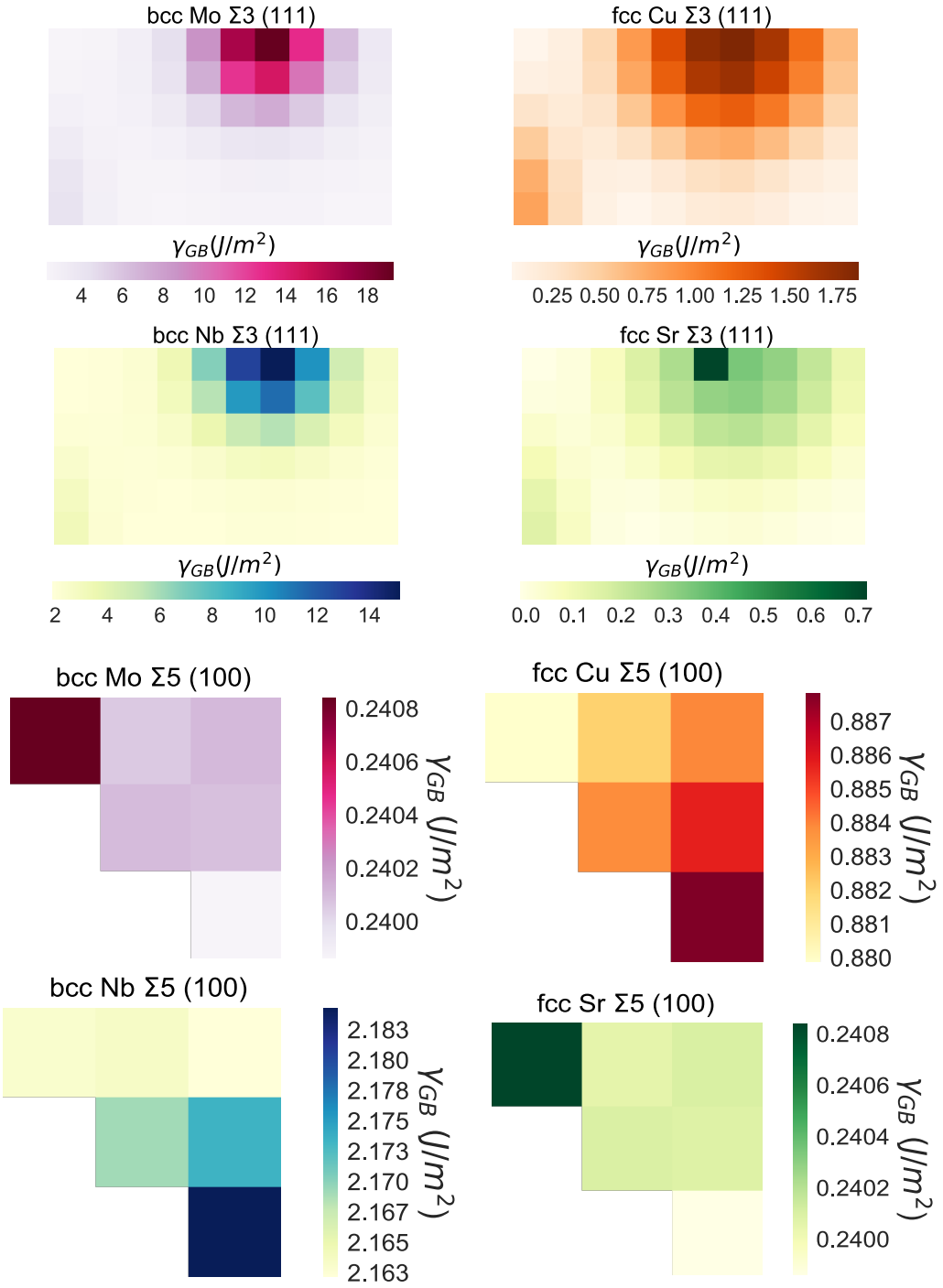

Figure B.2: Lattice translation tests (along *a* and *b* directions) for twist GBs.

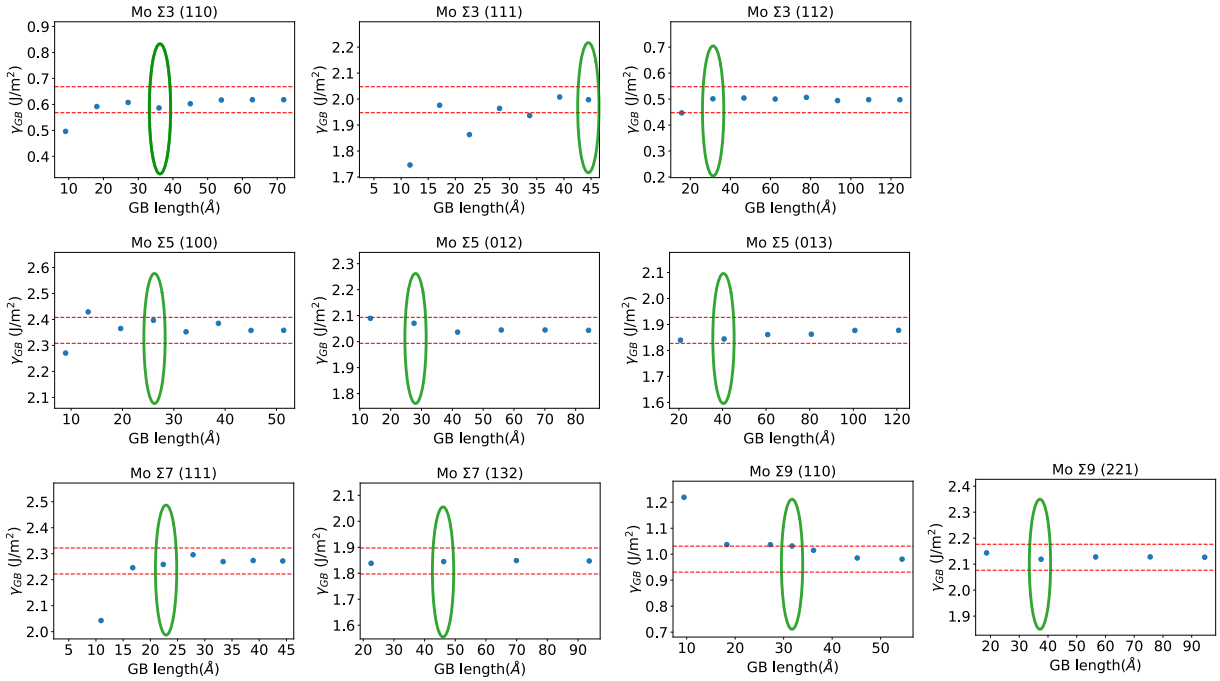

(a) bcc Mo

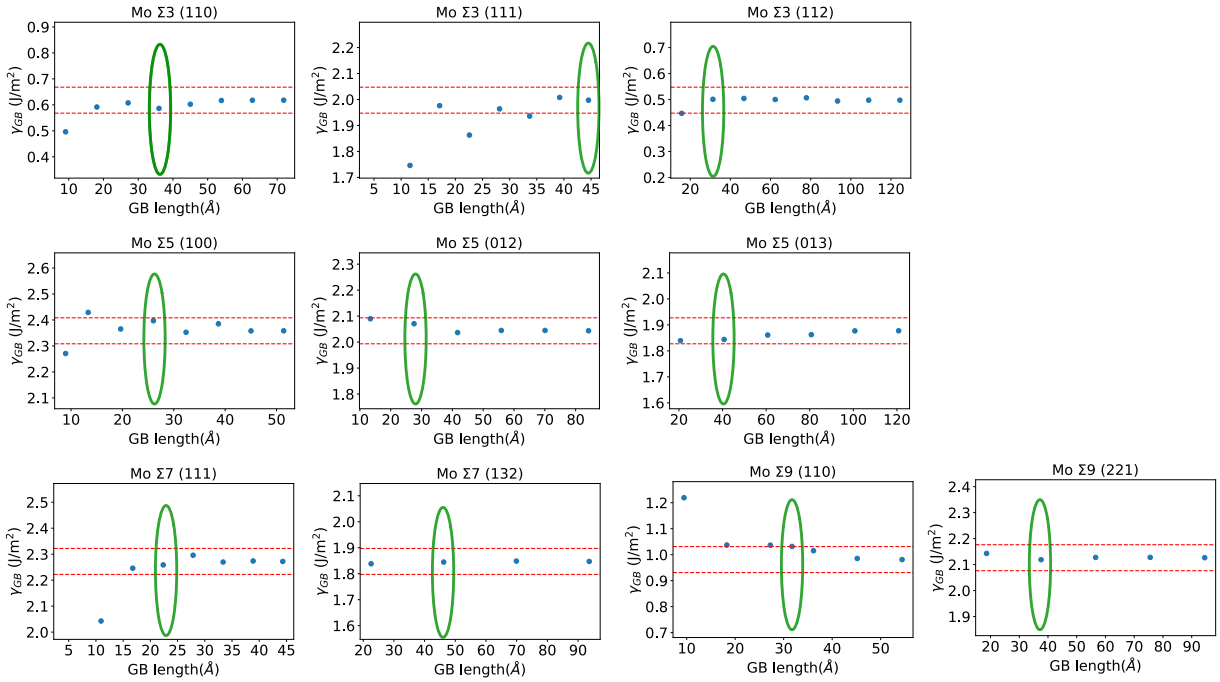

(b) fcc Cu

Figure B.3: GB length convergence tests of bcc Mo and fcc Cu

Table B.1: Force convergence test of Mo Σ3 (112) GB

EDIFFG (eV/Å)	energy per atom (eV)	γ_{GB} (J/m^2)
-0.0200	-10.814099	0.482336
-0.0100	-10.814100	0.482203
-0.0050	-10.814100	0.482203
-0.0010	-10.814107	0.482092
-0.0005	-10.814112	0.482034
-0.0001	-10.814112	0.482034

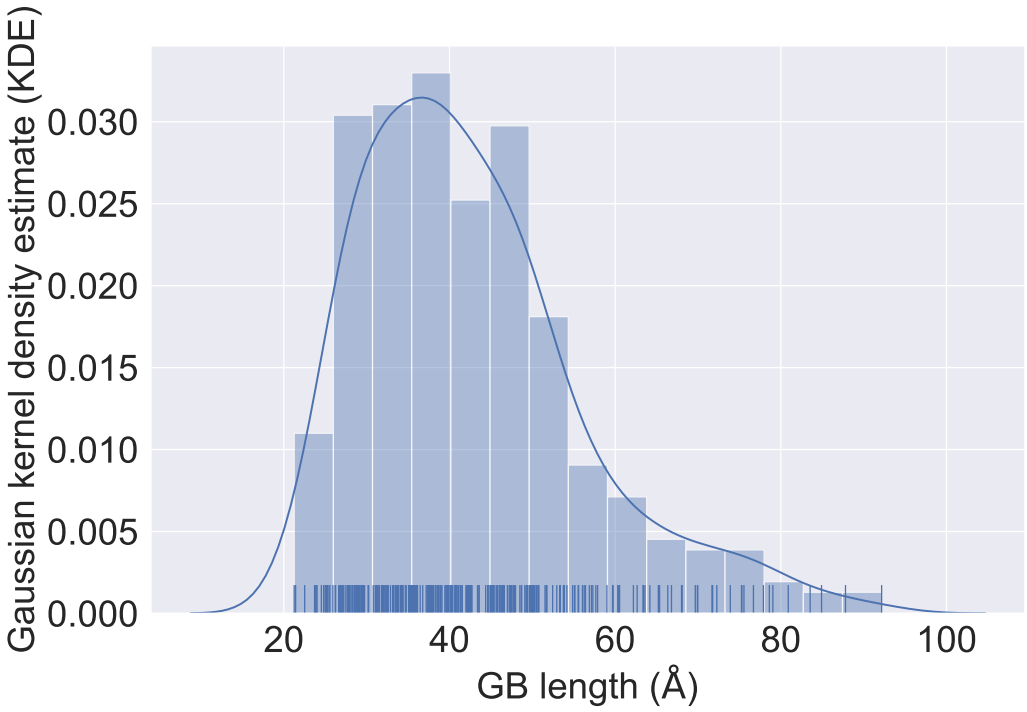

Figure B.4: GB length distribution of all 327 GBs.

Table B.2: 3D shift test, where the *a* and *b* shifts are in GB lattice units and the *c* shift is in units of Å. γ_{GB}^{static} (J/m^{-2}) and γ_{GB}^{relax} (J/m^{-2}) represent the GB energy of selected low energy 3D shifts from static calculations and subsequent relaxation, respectively. Δ_{GB}^{relax} is the relaxed GB energy difference between the un-shifted GB structure and the most favorable shifted GB.

	GB type	*a* shift	*b* shift	*c* shift	γ_{GB}^{relax}	γ_{GB}^{static}	#atoms	Δ_{GB}^{relax}
0	MoΣ3(110)	0.000	0.000	0.00	0.642	0.748	48	
1	MoΣ3(110)	0.500	0.000	0.00	0.654	0.758	48	0.013
2	MoΣ3(112)	0.000	0.000	0.00	0.598	0.696	24	
3	MoΣ3(112)	0.875	0.000	0.00	0.599	0.724	24	0.001
4	MoΣ5(012)	0.500	0.125	0.63	2.038	2.457	40	
5	MoΣ5(012)	0.500	0.125	0.32	2.040	2.430	40	
6	MoΣ5(012)	0.000	0.000	0.00	2.070	2.643	38	0.032
7	MoΣ5(013)	0.250	0.000	0.32	1.653	2.078	40	
8	MoΣ5(013)	0.000	0.000	0.00	1.778	3.772	40	0.125
9	MoΣ7(123)	0.750	0.125	0.63	1.900	2.561	56	
10	MoΣ7(123)	0.750	0.250	0.63	1.904	2.515	56	
11	MoΣ7(123)	0.750	0.000	0.63	1.905	2.521	56	
12	MoΣ7(123)	0.750	0.125	0.32	1.906	2.662	56	
13	MoΣ7(123)	0.500	0.000	0.63	1.910	2.603	56	
14	MoΣ7(123)	0.000	0.000	0.00	1.926	2.922	54	0.026
15	MoΣ9(122)	0.125	0.500	0.63	2.060	2.669	72	
16	MoΣ9(122)	0.375	0.750	0.63	2.060	2.729	72	
17	MoΣ9(122)	0.375	0.750	0.00	2.069	3.015	70	
18	MoΣ9(122)	0.000	0.000	0.00	2.137	2.843	70	0.077
19	NbΣ3(110)	0.500	0.000	0.00	0.365	0.540	48	
20	NbΣ3(110)	0.000	0.000	0.00	0.407	0.552	48	0.042

21	NbΣ3(112)	0.875	0.500	0.00	0.320	3.037	22	
22	NbΣ3(112)	0.000	0.000	0.00	0.354	0.511	24	0.034
23	NbΣ5(012)	0.000	0.000	0.00	1.305	1.859	38	
24	NbΣ5(012)	0.500	0.125	0.33	1.326	1.588	40	
25	NbΣ5(012)	0.500	0.125	0.66	1.326	1.801	40	0.021
26	NbΣ5(013)	0.000	0.000	0.00	1.281	2.316	40	
27	NbΣ5(013)	0.250	0.000	0.33	1.287	1.624	40	0.005
28	NbΣ7(123)	0.500	0.000	0.66	1.185	1.910	56	
29	NbΣ7(123)	0.750	0.125	0.33	1.189	1.876	56	
30	NbΣ7(123)	0.750	0.250	0.33	1.194	1.886	56	
31	NbΣ7(123)	0.750	0.375	0.66	1.198	1.896	56	
32	NbΣ7(123)	0.000	0.000	0.00	1.200	1.992	54	0.015
33	NbΣ7(122)	0.375	0.750	0.00	1.301	2.054	70	
34	NbΣ7(122)	0.125	0.500	0.66	1.306	2.031	72	
35	NbΣ7(122)	0.000	0.000	0.00	1.350	2.026	70	0.050

Table B.3: Comparison between full grid search and two-step search scheme for Mo and Nb GBs. Only five lowest GB energy translations are shown at each step. It can be seen that the two schemes find essentially similar low energy translations.

a shift	b shift	c shift	γ_{GB} (Jm^{-2})	a shift	b shift	c shift	γ_{GB} (Jm^{-2})
Mo				Nb			
Σ3 (110)				Σ3(110)			
Full grid search				Full grid search			
0.000	0.000	0.00	0.748	0.500	0.000	0.00	0.540

0.500	0.000	0.00	0.758	0.000	0.000	0.00	0.552
0.000	0.000	0.32	0.961	0.500	0.000	0.33	0.664
0.500	0.000	0.32	0.961	0.000	0.000	0.33	0.668
0.000	0.375	0.00	0.974	0.500	0.375	0.00	0.671
Step 1: c search				Step 1: c search			
0.000	0.000	0.00	0.748	0.000	0.000	0.00	0.552
0.000	0.000	0.32	0.961	0.000	0.000	0.33	0.668
0.000	0.000	0.63	1.932	0.000	0.000	0.66	1.250
0.000	0.000	0.95	2.981	0.000	0.000	1.00	1.942
0.000	0.000	1.27	3.833	0.000	0.000	1.33	2.582
Step 2: a-b search				Step 2: a-b search			
0.000	0.000	0.00	0.748	0.500	0.000	0.00	0.540
0.500	0.000	0.00	0.758	0.000	0.000	0.00	0.552
0.000	0.375	0.00	0.974	0.500	0.375	0.00	0.671
0.500	0.375	0.00	0.984	0.000	0.375	0.00	0.688
0.000	0.250	0.00	1.583	0.500	0.250	0.00	0.965
Σ3 (112)				Σ3(112)			
Full grid search				Full grid search			
0.000	0.000	0.00	0.696	0.875	0.000	0.00	0.443
0.875	0.000	0.00	0.724	0.000	0.000	0.00	0.511
0.125	0.000	0.00	0.891	0.125	0.000	0.00	0.618
0.000	0.000	0.32	0.898	0.875	0.000	0.33	0.664
0.875	0.000	0.32	0.916	0.000	0.000	0.33	0.679
Step 1: c search				Step 1: c search			
0.000	0.000	0.00	0.696	0.000	0.000	0.00	0.511

0.000	0.000	0.32	0.898	0.000	0.000	0.33	0.679
0.000	0.000	0.63	1.802	0.000	0.000	0.66	1.304
0.000	0.000	0.95	2.856	0.000	0.000	1.00	2.059
0.000	0.000	1.27	3.769	0.000	0.000	1.33	2.768
	Step 2: a-b search				Step 2: a-b search		
0.000	0.000	0.00	0.696	0.875	0.000	0.00	0.443
0.875	0.000	0.00	0.724	0.000	0.000	0.00	0.511
0.125	0.000	0.00	0.891	0.125	0.000	0.00	0.618
0.250	0.000	0.00	1.245	0.250	0.000	0.00	0.775
0.875	0.125	0.00	1.813	0.875	0.125	0.00	1.095
	Σ5 (013)				Σ5(013)		
	Full grid search				Full grid search		
0.250	0.000	0.32	2.078	0.000	0.000	0.33	1.502
0.000	0.000	0.32	2.145	0.250	0.000	0.33	1.624
0.250	0.750	0.32	2.260	0.250	0.750	0.33	1.625
0.000	0.000	0.63	2.308	0.000	0.000	0.66	1.699
0.250	0.000	0.63	2.335	0.500	0.000	0.33	1.731
	Step 1: c search				Step 1: c search		
0.000	0.000	0.32	2.145	0.000	0.000	0.33	1.502
0.000	0.000	0.63	2.308	0.000	0.000	0.66	1.699
0.000	0.000	0.95	3.030	0.000	0.000	1.00	2.223
0.000	0.000	0.00	3.772	0.000	0.000	0.00	2.316
0.000	0.000	1.27	3.829	0.000	0.000	1.33	2.801
	Step 2: a-b search				Step 2: a-b search		
0.250	0.000	0.32	2.078	0.000	0.000	0.33	1.502

0.000	0.000	0.32	2.145	0.250	0.000	0.33	1.624
0.250	0.750	0.32	2.260	0.250	0.750	0.33	1.625
0.500	0.000	0.32	2.369	0.500	0.000	0.33	1.731
0.000	0.750	0.32	2.808	0.000	0.750	0.33	2.021

The GB structures, energies and work of separation can also be found on Materials Project (`https://materialsproject.org/`) website. The material IDs (mp-ids) of corresponding elements can be found in Table B.9

Table B.4: Grain boundary energies (J/m^2) of cubic elements.

sigma	Σ3	Σ3	Σ3	Σ5	Σ5	Σ5	Σ7	Σ7	Σ9	Σ9
plane	(011)	(111)	(112)	(001)	(012)	(013)	(111)	(123)	(011)	(122)
Ba	0.045	0.182	0.026	0.279	0.144	0.161	0.254	0.135	0.098	0.187
Cr	0.675	1.981	0.645	2.646	2.195	1.977	2.335	1.901	1.178	2.253
Cs	-0.002	0.013	-0.000	0.021	0.013	0.021	0.007	0.011	-0.004	0.019
Fe	0.508	1.598	0.423	2.243	1.892	1.560	1.904	1.419	0.970	1.754
K	0.032	0.077	0.025	0.088	0.057	0.073	0.046	0.063	0.023	0.071
Li	0.046	0.171	0.054	0.269	0.150	0.156	0.213	0.142	0.082	0.202
Mo	0.503	1.743	0.480	2.432	2.029	1.727	2.210	1.732	1.040	2.064
Na	0.063	0.123	0.044	0.138	0.082	0.132	0.142	0.086	0.074	0.129
Nb	0.294	1.286	0.252	1.492	1.242	1.200	1.343	1.018	0.598	1.271
Rb	0.001	0.048	0.008	0.060	0.034	0.045	0.024	0.026	0.008	0.043
Ta	0.334	1.526	0.289	1.925	1.412	1.438	1.558	1.216	0.732	1.508
V	0.322	1.176	0.258	1.383	1.204	1.262	1.255	0.941	0.611	1.210
W	0.714	2.242	0.665	3.205	2.654	2.204	2.866	2.327	1.400	2.806
Ag	0.545	0.069	0.427	0.419	0.593	0.553	0.208	0.542	0.710	0.507
Al	0.456	-0.004	0.310	0.383	0.532	0.476	0.135	0.501	0.713	0.430
Au	0.458	0.026	0.338	0.323	0.520	0.447	0.175	0.441	0.607	0.393
Ca	0.239	0.018	0.204	0.262	0.303	0.302	0.109	0.307	0.383	0.291
Ce	0.496	0.219	0.489	0.578	0.516	0.580	0.285	0.539	0.622	0.485
Cu	0.848	0.071	0.634	0.751	0.997	0.882	0.370	0.916	1.166	0.856

Ir	1.857	0.352	1.616	1.296	2.186	1.728	0.856	1.866	2.246	1.578
Ni	1.210	-0.007	1.150	1.088	1.383	1.262	0.512	1.327	1.668	1.161
Pb	0.242	0.067	0.221	0.224	0.281	0.243	0.062	0.229	0.313	0.243
Pd	0.886	0.072	0.682	0.718	1.003	0.898	0.319	0.950	1.189	0.852
Pt	0.864	0.176	0.675	0.616	1.094	0.889	0.279	0.885	1.165	0.795
Rh	1.552	0.082	1.250	1.172	1.680	1.447	0.655	1.541	1.854	1.311
Sr	0.187	-0.010	0.159	0.199	0.234	0.237	0.088	0.240	0.310	0.225
Th	0.684	0.175	0.662	0.775	0.758	0.823	0.385	0.817	0.941	0.770
Yb	0.243	0.003	0.198	0.257	0.301	0.302	0.130	0.310	0.397	0.294

Table B.5: Grain boundary energies (J/m^2) of hcp elements

	Be	Cd	Co	Dy	Er	Gd	Hf	Ho	La
Σ7(0001)	1.121	0.103	0.722	0.264	0.318	0.201	0.411	0.297	0.139
	Lu	Mg	Nd	Os	Pm	Pr	Re	Ru	Sc
Σ7(0001)	0.342	0.2	0.208	1.578	0.217	0.195	0.97	1.119	0.294
	Sm	Tb	Tc	Ti	Tl	Tm	Y	Zn	Zr
Σ7(0001)	0.227	0.242	0.671	0.365	0.074	0.328	0.216	0.094	0.314

Table B.6: Work of separation (W_{sep} (J/m^2)) of cubic elements

sigma	Σ3	Σ3	Σ3	Σ5	Σ5	Σ5	Σ7	Σ7	Σ9	Σ9
plane	(011)	(111)	(112)	(001)	(012)	(013)	(111)	(123)	(011)	(122)
Ag	1.187	1.476	1.309	1.201	1.204	1.229	1.337	1.179	1.023	1.142
Al	1.498	1.595	1.649	1.447	1.498	1.512	1.456	1.427	1.242	1.466
Au	1.197	1.458	1.305	1.399	1.291	1.365	1.309	1.255	1.048	1.167
Ba	0.578	0.592	0.721	0.364	0.535	0.534	0.519	0.582	0.526	0.559
Ca	0.844	0.904	0.887	0.654	0.793	0.765	0.813	0.783	0.701	0.819
Ce	1.763	1.817	1.789	1.687	1.906	1.789	1.751	1.817	1.636	1.737
Cr	5.727	4.890	6.402	4.619	4.884	5.069	4.536	4.994	5.225	4.424
Cs	0.123	0.144	0.140	0.124	0.131	0.120	0.150	0.139	0.124	0.131
Cu	2.274	2.557	2.618	2.184	2.197	2.296	2.259	2.241	1.956	2.100
Fe	4.386	3.862	4.794	2.756	3.241	5.308	3.556	3.846	3.924	3.557
Ir	3.802	4.217	3.802	4.339	3.888	4.310	3.712	3.848	3.413	3.595
K	0.185	0.176	0.228	0.155	0.181	0.162	0.207	0.180	0.193	0.183
Li	0.951	0.916	1.023	0.651	0.861	0.839	0.874	0.927	0.915	0.835
Mo	5.092	4.181	6.318	3.931	4.170	4.448	3.715	4.252	4.555	4.066
Na	0.374	0.378	0.495	0.298	0.376	0.338	0.359	0.389	0.363	0.353
Nb	3.854	3.392	4.439	3.059	3.248	3.366	3.335	3.540	3.550	3.347
Ni	3.362	3.854	3.321	3.329	3.410	3.531	3.335	3.309	2.904	3.185
Pb	0.421	0.439	0.382	0.345	0.426	0.452	0.444	0.411	0.350	0.341
Pd	2.262	2.605	2.545	2.333	2.249	2.370	2.357	2.222	1.959	2.141
Pt	2.878	2.782	2.851	3.067	2.680	2.866	2.678	2.652	2.577	2.404
Rb	0.164	0.161	0.187	0.129	0.149	0.135	0.184	0.164	0.157	0.151
Rh	3.109	3.896	3.370	3.480	3.318	3.541	3.324	3.272	2.807	3.138

Sr	0.628	0.695	0.658	0.494	0.590	0.569	0.597	0.574	0.505	0.543
Ta	4.350	3.875	5.050	3.016	3.643	3.649	3.842	3.986	3.952	3.751
Th	1.809	1.896	1.715	1.487	1.883	1.877	1.685	1.702	1.552	1.638
Ac	1.011	1.235	1.078	0.927	1.15	1.061	1.088	1.039	0.894	0.993
V	4.521	4.225	5.131	3.379	3.816	3.678	4.146	4.352	4.232	4.089
W	5.743	4.689	6.123	4.703	4.694	5.219	4.065	4.595	5.057	4.343
Yb	0.778	0.899	0.803	0.608	0.717	0.701	0.772	0.711	0.624	0.675

Table B.7: Work of separation (W_{sep} (J/m^2)) of hcp elements

	Be	Cd	Co	Dy	Er	Gd	Hf	Ho	La
Σ7(0001)	2.46	0.296	3.493	1.714	1.79	1.481	3.007	1.751	1.252
	Lu	Mg	Nd	Os	Pm	Pr	Re	Ru	Sc
Σ7(0001)	1.911	0.89	1.43	4.262	1.519	1.373	4.192	4.035	2.24
	Sm	Tb	Tc	Ti	Tl	Tm	Y	Zn	Zr
Σ7(0001)	1.557	1.672	3.797	3.566	0.437	1.833	1.793	0.601	2.907

Table B.8: The comparison between the DFT calculated GB energies and the corresponding GB energies from references (in units of J/m^2).

	element	GB type	This work γ_{GB}	Ref γ_{GB}	functional	ref.
1	Al	Σ 3[1 1 0] (112)	0.31	0.43	LDA	[120]
2	Al	Σ5[1 0 0] (012)	0.53	0.46	LDA	[121]

	element	GB type	This work γ_{GB}	Ref γ_{GB}	functional	ref.
3	Al	Σ5[1 0 0] (012)	0.53	0.47	GGA	[122]
4	Al	Σ5[1 0 0] (012)	0.53	0.50	GGA-PBE	[123]
5	Al	Σ5[1 0 0] (012)	0.53	0.50	LDA	[124]
6	Al	Σ5[1 0 0] (012)	0.53	0.53	GGA	[125]
7	Cr	Σ3[1 1 0] (111)	1.98	1.88	GGA	[126]
8	Cr	Σ5[1 0 0] (012)	2.19	2.52	GGA	[126]
9	Cu	Σ3[1 1 0] (111)	0.07	0.02	GGA-PBE	[101]
10	Cu	Σ3[1 1 0] (112)	0.63	0.57	GGA-PBE	[101]
11	Cu	Σ3[1 1 0] (112)	0.63	0.64	GGA-PBE	[127]
12	Cu	Σ3[1 1 0] (112)	0.63	0.91	GGA-PBE	[127]
13	Cu	Σ5[1 0 0] (012)	1.00	0.90	GGA-PBE	[127]
14	Cu	Σ5[1 0 0] (012)	1.00	0.92	GGA-PBE	[128]
15	Cu	Σ5[1 0 0] (012)	1.00	0.92	GGA-PBE	[101]
16	Cu	Σ5[1 0 0] (013)	0.88	1.07	LDA	[129]
17	Cu	Σ5[1 0 0] (013)	0.88	0.83	GGA	[130]
18	Cu	Σ5[1 0 0] (013)	0.88	0.88	GGA-PBE	[131]
19	Cu	Σ5[1 0 0] (013)	0.88	0.88	FLAPW-GGA	[127]
20	Cu	Σ9[1 1 0] (221)	0.86	0.81	GGA-PBE	[127]
21	Cu	Σ9[1 1 0] (221)	0.86	1.15	GGA-PBE	[127]
22	Fe	Σ5[1 0 0] (013)	1.56	1.57	GGA-PBE	[100]
23	Fe	Σ3[1 1 0] (110)	0.51	0.52	GGA-PBE	[100]
24	Fe	Σ3[1 1 0] (111)	1.60	1.48	PAW-GGA	[132]
25	Fe	Σ3[1 1 0] (111)	1.60	1.52	GGA	[116]
26	Fe	Σ3[1 1 0] (111)	1.60	1.52	PAW-GGA	[133]

	element	GB type	This work γ_{GB}	Ref γ_{GB}	functional	ref.
27	Fe	Σ3[1 1 0] (111)	1.60	1.57	GGA-PBE	[100]
28	Fe	Σ3[1 1 0] (111)	1.60	1.57	GGA-PW91	[115]
29	Fe	Σ3[1 1 0] (111)	1.60	1.57	PAW-GGA	[134]
30	Fe	Σ3[1 1 0] (111)	1.60	1.61	GGA-PBE	[114]
31	Fe	Σ3[1 1 0] (111)	1.60	1.78	PBEsol	[99]
32	Fe	Σ3[1 1 0] (112)	0.42	0.34	GGA	[116]
33	Fe	Σ3[1 1 0] (112)	0.42	0.45	GGA-PBE	[100]
34	Fe	Σ3[1 1 0] (112)	0.42	0.45	PBE	[135]
35	Fe	Σ3[1 1 0] (112)	0.42	0.47	GGA-PW91	[117]
36	Fe	Σ3[1 1 0] (112)	0.42	0.51	PBEsol	[99]
37	Fe	Σ5[1 0 0] (012)	1.89	1.64	GGA-PBE	[100]
38	Fe	Σ5[1 0 0] (012)	1.89	2.00	GGA-PW91	[115]
39	Fe	Σ5[1 0 0] (100)	2.24	2.12	GGA-PBE	[100]
40	Fe	Σ5[1 0 0] (013)	1.56	0.83	PBE	[135]
41	Fe	Σ5[1 0 0] (013)	1.56	1.49	GGA	[116]
42	Fe	Σ5[1 0 0] (013)	1.56	1.51	PAW-GGA	[142]
43	Fe	Σ5[1 0 0] (013)	1.56	1.53	GGA-PW91	[117]
44	Fe	Σ5[1 0 0] (013)	1.56	1.63	GGA-PBE	[118]
45	Fe	Σ5[1 0 0] (013)	1.56	1.67	PBEsol	[99]
46	Fe	Σ7[1 1 1] (123)	1.42	1.46	GGA-PBE	[100]
47	Fe	Σ7[1 1 1] (123)	1.42	1.63	PBEsol	[99]
48	Fe	Σ9[1 1 0] (221)	1.75	1.66	GGA-PBE	[100]
49	Mo	Σ3[1 1 0] (111)	1.74	1.93	PBEsol	[99]
50	Mo	Σ3[1 1 0] (112)	0.48	0.54	PBEsol	[99]

	element	GB type	This work γ_{GB}	Ref γ_{GB}	functional	ref.
51	Mo	Σ5[1 0 0] (013)	1.73	1.52	GGA	[136]
52	Mo	Σ5[1 0 0] (013)	1.73	1.70	LDFT	[119]
53	Mo	Σ5[1 0 0] (013)	1.73	1.81	LDA	[137]
54	Mo	Σ5[1 0 0] (013)	1.73	1.81	PBEsol	[99]
55	Mo	Σ5[1 0 0] (013)	1.73	1.83	GGA-PBE	[138]
56	Mo	Σ5[100] (100)	2.43	2.43	GGA-PBE	[138]
57	Mo	Σ7[1 1 1] (123)	1.73	1.89	PBEsol	[99]
58	Nb	Σ5[1 0 0] (013)	1.20	1.29	LDFT	[119]
59	Ni	Σ3[1 1 0] (111)	-0.01	0.04	GGA-PBE	[101]
60	Ni	Σ3[1 1 0] (112)	1.15	0.84	GGA-PBE	[101]
61	Ni	Σ5[1 0 0] (012)	1.38	1.17	GGA-PBE	[140]
62	Ni	Σ5[1 0 0] (012)	1.38	1.23	GGA-PBE	[101]
63	Ni	Σ5[1 0 0] (012)	1.38	1.23	NCP	[141]
64	Ni	Σ5[1 0 0] (012)	1.38	1.23	PAW	[143]
65	Ni	Σ5[1 0 0] (012)	1.38	1.23	PAW-GGA	[143]
66	Ni	Σ5[1 0 0] (012)	1.38	1.33	PAW	[132]
67	Ni	Σ5[1 0 0] (012)	1.38	1.41	FLAPW-tGGA	[144]
68	Ni	Σ5[1 0 0] (012)	1.38	1.43	FLAPW-GGA	[139]
69	Ta	Σ5[1 0 0] (013)	1.44	1.54	LDFT	[119]
70	V	Σ3[1 1 0] (111)	1.25	0.96	PAW-GGA	[145]
71	W	Σ3[1 1 0] (1 1 2)	0.66	0.73	PAW-GGA	[146]
72	W	Σ3[1 1 0] (111)	2.24	2.10	PBEsol	[147]
73	W	Σ3[1 1 0] (111)	2.24	2.29	PAW-GGA	[148]
74	W	Σ3[1 1 0] (111)	2.24	2.44	PBEsol	[99]

	element	GB type	This work γ_{GB}	Ref γ_{GB}	functional	ref.
75	W	Σ3[1 1 0] (112)	0.66	0.65	PBEsol	[147]
76	W	Σ3[1 1 0] (112)	0.66	0.70	PAW-GGA	[148]
77	W	Σ3[1 1 0] (112)	0.67	0.66	PBEsol	[99]
78	W	Σ5[1 0 0] (012)	2.65	3.12	PAW-GGA	[148]
79	W	Σ5[1 0 0] (013)	2.20	2.23	PAW-GGA	[148]
80	W	Σ5[1 0 0] (013)	2.20	2.24	LDFT	[119]
81	W	Σ5[1 0 0] (013)	2.20	2.27	PBEsol	[99]
82	W	Σ7[1 1 1] (123)	2.33	2.37	PBEsol	[99]
83	W	Σ7[1 1 1] (123)	2.33	2.52	PAW-GGA	[148]
84	hcp-Zr	Σ7(0001)[0001]	0.31	0.29	GGA-PBE	[149]

Table B.9: Materials project mp-ids of all elements included in this work

Ac	Ag	Al	Au	Ba	Be
mp-10018	mp-124	mp-134	mp-81	mp-122	mp-87
Ca	Cd	Ce	Co	Cr	Cs
mp-45	mp-94	mp-28	mp-54	mp-90	mp-1
Cu	Dy	Er	Eu	Fe	Gd
mp-30	mp-88	mp-99	mp-20071	mp-13	mp-155
Hf	Hg	Ho	Ir	K	La
mp-103	mp-1184554	mp-144	mp-101	mp-58	mp-26
Li	Lu	Mg	Mo	Na	Nb
mp-135	mp-145	mp-153	mp-129	mp-127	mp-75
Nd	Ni	Os	Pb	Pd	Pm

mp-123	mp-23	mp-49	mp-20483	mp-2	mp-867200
Pr	Pt	Rb	Re	Rh	Ru
mp-38	mp-126	mp-70	mp-8	mp-74	mp-33
Sc	Sm	Sr	Ta	Tb	Tc
mp-67	mp-69	mp-76	mp-50	mp-18	mp-113
Th	Ti	Tl	Tm	V	W
mp-37	mp-46	mp-82	mp-143	mp-146	mp-91
Y	Yb	Zn	Zr		
mp-112	mp-162	mp-79	mp-131		

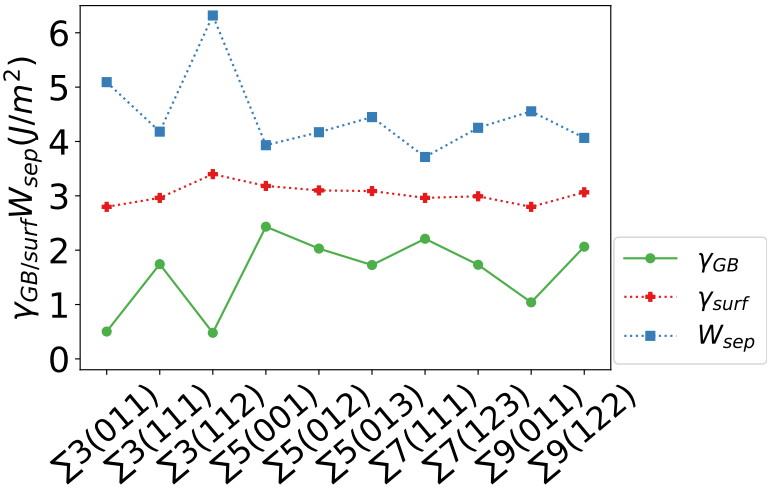

(a) bcc Mo

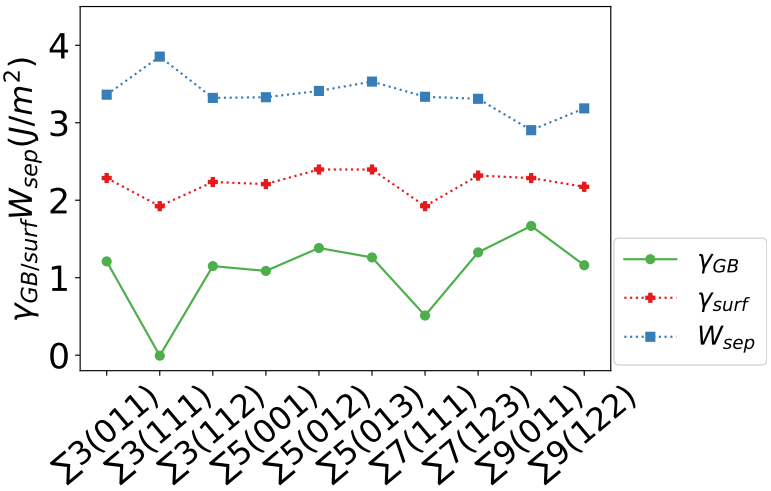

(b) fcc Cu

Figure B.5: The γ_{surf} varies moderately across different surfaces while the γ_{GB} varies dramatically across different GB types. This causes the near-linear relationship between γ_{GB} and W_{sep} as shown in Figure B.6.

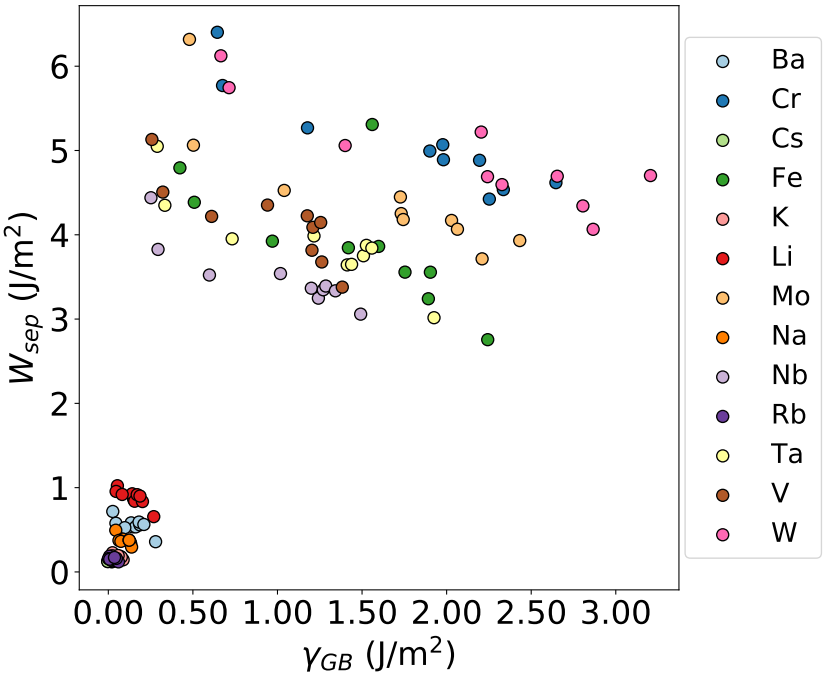

(a) bcc elements

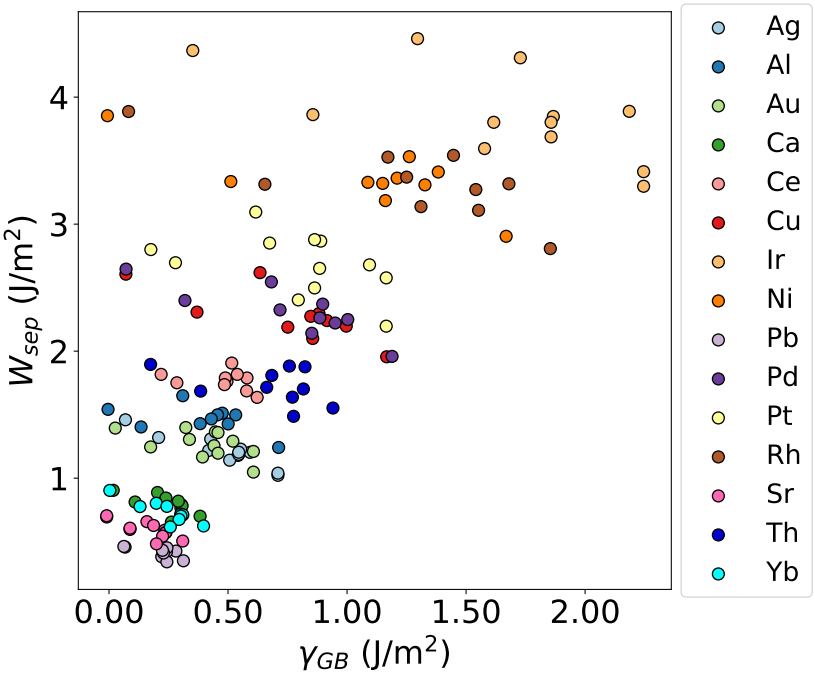

(b) fcc Cu

Figure B.6: The near linear trend between work of separation and GB energy. Each color represents one type of element. We observe a negative correlation between the value of W_{sep} and γ_{GB} for each element.

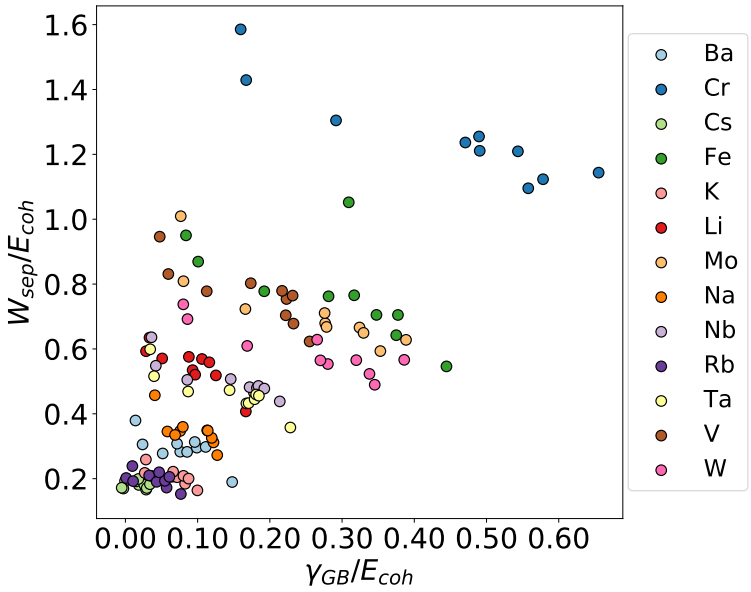

(a) bcc elements

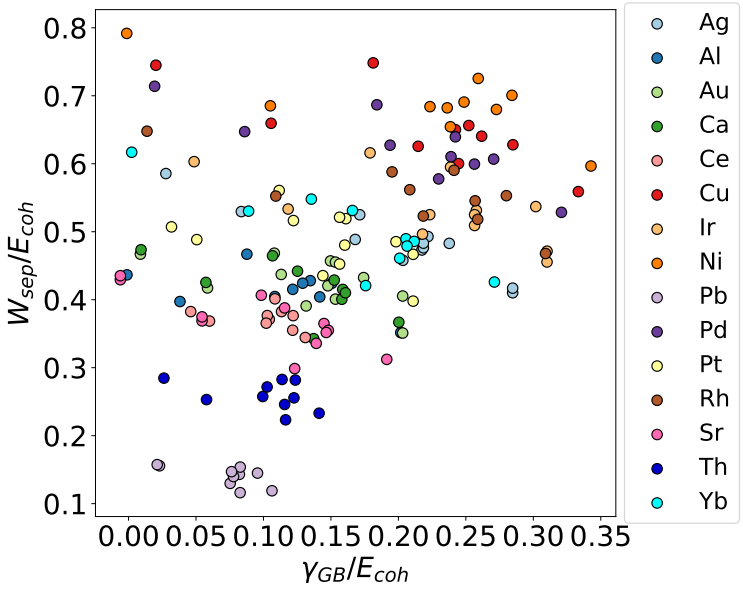

(b) fcc Cu

Figure B.7: The comparison between normalized GB energy and work of separation (both normalized by cohesive energy). The negative correlation between normalized γ_{GB} and W_{sep} of each element is observable.

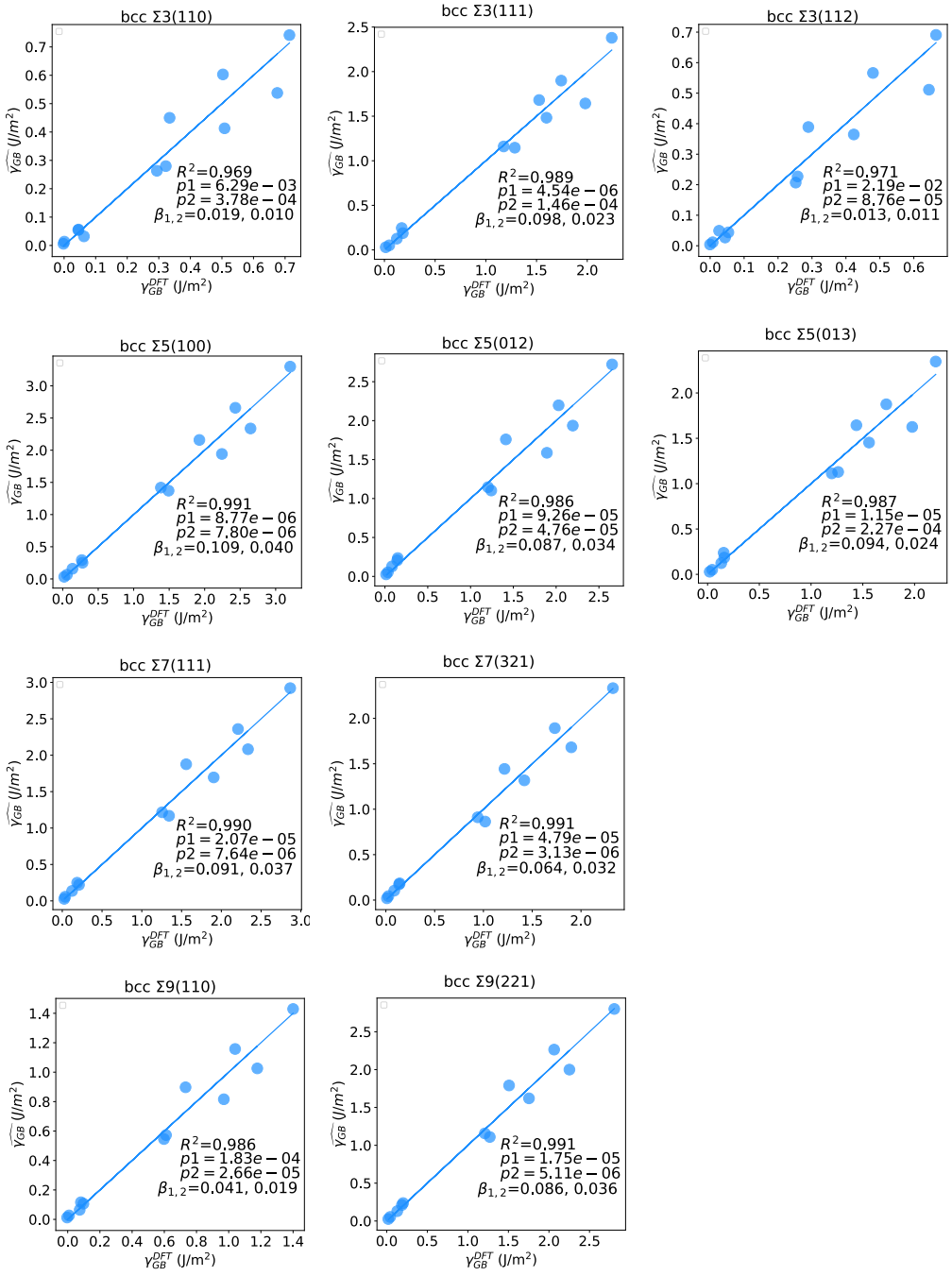

Figure B.8: Linear fitting for all GB types of bcc elements with $\gamma_{GB} = \beta_1 E_{coh} a_0^{-2} + \beta_2 G \cdot a_0$.

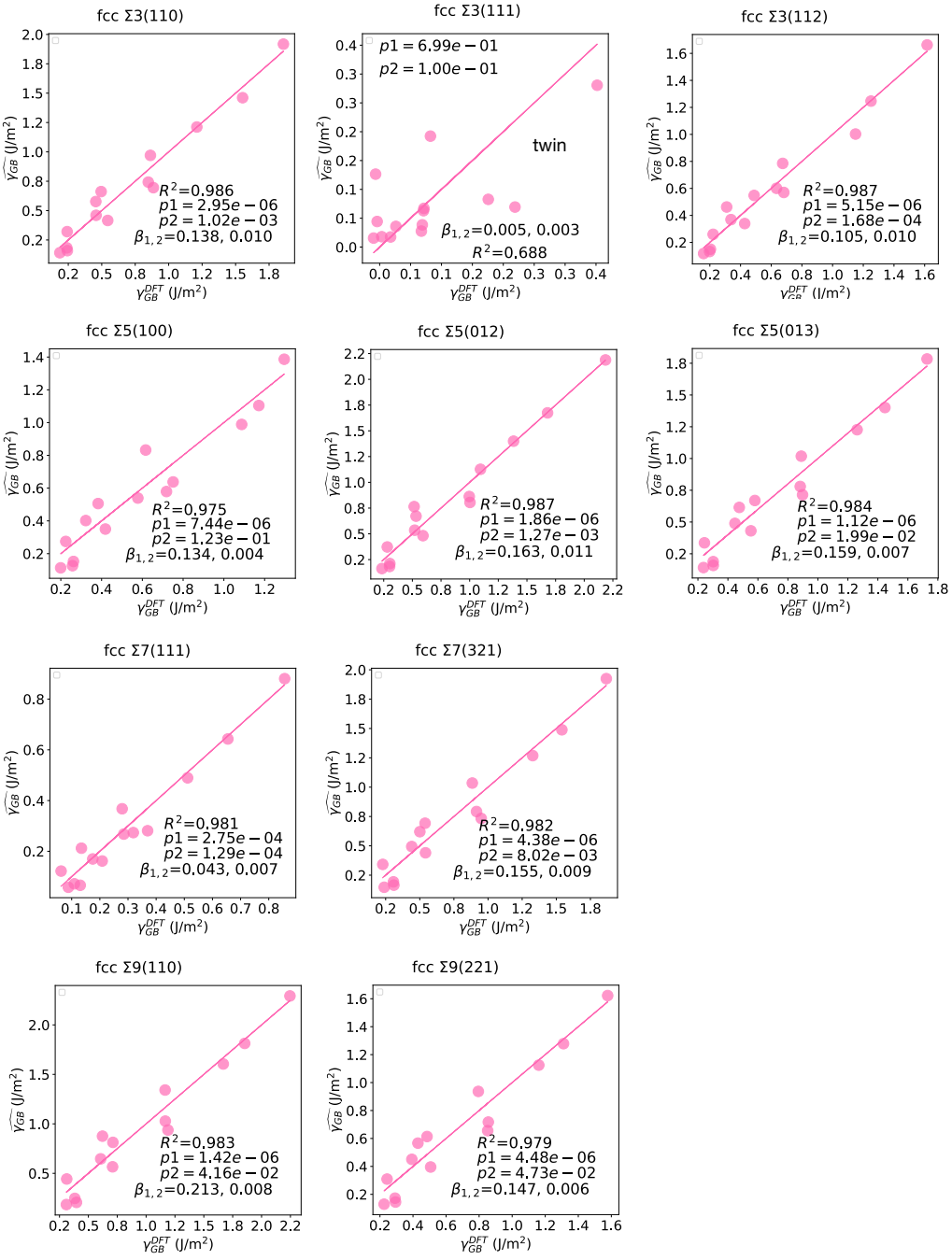

Figure B.9: Linear fitting for all GB types of fcc elements with $\gamma_{GB} = \beta_1 E_{coh} a_0^{-2} + \beta_2 G \cdot a_0$.

Bibliography

[1] David L. Olmsted, Stephen M. Foiles, and Elizabeth A. Holm. Survey of computed grain boundary properties in face-centered cubic metals: I. Grain boundary energy. *Acta Materialia*, 57(13):3694–3703, aug 2009. ISSN 13596454. doi: 10.1016/j.actamat.2009.04.007.

[2] Sutatch Ratanaphan, David L. Olmsted, Vasily V. Bulatov, Elizabeth A. Holm, Anthony D. Rollett, and Gregory S. Rohrer. Grain boundary energies in body-centered cubic metals. *Acta Materialia*, 88:346–354, 2015. ISSN 13596454. doi: 10.1016/j.actamat.2015.01.069.

[3] Chi Chen, Zhi Deng, Richard Tran, Hanmei Tang, Iek-heng Chu, and Shyue Ping Ong. Accurate force field for molybdenum by machine learning large materials data. *Physical Review Materials*, 1(4):043603, sep 2017. ISSN 2475-9953. doi: 10.1103/PhysRevMaterials.1.043603.

[4] Xiang-Guo Li, Chongze Hu, Chi Chen, Zhi Deng, Jian Luo, and Shyue Ping Ong. Quantum-accurate spectral neighbor analysis potential models for Ni-Mo binary alloys and fcc metals. *Phys. Rev. B*, 98(9):94104, sep 2018. doi: 10.1103/PhysRevB.98.094104.

[5] Hossein Beladi and Gregory S. Rohrer. The Distribution of Grain Boundary Planes in Interstitial Free Steel. *Metallurgical and Materials Transactions A*, 44(1):115–124, jan 2013. ISSN 1073-5623. doi: 10.1007/s11661-012-1393-0.

[6] David M. Saylor, Bassem S. El Dasher, Anthony D. Rollett, and Gregory S. Rohrer. Distribution of grain boundaries in aluminum as a function of five macroscopic parameters. *Acta Materialia*, 52(12):3649–3655, 2004. ISSN 13596454. doi: 10.1016/j.actamat.2004.04.018.

[7] Jia Li, Shen J. Dillon, and Gregory S. Rohrer. Relative grain boundary area and energy distributions in nickel. *Acta Materialia*, 57(14):4304–4311, aug 2009. ISSN 13596454. doi: 10.1016/j.actamat.2009.06.004.

[8] matweb. Material property data, 2019. Last accessed 14 April 2019.

[9] William D. Callister and David G. Rethwisch. *Materials Science and Engineering: An Introduction*. Wiley, Hoboken, NJ, 9th edition edition, 2014. ISBN 978-1-118-32457-8.

[10] Pavel Lejček. Grain boundaries: Description, structure and thermodynamics. In *Grain Boundary Segregation in Metals*, chapter 2, pages 5–24. Springer, Berlin, Heidelberg, 2010. ISBN 978-3-642-12505-8. doi: 10.1007/978-3-642-12505-8_2.

[11] Gerd Duscher, Matthew F. Chisholm, Uwe Alber, and Manfred Rühle. Bismuth-induced embrittlement of copper grain boundaries. *Nature Materials*, 3(9):621–626, September 2004. ISSN 1476-1122, 1476-4660. doi: 10.1038/nmat1191.

[12] Easo P. George, Dierk Raabe, and Robert O. Ritchie. High-entropy alloys. *Nature Reviews Materials*, 4(8):515–534, August 2019. ISSN 2058-8437. doi: 10.1038/s41578-019-0121-4.

[13] J.-W. Yeh, S.-K. Chen, S.-J. Lin, J.-Y. Gan, T.-S. Chin, T.-T. Shun, C.-H. Tsau, and S.-Y. Chang. Nanostructured High-Entropy Alloys with Multiple Principal Elements: Novel Alloy Design Concepts and Outcomes. *Advanced Engineering Materials*, 6(5):299–303, May 2004. ISSN 1438-1656, 1527-2648. doi: 10.1002/adem.200300567.

[14] W. Kohn and L. J. Sham. Self-consistent equations including exchange and correlation effects. *Physical Review*, 140(4A), 1965. ISSN 0031899X. doi: 10.1103/PhysRev.140.A1133.

[15] Y. Suzuki, T. Sekino, and K. Niihara. Effects of ZrO2 addition on microstructure and mechanical properties of MoSi2. *Scripta Metallurgica et Materialia*, 33(1):69–74, jul 1995. doi: 10.1016/0956-716x(95)00093-b.

[16] Z. Yao, J. Stiglich, and T.S. Sudarshan. Molybdenum silicide based materials and their properties. *Journal of Materials Engineering and Performance*, 8(3):291–304, jun 1999. doi: 10.1361/105994999770346837.

[17] T.C. Chou and T.G. Nieh. Kinetics of MoSi2 pest during low-temperature oxidation. *J. Mater. Res.*, 8(7):1605–1610, jul 1993. doi: 10.1557/jmr.1993.1605.

[18] T. C. Chou and T. G. Nieh. Pesting of the high-temperature intermetallic MoSi2. *JOM*, 45(12):15–21, dec 1993. doi: 10.1007/bf03222509.

[19] J. H. Schneibel, P. F. Tortorelli, R. O. Ritchie, and J. J. Kruzic. Optimization of mo-si-b intermetallic alloys. *Metall and Mat Trans A*, 36(3):525–531, mar 2005. doi: 10.1007/s11661-005-0166-4.

[20] J. A. Lemberg and R. O. Ritchie. Mo-si-b alloys for ultrahigh-temperature structural applications. *Adv. Mater.*, 24(26):3445–3480, jun 2012. doi: 10.1002/adma.201200764.

[21] M.K Miller, E.A Kenik, M.S Mousa, K.F Russell, and A.J Bryhan. Improvement in the ductility of molybdenum alloys due to grain boundary segregation. *Scripta Materialia*, 46(4):299–303, feb 2002. doi: 10.1016/s1359-6462(01)01242-8.

[22] M.K Miller and A.J Bryhan. Effect of zr, b and c additions on the ductility of molybdenum. *Materials Science and Engineering: A*, 327(1):80–83, apr 2002. doi: 10.1016/s0921-5093(01)01880-9.

[23] H. Saage, M. Krüger, D. Sturm, M. Heilmaier, J.H. Schneibel, E. George, L. Heatherly, Ch. Somsen, G. Eggeler, and Y. Yang. Ductilization of mo–si solid solutions manufactured by powder metallurgy. *Acta Materialia*, 57(13):3895–3901, aug 2009. doi: 10.1016/j.actamat.2009.04.040.

[24] A. Kumar and Brian Leonard Eyre. Grain boundary segregation and intergranular fracture in molybdenum. *Proc. R. Soc. Lond. A*, 370(1743):431–458, apr 1980. doi: 10.1098/rspa.1980.0043.

[25] P. Peralta, S.A. Maloy, F. Chu, J.J. Petrovic, and T.E. Mitchell. Mechanical properties of monocrystalline c11b MoSi2 with small aluminum additions. *Scripta Materialia*, 37(10):1599–1604, nov 1997. doi: 10.1016/s1359-6462(97)00280-7.

[26] U V Waghmare, Efthimios Kaxiras, V V Bulatov, and M S Duesbery. Effects of alloying on the ductility of MoSi2single crystals from first-principles calculations. *Modelling Simul. Mater. Sci. Eng.*, 6(4):493–506, jul 1998. doi: 10.1088/0965-0393/6/4/013.

[27] A.A Sharif, A Misra, J.J Petrovic, and T.E Mitchell. Solid solution hardening and softening in MoSi2 alloys. *Scripta Materialia*, 44(6):879–884, apr 2001. doi: 10.1016/s1359-6462(00)00698-9.

[28] A.A. Sharif, A. Misra, J.J. Petrovic, and T.E. Mitchell. Alloying of MoSi2 for improved mechanical properties. *Intermetallics*, 9(10-11):869–873, oct 2001. doi: 10.1016/s0966-9795(01)00084-x.

[29] Hai Hu, Xiaozhi Wu, Rui Wang, Weiguo Li, and Qing Liu. First principles study on the phase stability and mechanical properties of MoSi2 alloyed with al, mg and ge. *Intermetallics*, 67:26–34, dec 2015. doi: 10.1016/j.intermet.2015.07.008.

[30] M. Krüger, D. Schliephake, P. Jain, K. S. Kumar, G. Schumacher, and M. Heilmaier. Effects of zr additions on the microstructure and the mechanical behavior of PM mo-si-b alloys. *JOM*, 65(2):301–306, nov 2012. doi: 10.1007/s11837-012-0475-1.

[31] J.J Petrovic. Toughening strategies for MoSi2-based high temperature structural silicides. *Intermetallics*, 8(9-11):1175–1182, sep 2000. doi: 10.1016/s0966-9795(00)00044-3.

[32] Clint B. Geller, Richard W. Smith, John E. Hack, Paul Saxe, and Erich Wimmer. A computational search for ductilizing additives to mo. *Scripta Materialia*, 52(3):205–210, feb 2005. doi: 10.1016/j.scriptamat.2004.09.034.

[33] S.P. Sun, X.P. Li, Y. Zhang, H.J. Wang, Y. Yu, Y. Jiang, and D.Q. Yi. Prediction of the mechanical properties of MoSi 2 doped with cr, nb and w from first-principles calculations.

Journal of Alloys and Compounds, 714:459–466, aug 2017. doi: 10.1016/j.jallcom.2017.04.271.

[34] R. Gibala, A.K. Ghosh, D.C. Van Aken, D.J. Srolovitz, A. Basu, H. Chang, D.P. Mason, and W. Yang. Mechanical behavior and interface design of MoSi2-based alloys and composites. *Materials Science and Engineering: A*, 155(1-2):147–158, jun 1992. doi: 10.1016/0921-5093(92)90322-r.

[35] G. Liu, G. J. Zhang, F. Jiang, X. D. Ding, Y. J. Sun, J. Sun, and E. Ma. Nanostructured high-strength molybdenum alloys with unprecedented tensile ductility. *Nature Mater*, 12 (4):344–350, jan 2013. doi: 10.1038/nmat3544.

[36] I.M. Gunter, J.H. Schneibel, and J.J. Kruzic. Ductility and fracture toughness of molybdenum with MgAl2o4 additions. *Materials Science and Engineering: A*, 458(1-2):275–280, jun 2007. doi: 10.1016/j.msea.2006.12.128.

[37] P. Jéhanno, M. Böning, H. Kestler, M. Heilmaier, H. Saage, and M. Krüger. Molybdenum alloys for high temperature applications in air. *Powder Metallurgy*, 51(2):99–102, jun 2008. doi: 10.1179/174329008x313379.

[38] Yoshikazu Suzuki, Peter E. D. Morgan, and Koichi Niihara. Improvement in mechanical properties of powder-processed MoSi2by the addition of sc2o3and y2o3. *J American Ceramic Society*, 81(12):3141–3149, dec 1998. doi: 10.1111/j.1151-2916.1998.tb02749.x.

[39] W. Mao. Kinetics of self-healing reaction in tbc with $MoSi_2$ based sacrificial particles. Master's thesis, https://repository.tudelft.nl/islandora/object/uuid:1327ad1b-4638-407b-a801-4baac7b23f27?collection=education, 2013.

[40] D.E. Jiang and Emily A. Carter. Prediction of strong adhesion at the MoSi2/fe interface. *Acta Materialia*, 53(17):4489–4496, oct 2005. doi: 10.1016/j.actamat.2005.06.001.

[41] K. A. Marino, B. Hinnemann, and E. A. Carter. Atomic-scale insight and design principles for turbine engine thermal barrier coatings from theory. *Proceedings of the National Academy of Sciences*, 108(14):5480–5487, mar 2011. doi: 10.1073/pnas.1102426108.

[42] A. Arya and Emily A. Carter. Structure, bonding, and adhesion at the ZrC(100)/fe(110) interface from first principles. *Surface Science*, 560(1-3):103–120, jul 2004. doi: 10.1016/j.susc.2004.04.022.

[43] O. Lenchuk, J. Rohrer, and K. Albe. Solubility of zirconium and silicon in molybdenum studied by first-principles calculations. *Scripta Materialia*, 97:1–4, mar 2015. doi: 10.1016/j.scriptamat.2014.10.007.

[44] Olena Lenchuk, Jochen Rohrer, and Karsten Albe. Atomistic modelling of zirconium and silicon segregation at twist and tilt grain boundaries in molybdenum. *J Mater Sci*, 51(4): 1873–1881, oct 2015. doi: 10.1007/s10853-015-9494-y.

[45] Olena Lenchuk, Jochen Rohrer, and Karsten Albe. Cohesive strength of zirconia/molybdenum interfaces and grain boundaries in molybdenum: A comparative study. *Acta Materialia*, 135:150–157, aug 2017. doi: 10.1016/j.actamat.2017.05.070.

[46] Richard Tran, Zihan Xu, Naixie Zhou, Balachandran Radhakrishnan, Jian Luo, and Shyue Ping Ong. Computational study of metallic dopant segregation and embrittlement at molybdenum grain boundaries. *Acta Materialia*, 117:91–99, sep 2016. doi: 10.1016/j.actamat.2016.07.005.

[47] Shyue Ping Ong, William Davidson Richards, Anubhav Jain, Geoffroy Hautier, Michael Kocher, Shreyas Cholia, Dan Gunter, Vincent L. Chevrier, Kristin A. Persson, and Gerbrand Ceder. Python materials genomics (pymatgen): A robust, open-source python library for materials analysis. *Computational Materials Science*, 68:314–319, feb 2013. doi: 10.1016/j.commatsci.2012.10.028.

[48] Shyue Ping Ong, Shreyas Cholia, Anubhav Jain, Miriam Brafman, Dan Gunter, Gerbrand Ceder, and Kristin A. Persson. The materials application programming interface (API): A simple, flexible and efficient API for materials data based on REpresentational state transfer (REST) principles. *Computational Materials Science*, 97:209–215, feb 2015. doi: 10.1016/j.commatsci.2014.10.037.

[49] Anubhav Jain, Shyue Ping Ong, Geoffroy Hautier, Wei Chen, William Davidson Richards, Stephen Dacek, Shreyas Cholia, Dan Gunter, David Skinner, Gerbrand Ceder, and Kristin A. Persson. Commentary: The materials project: A materials genome approach to accelerating materials innovation. *APL Materials*, 1(1):011002, jul 2013. doi: 10.1063/1.4812323.

[50] G. Kresse and J. Furthmüller. Efficient iterative schemes for ab initio total-energy calculations using a plane-wave basis set. *Physical Review B*, 54(16):11169–11186, oct 1996. ISSN 0163-1829. doi: 10.1103/PhysRevB.54.11169.

[51] P. E. Blöchl. Projector augmented-wave method. *Physical Review B*, 50(24):17953–17979, dec 1994. ISSN 0163-1829. doi: 10.1103/PhysRevB.50.17953.

[52] John P Perdew, Kieron Burke, and Matthias Ernzerhof. Generalized Gradient Approximation Made Simple. *Physical Review Letters*, 77(18):3865–3868, oct 1996. ISSN 0031-9007. doi: 10.1103/PhysRevLett.77.3865.

[53] Su-Huai Wei and S. B. Zhang. Chemical trends of defect formation and doping limit in II-VI semiconductors: The case of CdTe. *Physical Review B*, 66(15):155211, October 2002. ISSN 0163-1829, 1095-3795. doi: 10.1103/PhysRevB.66.155211.

[54] Lei Wang, Thomas Maxisch, and Gerbrand Ceder. Oxidation energies of transition metal oxides within the gga+u framework. *Phys. Rev. B*, 73(19), may 2006. doi: 10.1103/physrevb.73.195107.

[55] A. Brokman and R.W. Balluffi. Coincidence lattice model for the structure and energy of grain boundaries. *Acta Metallurgica*, 29(10):1703–1719, oct 1981. doi: 10.1016/0001-6160(81)90005-5.

[56] L. Shaw and R. Abbaschian. Chemical states of the molybdenum disilicide (MoSi2) surface. *JOURNAL OF MATERIALS SCIENCE*, 30(20):5272–5280, oct 1995. doi: 10.1007/bf00356081.

[57] C. Bradford Barber, David P. Dobkin, and Hannu Huhdanpaa. The quickhull algorithm for convex hulls. *ACM Transactions on Mathematical Software*, 22(4):469–483, dec 1996. doi: 10.1145/235815.235821.

[58] K. Coleman F. Garzarolli, R. Adamson. Microstructure of zirconium alloys and effects on performance. *Advanced Nuclear Technology International Europe AB*, nov 2015.

[59] Dennis M. Dimiduk and John H. Perepezko. Mo-si-b alloys: Developing a revolutionary turbine-engine material. *MRS Bulletin*, 28(9):639–645, sep 2003. doi: 10.1557/mrs2003.191.

[60] Rui Li, Guojun Zhang, Bin Li, Xuan Chen, Shuai Ren, Juan Wang, and Jun Sun. The multi-scale microstructure and strengthening mechanisms of Mo-12Si-8.5BxZr (at.%) alloys. *International Journal of Refractory Metals and Hard Materials*, 68:65–74, November 2017. ISSN 02634368. doi: 10.1016/j.ijrmhm.2017.06.007.

[61] Yoshikazu Suzuki, Peter E.D. Morgan, and Koichi Niihara. The improvement in mechanical properties of MoSi2 through in situ crystallization of grain boundary silica glass by the additions of refractory oxides. *Materials Science and Engineering: A*, 261(1-2):188–195, March 1999. ISSN 09215093. doi: 10.1016/S0921-5093(98)01065-X.

[62] S. Wagener. Getter materials for electron tubes. *Vacuum*, 1(2):128–133, apr 1951. doi: 10.1016/0042-207x(51)90066-8.

[63] Tadao Watanabe. The importance of grain boundary character distribution (GBCD) to recrystallization, grain growth and texture. *Scripta Metallurgica et Materialia*, 27(11):1497–1502, dec 1992. ISSN 0956716X. doi: 10.1016/0956-716X(92)90134-Z.

[64] Gregory S. Rohrer. Grain boundary energy anisotropy: a review. *Journal of Materials Science*, 46(18):5881–5895, sep 2011. ISSN 0022-2461. doi: 10.1007/s10853-011-5677-3.

[65] Tadao Watanabe. Grain boundary engineering: historical perspective and future prospects. *Journal of Materials Science*, 46(12):4095–4115, jun 2011. ISSN 1573-4803. doi: 10.1007/s10853-011-5393-z.

[66] Chongze Hu, Jingsong Huang, Bobby G Sumpter, Efstathios Meletis, and Traian Dumitrică. Ab Initio Predictions of Strong Interfaces in Transition-Metal Carbides and Nitrides for Superhard Nanocomposite Coating Applications. *ACS Applied Nano Materials*, 1(5):2029–2035, may 2018. doi: 10.1021/acsanm.8b00227.

[67] Tadao Watanabe and Sadahiro Tsurekawa. The control of brittleness and development of desirable mechanical properties in polycrystalline systems by grain boundary engineering. *Acta Materialia*, 47(15):4171–4185, 1999. ISSN 1359-6454. doi: https://doi.org/10.1016/S1359-6454(99)00275-X.

[68] Hui Zheng, Richard Tran, Xiang Guo Li, Balachandran Radhakrishnan, and Shyue Ping Ong. Role of Zr in strengthening MoSi2 from density functional theory calculations. *Acta Materialia*, 145:470–476, 2018. ISSN 13596454. doi: 10.1016/j.actamat.2017.12.017.

[69] E.M. Lehockey and G. Palumbo. On the creep behaviour of grain boundary engineered nickel 1. *Materials Science and Engineering: A*, 237(2):168–172, 1997. ISSN 09215093. doi: 10.1016/S0921-5093(97)00126-3.

[70] P. Shi, R. Hu, T. Zhang, L. Yuan, and J. Li. Grain boundary character distribution and its effect on corrosion of Ni–23Cr–16Mo superalloy. *Materials Science and Technology*, 33 (1):84–91, 2017. ISSN 0267-0836. doi: 10.1179/1743284715Y.0000000142.

[71] Shigeaki Kobayashi, Toshiyuki Inomata, Hiroyuki Kobayashi, Sadahiro Tsurekawa, and Tadao Watanabe. Effects of grain boundary- and triple junction-character on intergranular fatigue crack nucleation in polycrystalline aluminum. *Journal of Materials Science*, 43 (11):3792–3799, jun 2008. ISSN 1573-4803. doi: 10.1007/s10853-007-2236-z.

[72] E M Lehockey, G Palumbo, and P Lin. Improving the weldability and service performance of nickel-and iron-based superalloys by grain boundary engineering. *Metallurgical and Materials Transactions A*, 29(12):3069–3079, dec 1998. ISSN 1543-1940. doi: 10.1007/s11661-998-0214-y.

[73] G S Was. Grain-Boundary Chemistry and Intergranular Fracture in Austenitic Nickel-Base Alloys—A Review. *CORROSION*, 46(4):319–330, 1990. doi: 10.5006/1.3585110.

[74] Ulrich Krupp, William M Kane, Xinyu Liu, Olaf Dueber, Campbell Laird, and Charles J McMahon. The effect of grain-boundary-engineering-type processing on oxygen-induced cracking of IN718. *Materials Science and Engineering: A*, 349(1):213–217, 2003. ISSN 0921-5093. doi: https://doi.org/10.1016/S0921-5093(02)00753-0.

[75] André Pineau. Crossing grain boundaries in metals by slip bands, cleavage and fatigue cracks. *Philosophical Transactions of the Royal Society A: Mathematical, Physical and Engineering Sciences*, 373(2038):20140131, 2015. doi: 10.1098/rsta.2014.0131.

[76] G. S. Rohrer, J. Li, S. Lee, A. D. Rollett, M. Groeber, and M. D. Uchic. Deriving grain boundary character distributions and relative grain boundary energies from three-dimensional EBSD data. *Materials Science and Technology*, 26(6):661–669, 2010. ISSN 0267-0836. doi: 10.1179/026708309X12468927349370.

[77] Gregory S. Rohrer, Elizabeth A. Holm, Anthony D. Rollett, Stephen M. Foiles, Jia Li, and David L. Olmsted. Comparing calculated and measured grain boundary energies in nickel.

Acta Materialia, 58(15):5063–5069, 2010. ISSN 13596454. doi: 10.1016/j.actamat.2010.05.042.

[78] G Hasson, J.-Y. Boos, I Herbeuval, M Biscondi, and C Goux. Theoretical and experimental determinations of grain boundary structures and energies: Correlation with various experimental results. *Surface Science*, 31:115–137, 1972. ISSN 0039-6028. doi: https://doi.org/10.1016/0039-6028(72)90256-7.

[79] K Barmak, J Kim, C.-S. Kim, W E Archibald, G S Rohrer, A D Rollett, D Kinderlehrer, S Ta'asan, H Zhang, and D J Srolovitz. Grain boundary energy and grain growth in Al films: Comparison of experiments and simulations. *Scripta Materialia*, 54(6):1059–1063, 2006. ISSN 1359-6462. doi: https://doi.org/10.1016/j.scriptamat.2005.11.060.

[80] N.a A Gjostein and F.N N Rhines. Absolute interfacial energies of [001] tilt and twist grain boundaries in copper. *Acta Metallurgica*, 7(5):319–330, 1959. ISSN 0001-6160. doi: https://doi.org/10.1016/0001-6160(59)90198-1.

[81] M McLean. Grain-boundary energy of copper at 1030°C. *Journal of Materials Science*, 8(4):571–576, apr 1973. ISSN 1573-4803. doi: 10.1007/BF00550462.

[82] Siu Wai Chan and R. W. Balluffi. Study of energy vs misorientation for grain boundaries in gold by crystallite rotation method-II. Tilt boundaries and mixed boundaries. *Acta Metallurgica*, 34(11):2191–2199, 1986. ISSN 00016160. doi: 10.1016/0001-6160(86)90164-1.

[83] H Miura, M Kato, and T Mori. Temperature dependence of the energy of Cu [110] symmetrical tilt grain boundaries. *Journal of Materials Science Letters*, 13(1):46–48, jan 1994. ISSN 1573-4811. doi: 10.1007/BF02352916.

[84] Thomas Skidmore, Rudy G. Buchheit, and Mary C. Juhas. Grain boundary energy vs. misorientation in Inconel® 600 alloy as measured by thermal groove and OIM analysis correlation. *Scripta Materialia*, 50(6):873–877, 2004. ISSN 13596462. doi: 10.1016/j.scriptamat.2003.12.004.

[85] Gregory S. Rohrer. Measuring and interpreting the structure of grain-boundary networks. *Journal of the American Ceramic Society*, 94(3):633–646, 2011. ISSN 00027820. doi: 10.1111/j.1551-2916.2011.04384.x.

[86] Yaron Amouyal, Eugen Rabkin, and Yuri Mishin. Correlation between grain boundary energy and geometry in Ni-rich NiAl. *Acta Materialia*, 53(14):3795–3805, 2005. ISSN 13596454. doi: 10.1016/j.actamat.2005.04.043.

[87] Xuan Liu, Dooho Choi, Hossein Beladi, Noel T Nuhfer, Gregory S Rohrer, and Katayun Barmak. The five-parameter grain boundary character distribution of nanocrystalline tungsten. *Scripta Materialia*, 69(5):413–416, 2013. ISSN 1359-6462. doi: https://doi.org/10.1016/j.scriptamat.2013.05.046.

[88] Hossein Beladi and Gregory S Rohrer. The relative grain boundary area and energy distributions in a ferritic steel determined from three-dimensional electron backscatter diffraction maps. *Acta Materialia*, 61(4):1404–1412, 2013. ISSN 1359-6454. doi: https://doi.org/10.1016/j.actamat.2012.11.017.

[89] Hossein Beladi, Noel T Nuhfer, and Gregory S Rohrer. The five-parameter grain boundary character and energy distributions of a fully austenitic high-manganese steel using three dimensional data. *Acta Materialia*, 70:281–289, 2014. ISSN 1359-6454. doi: https://doi.org/10.1016/j.actamat.2014.02.038.

[90] Madeleine N. Kelly, Krzysztof Glowinski, Noel T. Nuhfer, and Gregory S. Rohrer. The five parameter grain boundary character distribution of α-Ti determined from three-dimensional orientation data. *Acta Materialia*, 111:22–30, 2016. ISSN 13596454. doi: 10.1016/j.actamat.2016.03.029.

[91] D. Wolf. Structure-energy correlation for grain boundaries in F.C.C. metals—I. Boundaries on the (111) and (100) planes. *Acta Metallurgica*, 37(7):1983–1993, 1989. ISSN 0001-6160. doi: https://doi.org/10.1016/0001-6160(89)90082-5.

[92] D Wolf and S Phillpot. Role of the densest lattice planes in the stability of crystalline interfaces: A computer simulation study. *Materials Science and Engineering: A*, A107: 3–14, 1989. ISSN 0921-5093. doi: https://doi.org/10.1016/0921-5093(89)90370-5.

[93] D. Wolf. Correlation between the energy and structure of grain boundaries in b.c.c. metals. II. Symmetrical tilt boundaries. *Philosophical Magazine A*, 62(4):447–464, 1990. ISSN 01418610. doi: 10.1080/01418619008244790.

[94] D. Wolf. A broken-bond model for grain boundaries in face-centered cubic metals. *Journal of Applied Physics*, 68(7):3221–3236, 1990. ISSN 00218979. doi: 10.1063/1.346373.

[95] D. Wolf. Structure-energy correlation for grain boundaries in F.C.C. metals-III. Symmetrical tilt boundaries. *Acta Metallurgica Et Materialia*, 38(5):781–790, 1990. ISSN 09567151. doi: 10.1016/0956-7151(90)90030-K.

[96] Elizabeth A. Holm, David L. Olmsted, and Stephen M. Foiles. Comparing grain boundary energies in face-centered cubic metals: Al, Au, Cu and Ni. *Scripta Materialia*, 63(9): 905–908, 2010. ISSN 13596462. doi: 10.1016/j.scriptamat.2010.06.040.

[97] Mark A. Tschopp, Shawn P. Coleman, and David L. McDowell. Symmetric and asymmetric tilt grain boundary structure and energy in Cu and Al (and transferability to other fcc metals). *Integrating Materials and Manufacturing Innovation*, 4(1):11, oct 2015. ISSN 2193-9764. doi: 10.1186/s40192-015-0040-1.

[98] Elizabeth A. Holm, Gregory S. Rohrer, Stephen M. Foiles, Anthony D. Rollett, Herbert M. Miller, and David L. Olmsted. Validating computed grain boundary energies in fcc metals using the grain boundary character distribution. *Acta Materialia*, 59(13):5250–5256, 2011. ISSN 13596454. doi: 10.1016/j.actamat.2011.05.001.

[99] Daniel Scheiber, Reinhard Pippan, Peter Puschnig, and Lorenz Romaner. Ab initio calculations of grain boundaries in bcc metals. *Modelling and Simulation in Materials Science and Engineering*, 24(3):035013, 2016. ISSN 1361651X. doi: 10.1088/0965-0393/24/3/035013.

[100] Jingliang Wang, Georg K.H. Madsen, and Ralf Drautz. Grain boundaries in bcc-Fe: A density-functional theory and tight-binding study. *Modelling and Simulation in Materials Science and Engineering*, 26(2), 2018. ISSN 1361651X. doi: 10.1088/1361-651X/aa9f81.

[101] Jonathan J Bean and Keith P McKenna. Origin of differences in the excess volume of copper and nickel grain boundaries. *Acta Materialia*, 110:246–257, 2016. ISSN 1359-6454. doi: https://doi.org/10.1016/j.actamat.2016.02.040.

[102] Shyue Ping Ong, William Davidson Richards, Anubhav Jain, Geoffroy Hautier, Michael Kocher, Shreyas Cholia, Dan Gunter, Vincent L. Chevrier, Kristin A. Persson, and Gerbrand Ceder. Python Materials Genomics (pymatgen): A robust, open-source python library for materials analysis. *Computational Materials Science*, 68:314–319, feb 2013. ISSN 0927-0256. doi: https://doi.org/10.1016/j.commatsci.2012.10.028.

[103] Shyue Ping Ong, Shreyas Cholia, Anubhav Jain, Miriam Brafman, Dan Gunter, Gerbrand Ceder, and Kristin A. Persson. The Materials Application Programming Interface (API): A simple, flexible and efficient API for materials data based on REpresentational State Transfer (REST) principles. *Computational Materials Science*, 97:209–215, 2015. ISSN 09270256. doi: 10.1016/j.commatsci.2014.10.037.

[104] H Grimmer. Coincidence-site lattices. *Acta Crystallographica Section A*, 32(5):783–785, sep 1976. ISSN 0567-7394. doi: 10.1107/S056773947601231X.

[105] Johannes J. Möller and Erik Bitzek. Fracture toughness and bond trapping of grain boundary cracks. *Acta Materialia*, 73:1–11, 2014. ISSN 1359-6454. doi: https://doi.org/10.1016/j.actamat.2014.03.035.

[106] Valerie R. Coffman and James P. Sethna. Grain boundary energies and cohesive strength as a function of geometry. *Physical Review B*, 77(14):144111, apr 2008. ISSN 10980121. doi: 10.1103/PhysRevB.77.144111.

[107] M Grujicic, H Zhao, and G L Krasko. Atomistic simulation of Σ3 (111) grain boundary fracture in tungsten containing various impurities. *International Journal of Refractory Metals and Hard Materials*, 15(5):341–355, 1997. ISSN 0263-4368. doi: https://doi.org/10.1016/S0263-4368(97)87508-7.

[108] Peter Gumbsch. Atomistic modelling of diffusion-controlled interfacial decohesion. *Materials Science and Engineering: A*, 260(1):72–79, 1999. ISSN 0921-5093. doi: https://doi.org/10.1016/S0921-5093(98)00984-8.

[109] Richard Tran, Zihan Xu, Balachandran Radhakrishnan, Donald Winston, Wenhao Sun, Kristin Aslaug Persson, and Shyue Ping Ong. Data Descripter: Surface energies of elemental crystals. *Scientific Data*, 3(160080):1–13, 2016. ISSN 0929-1903. doi: 10.1038/cgt.2016.38.

[110] Kiran Mathew, Joseph H Montoya, Alireza Faghaninia, Shyam Dwarakanath, Muratahan Aykol, Hanmei Tang, Iek-heng Chu, Tess Smidt, Brandon Bocklund, Matthew Horton, John Dagdelen, Brandon Wood, Zi-kui Liu, Jeffrey Neaton, Shyue Ping, Kristin Persson, Anubhav Jain, Shyue Ping Ong, Kristin Persson, Anubhav Jain, Shyue Ping, Kristin Persson, and Anubhav Jain. Atomate: A high-level interface to generate, execute, and analyze computational materials science workflows. *Computational Materials Science*, 139: 140–152, 2017. ISSN 0927-0256. doi: https://doi.org/10.1016/j.commatsci.2017.07.030.

[111] Anubhav Jain, Shyue Ping Ong, Wei Chen, Bharat Medasani, Xiaohui Qu, Michael Kocher, Miriam Brafman, Guido Petretto, Gian-Marco Rignanese, Geoffroy Hautier, Daniel Gunter, and Kristin A. Persson. FireWorks: a dynamic workflow system designed for high-throughput applications. *Concurrency and Computation: Practice and Experience*, 27(17):5037–5059, dec 2015. ISSN 15320626. doi: 10.1002/cpe.3505.

[112] Nicola Gaston, Dirk Andrae, Beate Paulus, Ulrich Wedig, and Martin Jansen. Understanding the hcp anisotropy in Cd and Zn: the role of electron correlation in determining the potential energy surface. *Phys. Chem. Chem. Phys.*, 12(3):681–687, 2010. ISSN 1463-9076. doi: 10.1039/B915967C.

[113] D. Wolf. Structure and energy of general grain boundaries in bcc metals. *Journal of Applied Physics*, 69(1):185–196, jan 1991. ISSN 00218979. doi: 10.1063/1.347741.

[114] Somesh Kr Bhattacharya, Shingo Tanaka, Yoshinori Shiihara, and Masanori Kohyama. Ab initio study of symmetrical tilt grain boundaries in bcc Fe: Structural units, magnetic moments, interfacial bonding, local energy and local stress. *Journal of Physics Condensed Matter*, 25(13), 2013. ISSN 09538984. doi: 10.1088/0953-8984/25/13/135004.

[115] E Wachowicz, T Ossowski, and A Kiejna. Cohesive and magnetic properties of grain boundaries in bcc Fe with Cr additions. *Phys. Rev. B*, 81(9):94104, mar 2010. doi: 10.1103/PhysRevB.81.094104.

[116] Ning Gao, Chu Chun Fu, M. Samaras, R. Schäublin, M. Victoria, and W. Hoffelner. Multiscale modelling of bi-crystal grain boundaries in bcc iron. *Journal of Nuclear Materials*, 385(2):262–267, 2009. ISSN 00223115. doi: 10.1016/j.jnucmat.2008.12.016.

[117] Yaojun A Du, Lars Ismer, Rogal Jutta, Tilmann Hickel, Jörg Neugebauer, and Ralf Drautz. First-principles study on the interaction of H interstitials with grain boundaries in α and γ-Fe. *Phys. Rev. B*, 84(14):144121, oct 2011. ISSN 03778282. doi: 10.1103/PhysRevB.84.144121.

[118] Miroslav Čák, Mojmír Šob, and Jürgen Hafner. First-principles study of magnetism at grain boundaries in iron and nickel. *Physical Review B - Condensed Matter and Materials Physics*, 78(5):1–10, 2008. ISSN 10980121. doi: 10.1103/PhysRevB.78.054418.

[119] T Ochs, O Beck, C Elsässer, and B Meyer. Symmetrical tilt grain boundaries in body-centred cubic transition metals: An ab initio local-density-functional study. *Philosophical Magazine A*, 80(2):351–372, 2000. doi: 10.1080/01418610008212057.

[120] Alan F. Wright and Susan R. Atlas. Density-functional calculations for grain boundaries in aluminum. *Phys. Rev. B*, 50(20):15248–15260, nov 1994. ISSN 01631829. doi: 10.1103/PhysRevB.50.15248.

[121] S. Ogata, H. Kitagawa, Y. Maegawa, and K. Saitoh. Ab-initio analysis of aluminum $\Sigma = 5$ grain boundaries — fundamental structures and effects of silicon impurity. *Computational Materials Science*, 7(3):271–278, 1997. ISSN 0927-0256. doi: https://doi.org/10.1016/S0927-0256(96)00095-X.

[122] Vsevolod I. Razumovskiy, A. V. Ruban, I. M. Razumovskii, A. Y. Lozovoi, V. N. Butrim, and Yu.Kh. Kh Vekilov. The effect of alloying elements on grain boundary and bulk cohesion in aluminum alloys: An ab initio study. *Scripta Materialia*, 65(10):926–929, 2011. ISSN 1359-6462. doi: https://doi.org/10.1016/j.scriptamat.2011.08.014.

[123] Shengjun Zhang, Oleg Y Kontsevoi, Arthur J Freeman, and Gregory B Olson. Sodium-induced embrittlement of an aluminum grain boundary. *Phys. Rev. B*, 82(22):224107, dec 2010. doi: 10.1103/PhysRevB.82.224107.

[124] Gang Lu and Nicholas Kioussis. Interaction of vacancies with a grain boundary in aluminum: A first-principles study. *Physical Review B - Condensed Matter and Materials Physics*, 64(2):1–7, jun 2001. ISSN 1550235X. doi: 10.1103/PhysRevB.64.024101.

[125] Vsevolod I. Razumovskiy, Igor M. Razumovskii, Andrei V. Ruban, V.N. Butrim, and Yu.Kh. Vekilov. The Influence of Alloying Elements on Grain Boundary and Bulk Cohesion in Aluminum Alloys: Ab Initio Study. *Advanced Materials Research THERMEC 2011 Supplement*, 409:417–422, nov 2011. ISSN 1662-8985. doi: 10.4028/www.scientific.net/AMR.409.417.

[126] T Ossowski, E Wachowicz, and A Kiejna. Effect of iron additions on intergranular cohesion in chromium. *Journal of Physics: Condensed Matter*, 21(48):485002, oct 2009. ISSN 09538984. doi: 10.1088/0953-8984/21/48/485002.

[127] Jian Xu, Jian-Bo Bo Liu, Shun-Ning Ning Li, Bai-Xin Xin Liu, and Yong Jiang. Self-healing properties of nanocrystalline materials: a first-principles analysis of the role of grain boundaries. *Phys. Chem. Chem. Phys.*, 18(27):17930–17940, 2016. ISSN 14639076. doi: 10.1039/C6CP02505F.

[128] Georg Schusteritsch, Thomas D. Kühne, Zheng Xiao Guo, and Efthimios Kaxiras. The effect of Ag, Pb and Bi impurities on grain boundary sliding and intergranular decohesion in Copper. *Philosophical Magazine*, 96(27):2868–2886, 2016. ISSN 14786443. doi: 10.1080/14786435.2016.1217360.

[129] A Y Lozovoi, A T Paxton, and M W Finnis. Structural and chemical embrittlement of grain boundaries by impurities: A general theory and first-principles calculations for copper. *Phys. Rev. B*, 74(15):155416, oct 2006. doi: 10.1103/PhysRevB.74.155416.

[130] Yue Cui and Huck Beng Chew. A simple numerical approach for reconstructing the atomic stresses at grain boundaries from quantum-mechanical calculations. *The Journal of Chemical Physics*, 150(14):144702, 2019. ISSN 00219606. doi: 10.1063/1.5085061.

[131] Zhifeng Huang, Fei Chen, Qiang Shen, Lianmeng Zhang, and Timothy J. Rupert. Uncovering the influence of common nonmetallic impurities on the stability and strength of a Σ5 (310) grain boundary in Cu. *Acta Materialia*, 148:110–122, 2018. ISSN 13596454. doi: 10.1016/j.actamat.2018.01.058.

[132] Masatake Yamaguchi, Motoyuki Shiga, and Hideo Kaburaki. Grain Boundary Decohesion by Sulfur Segregation in Ferromagnetic Iron and Nickel—A First-Principles Study—. *Materials Transactions*, 47(11):2682–2689, 2006. ISSN 1345-9678. doi: 10.2320/matertrans.47.2682.

[133] Masatake Yamaguchi. First-Principles Study on the Grain Boundary Embrittlement of Metals by Solute Segregation: Part I. Iron (Fe)-Solute (B, C, P, and S) Systems. *Metallurgical and Materials Transactions A*, 42(2):319–329, feb 2011. ISSN 1543-1940. doi: 10.1007/s11661-010-0381-5.

[134] Zhuo Xu, Shingo Tanaka, and Masanori Kohyama. Grain-boundary segregation of 3d-transition metal solutes in bcc Fe: ab initio local-energy and d-electron behavior analysis. *Journal of Physics: Condensed Matter*, 31(11):115001, jan 2019. doi: 10.1088/1361-648x/aafd00.

[135] Klaus-Dieter Dieter Bauer, Mira Todorova, Kurt Hingerl, and Jörg Neugebauer. A first principles investigation of zinc induced embrittlement at grain boundaries in bcc iron. *Acta Materialia*, 90:69–76, 2015. ISSN 1359-6454. doi: https://doi.org/10.1016/j.actamat.2015.02.018.

[136] A. M. Tahir, R. Janisch, and A. Hartmaier. Ab initio calculation of traction separation laws for a grain boundary in molybdenum with segregated C impurites. *Modelling and Simulation in Materials Science and Engineering*, 21(7):075005, 2013. ISSN 09650393. doi: 10.1088/0965-0393/21/7/075005.

[137] Rebecca Janisch and Christian Elsässer. Growth and mechanical properties of a MoC precipitate at a Mo grain boundary: An ab initio density functional theory study. *Phys. Rev. B*, 77(9):94118, mar 2008. doi: 10.1103/PhysRevB.77.094118.

[138] Richard Tran, Zihan Xu, Naixie Zhou, Balachandran Radhakrishnan, Jian Luo, and Shyue Ping Ong. Computational study of metallic dopant segregation and embrittlement at molybdenum grain boundaries. In *Acta Materialia*, volume 117, pages 91–99. Elsevier Ltd, 2016. doi: 10.1016/j.actamat.2016.07.005.

[139] Masatake Yamaguchi, Motoyuki Shiga, and Hideo Kaburaki. Energetics of segregation and embrittling potency for non-transition elements in the Ni Σ5 (012) symmetrical tilt grain boundary: a first-principles study. *Journal of Physics: Condensed Matter*, 16(23): 3933–3956, may 2004. ISSN 09538984. doi: 10.1088/0953-8984/16/23/013.

[140] V. I. Razumovskiy, A. Y. Lozovoi, and I. M. Razumovskii. First-principles-aided design of a new Ni-base superalloy: Influence of transition metal alloying elements on grain boundary and bulk cohesion. *Acta Materialia*, 82:369–377, 2015. ISSN 1359-6454. doi: https://doi.org/10.1016/j.actamat.2014.08.047.

[141] EL Tayeb Bentria, Ibn Khaldoun Lefkaier, and Bachir Bentria. The effect of vanadium impurity on Nickel Sigma 5(012) grain boundary. *Materials Science and Engineering A*, 577:197–201, 2013. ISSN 09215093. doi: 10.1016/j.msea.2013.04.047.

[142] Ying Zhang, Wen-Qiang Feng, Yue-Lin Liu, Guang-Hong Lu, and Tianmin Wang. First-principles study of helium effect in a ferromagnetic iron grain boundary: Energetics, site preference and segregation. *Nuclear Instruments and Methods in Physics Research Section B: Beam Interactions with Materials and Atoms*, 267(18):3200–3203, 2009. ISSN 0168-583X. doi: https://doi.org/10.1016/j.nimb.2009.06.064.

[143] M. Všianská and M. Šob. The effect of segregated sp-impurities on grain-boundary and surface structure, magnetism and embrittlement in nickel. *Progress in Materials Science*, 56(6):817–840, 2011. ISSN 00796425. doi: 10.1016/j.pmatsci.2011.01.008.

[144] Lü Chen, Ping Peng, Hou-Long Zhuang, and Dian-Wu Zhou. First-principle investigation of bismuth segregation at Σ5 (012) grain-boundaries in nickel. *Transactions of Nonferrous Metals Society of China*, 16(10):s813 – s819, 2006. ISSN 1003-6326. doi: https://doi.org/10.1016/S1003-6326(06)60306-3.

[145] Xuebang Wu, Xiang Shan Kong, Yu Wei You, Wei Liu, C. S. Liu, Jun Ling Chen, and G. N. Luo. Effect of transition metal impurities on the strength of grain boundaries in vanadium. *Journal of Applied Physics*, 120(9):95901, 2016. ISSN 10897550. doi: 10.1063/1.4961867.

[146] Wahyu Setyawan and Richard J Kurtz. Ab initio study of H, He, Li and Be impurity effect in tungsten Σ3 {112} and Σ27 {552} grain boundaries. *Journal of Physics: Condensed Matter*, 26(13):135004, mar 2014. ISSN 1361648X. doi: 10.1088/0953-8984/26/13/135004.

[147] Daniel Scheiber, Vsevolod I Razumovskiy, Peter Puschnig, Reinhard Pippan, and Lorenz Romaner. Ab initio description of segregation and cohesion of grain boundaries in W—25 at.% Re alloys. *Acta Materialia*, 88:180–189, 2015. ISSN 1359-6454. doi: https://doi.org/10.1016/j.actamat.2014.12.053.

[148] Xuebang Wu, Yu-Wei Wei You, Xiang-Shan Shan Kong, Jun-Ling Ling Chen, G.-N. N. Luo, Guang-Hong Hong Lu, C. S. Liu, and Zhiguang Wang. First-principles determination of grain boundary strengthening in tungsten: Dependence on grain boundary structure and metallic radius of solute. *Acta Materialia*, 120:315–326, 2016. ISSN 1359-6454. doi: https://doi.org/10.1016/j.actamat.2016.08.048.

[149] M. Christensen, T. M. Angeliu, J. D. Ballard, J. Vollmer, R. Najafabadi, and E. Wimmer. Effect of impurity and alloying elements on Zr grain boundary strength from first-principles computations. *Journal of Nuclear Materials*, 404(2):121–127, 2010. ISSN 0022-3115. doi: https://doi.org/10.1016/j.jnucmat.2010.07.012.

[150] Steve Plimpton. Fast Parallel Algorithms for Short-Range Molecular Dynamics. *Journal of Computational Physics*, 117(1):1–19, mar 1995. ISSN 0021-9991. doi: https://doi.org/10.1006/jcph.1995.1039.

[151] W T Geng, A J Freeman, R Wu, and G B Olson. Effect of Mo and Pd on the grain-boundary cohesion of Fe. *Phys. Rev. B*, 62(10):6208–6214, sep 2000. doi: 10.1103/PhysRevB.62.6208.

[152] Yan Quan Fen and Chong Yu Wang. Electronic effects of nitrogen and phosphorus on iron grain boundary cohesion. *Computational Materials Science*, 20(1):48–56, 2001. ISSN 09270256. doi: 10.1016/S0927-0256(00)00124-5.

[153] J Spencer Braithwaite and Peter Rez. Grain boundary impurities in iron. *Acta Materialia*, 53(9):2715–2726, 2005. ISSN 1359-6454. doi: https://doi.org/10.1016/j.actamat.2005.02.033.

[154] Hao Jin, Ilya Elfimov, and Matthias Militzer. Study of the interaction of solutes with Σ5 (013) tilt grain boundaries in iron using density-functional theory. *Journal of Applied Physics*, 115(9):093506, mar 2014. ISSN 0021-8979. doi: 10.1063/1.4867400.

[155] Eunan J McEniry, Tilmann Hickel, and Jörg Neugebauer. Hydrogen behaviour at twist $\{110\}$ grain boundaries in α-Fe. *Philosophical Transactions of the Royal Society of London A: Mathematical, Physical and Engineering Sciences*, 375(2098), 2017. ISSN 1364-503X. doi: 10.1098/rsta.2016.0402.

[156] A Y Lozovoi and A T Paxton. Boron in copper: A perfect misfit in the bulk and cohesion enhancer at a grain boundary. *Phys. Rev. B*, 77(16):165413, apr 2008. doi: 10.1103/PhysRevB.77.165413.

[157] Fanshun Meng, Xiaoming Lu, Yongli Liu, and Yang Qi. First-principles study on the effect and magnetism of iron segregation in Cu grain boundary. *Journal of Materials Science*, 52(8):4309–4322, 2017. ISSN 1573-4803. doi: 10.1007/s10853-016-0526-z.

[158] V. I. Razumovskiy, S. V. Divinski, and L. Romaner. Solute segregation in Cu: DFT vs. Experiment. *Acta Materialia*, 147:122–132, 2018. ISSN 1359-6454. doi: https://doi.org/10.1016/j.actamat.2018.01.011.

[159] D. Scheiber, R. Pippan, P. Puschnig, and L. Romaner. Ab initiosearch for cohesion-enhancing impurity elements at grain boundaries in molybdenum and tungsten. *Modelling and Simulation in Materials Science and Engineering*, 24(8):85009, nov 2016. ISSN 1361651X. doi: 10.1088/0965-0393/24/8/085009.

[160] Yong-Jie Hu, Ge Zhao, Baiyu Zhang, Chaoming Yang, Mingfei Zhang, Zi-Kui Liu, Xiaofeng Qian, and Liang Qi. Local electronic descriptors for solute-defect interactions in bcc refractory metals. *Nature Communications*, 10(1):4484, 2019. ISSN 2041-1723. doi: 10.1038/s41467-019-12452-7.

[161] R. Hill. The Elastic Behaviour of a Crystalline Aggregate. *Proceedings of the Physical Society. Section A*, 65(5):349–354, may 1952. ISSN 0370-1298. doi: 10.1088/0370-1298/65/5/307.

[162] Maarten de Jong, Wei Chen, Thomas Angsten, Anubhav Jain, Randy Notestine, Anthony Gamst, Marcel Sluiter, Chaitanya Krishna Ande, Sybrand van der Zwaag, Jose J Plata, Cormac Toher, Stefano Curtarolo, Gerbrand Ceder, Kristin A. Persson, and Mark Asta. Charting the complete elastic properties of inorganic crystalline compounds. *Scientific Data*, 2:150009, mar 2015. ISSN 2052-4463. doi: 10.1038/sdata.2015.9.

[163] W T Read, W Shockley, and Volumf Number. Dislocation Models of Crystal Grain Boundaries. *Phys. Rev.*, 78(3):275–289, may 1950. doi: 10.1103/PhysRev.78.275.

[164] B. Cantor, I.T.H. Chang, P. Knight, and A.J.B. Vincent. Microstructural development in equiatomic multicomponent alloys. *Materials Science and Engineering: A*, 375-377: 213–218, July 2004. ISSN 09215093. doi: 10.1016/j.msea.2003.10.257.

[165] Michael C. Gao. *High-Entropy Alloys*. Springer Science+Business Media, New York, NY, 2016. ISBN 978-3-319-27011-1.

[166] B. Gludovatz, A. Hohenwarter, D. Catoor, E. H. Chang, E. P. George, and R. O. Ritchie. A fracture-resistant high-entropy alloy for cryogenic applications. *Science*, 345(6201): 1153–1158, September 2014. ISSN 0036-8075, 1095-9203. doi: 10.1126/science.1254581.

[167] ZiJiao Zhang, M. M. Mao, Jiangwei Wang, Bernd Gludovatz, Ze Zhang, Scott X. Mao, Easo P. George, Qian Yu, and Robert O. Ritchie. Nanoscale origins of the damage tolerance of the high-entropy alloy CrMnFeCoNi. *Nature Communications*, 6(1):10143, December 2015. ISSN 2041-1723. doi: 10.1038/ncomms10143.

[168] Yu Zou, Soumyadipta Maiti, Walter Steurer, and Ralph Spolenak. Size-dependent plasticity in an Nb25Mo25Ta25W25 refractory high-entropy alloy. *Acta Materialia*, 65:85–97, February 2014. ISSN 13596454. doi: 10.1016/j.actamat.2013.11.049.

[169] Oleg N. Senkov, Daniel B. Miracle, Kevin J. Chaput, and Jean-Philippe Couzinie. Development and exploration of refractory high entropy alloys—A review. *Journal of Materials Research*, 33(19):3092–3128, October 2018. ISSN 0884-2914, 2044-5326. doi: 10.1557/jmr.2018.153.

[170] Michael Widom, W. P. Huhn, S. Maiti, and W. Steurer. Hybrid Monte Carlo/Molecular Dynamics Simulation of a Refractory Metal High Entropy Alloy. *Metallurgical and Materials Transactions A*, 45(1):196–200, January 2014. ISSN 1073-5623, 1543-1940. doi: 10.1007/s11661-013-2000-8.

[171] F. X. Zhang, Shijun Zhao, Ke Jin, H. Xue, G. Velisa, H. Bei, R. Huang, J. Y. P. Ko, D. C. Pagan, J. C. Neuefeind, W. J. Weber, and Yanwen Zhang. Local Structure and Short-Range Order in a NiCoCr Solid Solution Alloy. *Physical Review Letters*, 118(20):205501, May 2017. ISSN 0031-9007, 1079-7114. doi: 10.1103/PhysRevLett.118.205501.

[172] C. Niu, A. J. Zaddach, A. A. Oni, X. Sang, J. W. Hurt, J. M. LeBeau, C. C. Koch, and D. L. Irving. Spin-driven ordering of Cr in the equiatomic high entropy alloy NiFeCrCo. *Applied Physics Letters*, 106(16):161906, April 2015. ISSN 0003-6951, 1077-3118. doi: 10.1063/1.4918996.

[173] Qing-Jie Li, Howard Sheng, and Evan Ma. Strengthening in multi-principal element alloys with local-chemical-order roughened dislocation pathways. *Nature Communications*, 10 (1):3563, December 2019. ISSN 2041-1723. doi: 10.1038/s41467-019-11464-7.

[174] Jun Ding, Mark Asta, and Robert O. Ritchie. Melts of CrCoNi-based high-entropy alloys: Atomic diffusion and electronic/atomic structure from *ab initio* simulation. *Applied Physics Letters*, 113(11):111902, September 2018. ISSN 0003-6951, 1077-3118. doi: 10.1063/1.5045216.

[175] Jun Ding, Qin Yu, Mark Asta, and Robert O. Ritchie. Tunable stacking fault energies by tailoring local chemical order in CrCoNi medium-entropy alloys. *Proceedings of the National Academy of Sciences*, 115(36):8919–8924, September 2018. ISSN 0027-8424, 1091-6490. doi: 10.1073/pnas.1808660115.

[176] Xiang-Guo Li, Chi Chen, Hui Zheng, Yunxing Zuo, and Shyue Ping Ong. Complex strengthening mechanisms in the NbMoTaW multi-principal element alloy. *npj Computational Materials*, 6(1):70, December 2020. ISSN 2057-3960. doi: 10.1038/s41524-020-0339-0.

[177] Ruopeng Zhang, Shiteng Zhao, Jun Ding, Yan Chong, Tao Jia, Colin Ophus, Mark Asta, Robert O. Ritchie, and Andrew M. Minor. Short-range order and its impact on the CrCoNi medium-entropy alloy. *Nature*, 581(7808):283–287, May 2020. ISSN 0028-0836, 1476-4687. doi: 10.1038/s41586-020-2275-z.

[178] F. Otto, A. Dlouhý, K.G. Pradeep, M. Kuběnová, D. Raabe, G. Eggeler, and E.P. George. Decomposition of the single-phase high-entropy alloy CrMnFeCoNi after prolonged anneals at intermediate temperatures. *Acta Materialia*, 112:40–52, June 2016. ISSN 13596454. doi: 10.1016/j.actamat.2016.04.005.

[179] William Paul Huhn and Michael Widom. Prediction of A2 to B2 Phase Transition in the High-Entropy Alloy Mo-Nb-Ta-W. *JOM*, 65(12):1772–1779, December 2013. ISSN 1047-4838, 1543-1851. doi: 10.1007/s11837-013-0772-3.

[180] Fritz Körmann, Andrei V. Ruban, and Marcel H.F. Sluiter. Long-ranged interactions in bcc NbMoTaW high-entropy alloys. *Materials Research Letters*, 5(1):35–40, January 2017. ISSN 2166-3831. doi: 10.1080/21663831.2016.1198837.

[181] Qingqing Ding, Yin Zhang, Xiao Chen, Xiaoqian Fu, Dengke Chen, Sijing Chen, Lin Gu, Fei Wei, Hongbin Bei, Yanfei Gao, Minru Wen, Jixue Li, Ze Zhang, Ting Zhu, Robert O. Ritchie, and Qian Yu. Tuning element distribution, structure and properties by composition in high-entropy alloys. *Nature*, 574(7777):223–227, October 2019. ISSN 0028-0836, 1476-4687. doi: 10.1038/s41586-019-1617-1.

[182] Changning Niu, Carlyn R. LaRosa, Jiashi Miao, Michael J. Mills, and Maryam Ghazisaeidi. Magnetically-driven phase transformation strengthening in high entropy alloys. *Nature Communications*, 9(1):1363, December 2018. ISSN 2041-1723. doi: 10.1038/s41467-018-03846-0.

[183] Binglun Yin, Shuhei Yoshida, Nobuhiro Tsuji, and W. A. Curtin. Yield strength and misfit volumes of NiCoCr and implications for short-range-order. *Nature Communications*, 11 (1):2507, December 2020. ISSN 2041-1723. doi: 10.1038/s41467-020-16083-1.

[184] Sheng Yin, Jun Ding, Mark Asta, and Robert O. Ritchie. Ab initio modeling of the role of local chemical short-range order on the Peierls potential of screw dislocations in body-centered cubic high-entropy alloys. *arXiv:1912.10506 [cond-mat]*, December 2019.

[185] Yunxing Zuo, Chi Chen, Xiangguo Li, Zhi Deng, Yiming Chen, Jörg Behler, Gábor Csányi, Alexander V. Shapeev, Aidan P. Thompson, Mitchell A. Wood, and Shyue Ping Ong. Performance and Cost Assessment of Machine Learning Interatomic Potentials. *The Journal of Physical Chemistry A*, 124(4):731–745, January 2020. ISSN 1089-5639, 1520-5215. doi: 10.1021/acs.jpca.9b08723.

[186] Steve Plimpton. Fast Parallel Algorithms for Short-Range Molecular Dynamics. *Journal of Computational Physics*, 117(1):1–19, March 1995. ISSN 00219991. doi: 10.1006/jcph.1995.1039.

[187] A. Van der Ven, G. Ceder, M. Asta, and P. D. Tepesch. First-principles theory of ionic diffusion with nondilute carriers. *Physical Review B*, 64(18):184307, October 2001. ISSN 0163-1829, 1095-3795. doi: 10.1103/PhysRevB.64.184307.

[188] Pui-Wai Ma and S. L. Dudarev. Effect of stress on vacancy formation and migration in body-centered-cubic metals. *Physical Review Materials*, 3(6):063601, June 2019. ISSN 2475-9953. doi: 10.1103/PhysRevMaterials.3.063601.

[189] K.-Y. Tsai, M.-H. Tsai, and J.-W. Yeh. Sluggish diffusion in Co–Cr–Fe–Mn–Ni high-entropy alloys. *Acta Materialia*, 61(13):4887–4897, August 2013. ISSN 13596454. doi: 10.1016/j.actamat.2013.04.058.

[190] Spencer L. Thomas and Srikanth Patala. Vacancy diffusion in multi-principal element alloys: The role of chemical disorder in the ordered lattice. *Acta Materialia*, 196:144–153, September 2020. ISSN 13596454. doi: 10.1016/j.actamat.2020.06.022.

[191] Anirudh Raju Natarajan and Anton Van der Ven. Linking electronic structure calculations to generalized stacking fault energies in multicomponent alloys. *npj Computational Materials*, 6(1):80, December 2020. ISSN 2057-3960. doi: 10.1038/s41524-020-0348-z.

[192] J. W. Christian. Some surprising features of the plastic deformation of body-centered cubic metals and alloys. *Metallurgical Transactions A*, 14(7):1237–1256, July 1983. ISSN 0360-2133, 1543-1940. doi: 10.1007/BF02664806.

[193] L. Lilensten, J.-P. Couzinié, L. Perrière, A. Hocini, C. Keller, G. Dirras, and I. Guillot. Study of a bcc multi-principal element alloy: Tensile and simple shear properties and underlying deformation mechanisms. *Acta Materialia*, 142:131–141, January 2018. ISSN 13596454. doi: 10.1016/j.actamat.2017.09.062.

[194] G. Dirras, J. Gubicza, A. Heczel, L. Lilensten, J.-P. Couzinié, L. Perrière, I. Guillot, and A. Hocini. Microstructural investigation of plastically deformed Ti20Zr20Hf20Nb20Ta20 high entropy alloy by X-ray diffraction and transmission electron microscopy. *Materials Characterization*, 108:1–7, October 2015. ISSN 10445803. doi: 10.1016/j.matchar.2015.08.007.

[195] Alexander Stukowski. Structure identification methods for atomistic simulations of crystalline materials. *Modelling and Simulation in Materials Science and Engineering*, 20(4): 045021, June 2012. ISSN 0965-0393, 1361-651X. doi: 10.1088/0965-0393/20/4/045021.

[196] Alexander Stukowski, Vasily V Bulatov, and Athanasios Arsenlis. Automated identification and indexing of dislocations in crystal interfaces. *Modelling and Simulation in Materials Science and Engineering*, 20(8):085007, December 2012. ISSN 0965-0393, 1361-651X. doi: 10.1088/0965-0393/20/8/085007.

[197] S. Mahajan and D. F. Williams. Deformation Twinning in Metals and Alloys. *International Metallurgical Reviews*, 18(2):43–61, June 1973. ISSN 0367-9020. doi: 10.1179/imtlr.1973.18.2.43.

[198] Alexander Stukowski. Visualization and analysis of atomistic simulation data with OVITO–the Open Visualization Tool. *Modelling and Simulation in Materials Science and Engineering*, 18(1):015012, January 2010. ISSN 0965-0393, 1361-651X. doi: 10.1088/0965-0393/18/1/015012.

[199] Yu Zou, Jeffrey M. Wheeler, Huan Ma, Philipp Okle, and Ralph Spolenak. Nanocrystalline High-Entropy Alloys: A New Paradigm in High-Temperature Strength and Stability. *Nano Letters*, 17(3):1569–1574, March 2017. ISSN 1530-6984, 1530-6992. doi: 10.1021/acs.nanolett.6b04716.

[200] S.W. Xin, M. Zhang, T.T. Yang, Y.Y. Zhao, B.R. Sun, and T.D. Shen. Ultrahard bulk nanocrystalline VNbMoTaW high-entropy alloy. *Journal of Alloys and Compounds*, 769: 597–604, November 2018. ISSN 09258388. doi: 10.1016/j.jallcom.2018.07.331.

[201] X. Y. Li, Z. H. Jin, X. Zhou, and K. Lu. Constrained minimal-interface structures in polycrystalline copper with extremely fine grains. *Science*, 370(6518):831–836, November 2020. ISSN 0036-8075, 1095-9203. doi: 10.1126/science.abe1267.

[202] Michael Chandross and Nicolas Argibay. Ultimate Strength of Metals. *Physical Review Letters*, 124(12):125501, March 2020. ISSN 0031-9007, 1079-7114. doi: 10.1103/PhysRevLett.124.125501.

[203] Suveen N. Mathaudhu. Building on Gleiter: The Foundations and Future of Deformation Processing of Nanocrystalline Metals. *Metallurgical and Materials Transactions A*, 51 (12):6020–6044, December 2020. ISSN 1543-1940. doi: 10.1007/s11661-020-06031-5.